PHYSICAL ASPECTS OF SCRAPED-SURFACE HEAT EXCHANGERS

PHYSICAL ASPECTS OF SCRAPED-SURFACE HEAT EXCHANGERS

PROEFSCHRIFT

TER VERKRIJGING VAN DE GRAAD VAN DOCTOR IN DE
TECHNISCHE WETENSCHAPPEN AAN DE TECHNISCHE HOGESCHOOL DELFT,
OP GEZAG VAN DE RECTOR MAGNIFICUS DR IR C.J.D.M. VERHAGEN,
HOOGLERAAR IN DE AFDELING DER TECHNISCHE NATUURKUNDE,
VOOR EEN COMMISSIE UIT DE SENAAT TE VERDEDIGEN OP
WOENSDAG 4 FEBRUARI 1970 TE 14.00 UUR

DOOR

AUGUST MARIA TROMMELEN
NATUURKUNDIG INGENIEUR
GEBOREN TE LOON OP ZAND

DIT PROEFSCHRIFT IS GOEDGEKEURD DOOR
DE PROMOTOREN PROF. DR IR W.J. BEEK
EN PROF. DR IR N.W.F. KOSSEN.

ACKNOWLEDGEMENT

The author wishes to express his gratitude to the Management of the Unilever Research Laboratory Vlaardingen and of Unilever N. V. for their permission to publish the results of the investigation in this form. The valuable assistance of colleagues is gratefully acknowledged.

CONTENTS

CHAPTER 1

INTRODUCTION

Heat transfer to viscous or temperature-sensitive liquids often gives rise to difficulties. The heat transfer coefficients in conventional heat exchangers without moving parts, such as shell and tube-heat exchangers and plate-heat exchangers, are very low for viscous liquids. Since turbulence is absent, only by conduction will heat be transported to the faster flowing fluid at some distance from the wall. If heat-sensitive liquids are heated in a heat exchanger, for instance, for sterilization, they will deteriorate on the heated surface.

Another problem arises if the liquid that is being cooled crystallizes on the cooled surface. The solid layer of crystallized material then forms an additional resistance to heat transfer. Furthermore, part of the area available for flow is blocked and the liquid is forced to flow through a narrow channel, which results in a lower average residence time.

These problems can be overcome by continuously scraping the surface of the heat exchanger. This results in high temperature gradients at the wall and, consequently a high heat transfer coefficient. The scraping also reduces the time that any part of the liquid is exposed to high or low temperatures, thus avoiding the formation of a solid layer of crystallized or burnt material.

A fairly extensive list of applications of scraped-surface heat exchangers is given by Bolanowski and Lineberry[1]. These exchangers are used for the cooling and crystallization of margarine, ice-cream, shortening and orange juice concentrate. They are also used for sterilizing baby food puree, pasteurizing eggs and custard, the aeration of egg whites and the caramelization of sweetened condensed milk. Finally sulphonation for the detergents industry is mentioned.

There are two different types of scraped-surface heat exchangers:

- The heat exchanger is completely filled with the liquid that is being cooled or heated. This type is also called 'Votator'[+].

- The liquid flows as a film over the heat exchanger wall. This type is used for such processes as evaporation, stripping and deodorization.

The work described in this thesis is restricted to the first type, the completely filled scraped-surface heat exchanger (hereafter referred to as a SSHE). A sketch of a SSHE is given in Fig. 1. The liquid to be processed enters the SSHE at 1 and flows through the annulus formed by the shaft 5 and the scraped surface. The liquid leaves the SSHE at 2. The heat transfer medium flows through a helix, or through a jacket around the heat transfer tube as in Fig. 1. The rotating shaft is equipped with scraper blades, which are pressed against the heat transfer surface by centrifugal and viscous forces. Usually the blades are attached to the shaft in a manner allowing free movement. It is possible to use water, steam, ammonia, brine or dowtherm as the heat transfer medium. The choice of the construction material of heat transfer tube, shaft and blades depends on the physical and chemical properties of product and/or coolant. Usually the heat transfer tube is made of mild steel, which is chromium plated on the product side. A stainless steel tube would reduce the overall heat transfer coefficient considerably.

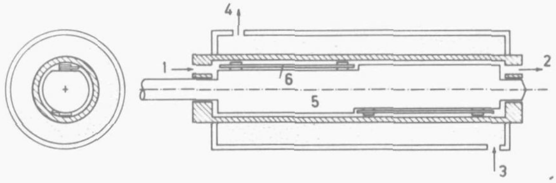

Fig. 1 *Cross-section and longitudinal section of a SSHE*

1. Product inlet
2. Product outlet
3. Coolant inlet
4. Coolant outlet
5. Shaft
6. Scraper blade.

The first patent for a SSHE was granted in 1928; its development was mainly undertaken by the Girdler Company[2]. Since that time the basic principle of the SSHE has not changed, although many patents have been granted for slightly modified types. Some of the changes involve the way in which the blades are attached to the shaft. A British patent[3] describes a polypropylene blade in a stainless steel holder. The holder has two pins that slide in holes in the rotating shaft. The blades are pressed against the wall by centrifugal force or by compression springs mounted in the holes in the

---

[+] Trade name of the Chemetron Corporation, Louisville, Kentucky, USA.

shaft. In a Japanese patent[4] a construction is described in which the blade scrapes the wall for only half of each revolution. Better mixing is claimed for this construction. Other constructions are known in which the rotating shaft is excentrically mounted in the heat transfer tube, either on one or both sides.

The main parameters in the design of a SSHE are the length L and the diameter, d_t, of the heat transfer tube, the diameter, d_s, of the rotating shaft, the number of rows of scraper blades, n, and the shaft speed, N. Typical values of these parameters are:

L : 1-1.5 m
d_t : 0.1-0.3 m
$d_t - d_s$: 0.005-0.05 m
N : 3-30 rev.s^{-1}
n : 2-10

The length and the diameter are usually limited by the mechanical properties of the SSHE. The annular space is determined by the permitted pressure drop and residence time. The shaft speed should be high to obtain a high heat transfer coefficient, but is limited by power consumption and wear of the scraper blades, which both depend strongly on the rheological properties of the liquid that is being processed.

Although many papers on SSHEs have been published, there is still a lack of information for the design engineer. There are no reliable correlations for heat transfer and power consumption. Scaling-up can be a problem. The mechanism of heat transfer is not fully understood and the mixing performance of a SSHE is not known. In order to elucidate these problems, the investigation reported in this thesis has been carried out.

Our experiments were restricted to the cooling of Newtonian liquids that did not crystallize under the experimental conditions. We imposed this restriction because interpretation of the experimental results of cooling liquids with complex rheological properties, or of crystallizing liquids, would have been extremely difficult.

The study was split into three parts, viz. flow pattern, power consumption and heat transfer. The three phenomena are interrelated: the flow pattern determines the shear stresses in the SSHE and therefore the power consumption. The flow pattern also influences heat transfer, for the following two reasons. Firstly, the distribution of the scraped-off cold layer over the bulk of the liquid is determined by the flow pattern. Secondly, axial dispersion in the SSHE reduces the effective temperature difference between the process fluid and the coolant. The relation between power consumption and heat transfer is obvious: the heat that is dissipated in the liquid must be removed again, thus reducing the net decrease in heat content of the process liquid.

CHAPTER 2

LITERATURE SURVEY

In the survey of the literature on SSHEs given in this chapter, only articles on full-tube SSHEs dealing with physico-technical aspects are included. Papers on wiped-film heat exchangers and those dealing only with special applications have been omitted.

The first section of this chapter gives brief descriptions of the papers in chronological order. In the second section the most important articles have been interpreted to derive a correlation for the heat transfer coefficient, that is based on penetration theory, combined with an empirical correction term.

2.1 Description of papers

In 1931 a paper was published by Huggins[5], dealing with the effect of scrapers on heating, cooling and mixing in stirred vessels. Heating and cooling tests were carried out with water, medium-viscous liquids and pasty materials. Heating and cooling times are in some cases halved by applying scrapers instead of paddle agitators. Experiments on power consumption show that the power consumption of an agitator with scrapers is 10 to 20 percent higher than that of the same agitator without scrapers, but because of the shorter heating or cooling time, there is a net saving in total power consumption.

A paper by Laughlin[6] describes a stirred vessel with scrapers used for drying pastes. No quantitative results are given.

Houlton[7] describes experiments on water-to-water heat transfer in a votator. The overall heat transfer coefficient varies between 3000 and 7000 $W.m^{-2}.^{o}C^{-1}$. The heat transfer medium flows through an almost rectangular helical channel around the heat transfer tube. It is shown that the Dittus-Boelter equation[8] may be used to calculate heat transfer coefficients on the jacket side. The influence on heat transfer of variations of shaft speed and liquid flow rate is investigated. No correlation for the heat transfer coefficient on the scraped side is given. Bolanowski and Lineberry[1] describe applications of SSHEs and give values of the overall heat transfer coefficients that are obtained in commercially available heat exchangers. Some of their data are given in Table 1.

Table 1

Applications of SSHEs (taken from Ref. 1)

Operation	Material	Overall heat transfer coefficient U ($W.m^{-2}\ ^oC^{-1}$)
Cooling and plasticizing	Lard and shortening	1400
Cooling	Margarine	1750
Heating	Starch	1750
Cooling	Starch	2100
Sterilization	Fruit puree	2300

Skelland[9] is the first author to attempt to find a correlation for the heat transfer coefficient, based on dimensional analysis and experiments. The author argues that the heat transfer takes place by conduction through a film and that the thermal conductivity, λ, of the liquid is important. The thickness of the film is determined by the linear axial velocity, v, the shaft speed, N, the shaft diameter, d_s, the tube diameter, d_t, the fluid density, ρ, and the viscosity, η. Other parameters to be taken into consideration are the length of the tube, L, and the specific heat of the fluid, c_p. Dimensional analysis showed that the following groups should be included in a correlation for heat transfer:

$$\frac{\alpha_s d_t}{\lambda}, \frac{d_t v \rho}{\eta}, \frac{c_p \eta}{\lambda}, \frac{d_t N}{v}, \frac{L}{d_t} \text{ and } \frac{d_s}{d_t}$$

The number of rows of scraper blades was not included, as all experiments were carried out with SSHEs having two rows. The ratio of shaft diameter and tube diameter was also not considered, because it remained almost constant during Skelland's experiments.

Skelland used two ammonia-cooled SSHEs, similar in construction but different in size. The equipment details are given in Table 2.

Table 2.

Equipment details of Skelland's votators[9]

	Small unit	Large unit	
Number of tubes in series	1	2	3
Effective scraped area (m^2)	0.0638	0.744	1.114
Internal diameter of heat transfer tube (m)	0.0762	0.102	0.102
Shaft diameter (m)	0.0572	0.0825	0.0825
Shaft speed (rev. s^{-1})	1.5-7.5	12.5	12.5

The materials used were water, glycerol-water mixtures and two similar glyceride oils.

Over-all heat transfer coefficients were calculated on the basis of the inside scraped-surface area, it being assumed that half the area of the flanged heads of the refrigerant jacket was effective in the cooling. For the driving force, the logarithmic mean temperature difference was used. In experiments with crystallizing oils the frictional heat was taken into account.

Ammonia-to-wall heat transfer coefficients were calculated from a correlation by McNelly[10] for the nucleate boiling regime. The scraped-side heat transfer coefficient was calculated from:

$$\frac{1}{U} = \frac{1}{\alpha_c} + \frac{1}{\alpha_m} + \frac{1}{\alpha_s} \qquad (1)$$

in which α_c is the ammonia-side heat transfer coefficient and $1/\alpha_m$ is the resistance of the wall of the heat transfer tube.

The experimental results, as also those obtained by Houlton[7] can be correlated by means of the dimensionless equation:

$$\frac{\alpha_s d_t}{\lambda} = 4.9 \left(\frac{d_t v \rho}{\eta}\right)^{0.57} \left(\frac{c_p \eta}{\lambda}\right)^{0.47} \left(\frac{d_t N}{v}\right)^{0.17} \left(\frac{d_t}{L}\right)^{0.37} \qquad (2)$$

From Eq. (2) Skelland[11] derives scale-up relationships for heat transfer in votators. He considers the following aspects:

- Rate of heat transfer per unit area of the scraped surface;
- Total heat transfer per unit mass of the product;
- Rate of heat transfer per unit mass of the product.

He also considers combinations of the above aspects, and derives relationships by which it is possible to duplicate heat transfer performance in two SSHEs of differing dimensions, but of a certain conventional design.

Latinen[12] discusses Skelland's paper[9]. He applies penetration theory to derive a theoretical equation for the heat transfer coefficient.
His reasoning is as follows:

'Ideally material at a uniform bulk temperature continually moves down the rear surface of the scraper blades to the cylindrical heat transfer surface where it either heats or cools by molecular conduction until the following blade scrapes it up and thoroughly mixes it with the bulk fluid. Since the depth of conductive heat penetration per pass is small in the range of r.p.m.'s where votators usually operate, the small variation in peripheral fluid velocities within the thin heat transfer layer may be neglected. Under these ideal conditions, the heat transfer mechanism is identical to molecular conduction into a semi-infinite solid where the contact time is the time between successive blade passes. Using the known surface temperature gradient[13], the average rate of heat influx for a given contact time may be readily calculated and expressed in terms of an effective scraped-film coefficient α_s:

$$\alpha_s = \frac{2}{\sqrt{\pi}} \left(\lambda \rho c_p N n \right)^{0.5} , \qquad (3)$$

Latinen goes on to say that for low Reynolds numbers the bulk mixing intensity is low and that this causes the heat transfer coefficients to be less than calculated from Eq. (3). On the other hand, at high Reynolds numbers the turbulent eddies might penetrate the theoretical heat transfer layer, causing higher film coefficients. Latinen compares the results of Houlton[7] and Skelland[9] with those of Eq. (3). The water data by Houlton are about 15 percent higher than predicted by Eq. (3). Skelland's measurements show no agreement with Eq. (3). Latinen concludes that the heat transfer mechanism is more complex than the penetration model suggests.

A somewhat more sophisticated approach to the penetration theory is made by Kool[14]. This author does not assume that the temperature of the heat transfer surface is constant. Because of the non-stationary heat flux through the wall and the resistance to heat transfer from the scraped surface to the coolant, the temperature of the scraped surface changes. If this phenomenon is included in the equations for non-stationary heat conduction, a complicated correlation for the heat transfer coefficient results. This correlation can be simplified to:

$$\alpha_s = 1.24\, \alpha_o^{-0.03} \quad (\lambda \rho c_p N n)^{0.515} \tag{4}$$

in which α_o is the heat transfer coefficient from scraping plane to coolant. Eq. (4) holds with 1 percent accuracy if the following condition is met:

$$0.2 < \frac{\alpha_o}{(\lambda \rho c_p N n)^{0.5}} < 30 \tag{5}$$

This condition is usually met in practice.

The difference between Eqs. (3) and (4) can be illustrated by an example, which shows that this sophistication is usually not necessary.

Let: $\alpha_o = 1750\ \mathrm{W.m^{-2}.\ ^oC^{-1}}$

$\lambda = 0.23\ \mathrm{W.m^{-1}.\ ^oC^{-1}}$

$\rho = 800\ \mathrm{kg.m^{-3}}$

$c_p = 2100\ \mathrm{J.kg^{-1}.\ ^oC^{-1}}$

$N = 8.3\ \mathrm{rev.\ s^{-1}}$

$n = 2$

From Eq. (3) it follows that:

$\alpha_s = 2880\ \mathrm{W.m^{-2}.\ ^oC^{-1}}$

Solution of Eq. (4) gives:

$\alpha_s = 3280\ \mathrm{W.m^{-2}.\ ^oC^{-1}}$

In this case there is a difference of 14%.

Harriot[15] reports heat transfer measurements with water, motor oil and carrot puree. The heat exchanger was a nickel pipe with an internal diameter of 0.0762 m and a length of 0.28 m. Two scraper blades were mounted on a shaft, the speed of which was varied between 6.7 and 30 rev. $\mathrm{s^{-1}}$. The products were cooled with water flowing through a helical channel around the heat transfer tube. Harriot used the same method as Houlton[7] to calculate the scraped-side heat transfer coefficient from the overall heat transfer coefficient. The conclusions he reaches are that the simple Eq. (3) predicts the heat transfer coefficients for water and fluids of low viscosity with reasonable accuracy. For viscous liquids the heat transfer coefficient is less than predicted by Eq. (3), because of incomplete mixing of the fluid scraped from the wall with the fluid in the annular space. The validity of the penetration theory for the measurements with water shows that for these experiments the penetration depth is smaller than the thickness of the hydrodynamic laminar sublayer.

Blaisdell and Zahradnik[16] report the effects of flow rate, shaft speed and temperature rise on the temperature distribution of water in a steam-heated laboratory-scale SSHE. The length of the SSHE was 0.305 m, the tube diameter 0.076 m and the shaft diameter 0.056 m. Two cutaway fiber blades were mounted on the shaft. The bulk fluid temperature was measured by thermocouples at the inlet, outlet and at five points along the shaft. The results of the experiments are not accurate enough to give a complete picture of the axial temperature profile in a SSHE. There appears to be a steep temperature change in the first part of the heat exchanger, which might indicate backmixing. In the other part of the SSHE, the logarithm of the temperature difference between the heat transfer medium and the process fluid was approximated by a linear function of the axial distance in the apparatus. It would appear that axial dispersion should not be neglected in a SSHE.

In 1960 a paper on the prediction of refrigerant-side heat transfer was published by Skelland[17] in which correlations for boiling liquids in the nucleate boiling regime are compared. When these correlations are used for calculating the heat transfer coefficient for boiling ammonia under certain conditions, it appears that the scattering of the plotted points is very great. No reliable correlation is available. This conclusion invalidates the results of the earlier work of Skelland[9,11], as the author states in a more recent article[18].

Hosking[19] gives a survey of the development of votators. Heat transfer coefficients for various liquids are listed in Table 3.

Table 3

Range of overall heat transfer coefficients U reported by Hosking[19].

	$(W.m^{-2}\ {}^{o}C^{-1})$
Thin liquid	2300-4000
Viscous liquid	850-2300
Crystallization	850-3700
Sulfonation	850-2300
Polymerization	1100-2800

An article on power consumption in SSHEs is published in 1962 by Skelland and Leung[20]. Measurements on power consumption were carried out during cooling glycerol/water mixtures in a water-cooled, scraped-surface heat exchanger, having a length of 0.47 m and an internal tube diameter of 0.076 m. The shaft diameters were 0.025 m, 0.036 m, 0.046 m and 0.057 m. The number of rows of scraper blades could be varied between two and five and the shaft speed between 1.7 and 12.5 rev. s^{-1}. Cooling water flowed through a helical channel of $7.3 \times 19.1 \times 10^{-6}$ m^2 around the heat transfer tube. The power consumed by the motor was measured with a three-phase balanced-load wattmeter. By correcting for the losses in the motor itself and those in the transmission and bearings the power consumed in rotating the shaft and blades inside the heat exchanger was determined.

The important dimensionless groups were determined by dimensional analysis. The relevant geometrical parameters were the tube diameter d_t and the tube length L; no dependence of power consumption on shaft diameter was measured. The power P is also dependent on shaft speed N, number of rows of scraper blades n, fluid density ρ and bulk viscosity η. An influence of the viscosity of the liquid adjacent to the tube wall could not be determined. From dimensional analysis, it was found that the important dimensionless groups required to correlate the experimental data are the power number $\frac{P}{d_t^5 N^3 \rho}$ and the Reynolds number $\frac{d_t^2 N \rho}{\eta}$.

The experiments could be correlated by

$$\frac{P}{d_t^5 N^3 \rho} = 77{,}500 \left(\frac{d_t^2 N \rho}{\eta} \right)^{-1.27} n^{0.59} \tag{6}$$

A further result of the work was that at high viscosities and high shaft speeds, the power consumed in rotating the shaft and blades is so great that it becomes a substantial fraction of the total heat transferred.

During the same experiments, heat transfer measurements were also carried out; they were reported by Skelland, Oliver and Tooke[18]. The experimental procedure was similar to that of Houlton[7]. Glycerol, water and glycerol/water mixtures were used as the working fluids. The same dimensionless groups as used in Skelland's earlier work were considered. However, the group $d_t v\rho/\eta$ was replaced by $(d_t-d_s)v\rho/\eta$ in order to get a better correlation. Furthermore d_s/d_t and the number of rows of scraper blades n were included. Two correlations were found, one for thin liquids and one for viscous liquids ($\eta > 5 \times 10^{-3}$ N.s.m^{-2}), the latter being:

$$\frac{\alpha_s d_t}{\lambda} = 0.014 \left(\frac{c_p \eta}{\lambda}\right)^{0.96} \left(\frac{(d_t - d_s)\, v \rho}{\eta}\right)^{1.00} \left(\frac{d_t N}{v}\right)^{0.62} \left(\frac{d_s}{d_t}\right)^{0.55} n^{0.53} \qquad (7)$$

This equation will be discussed further in Chapter 2.2.

Dinglinger[21] froze water and aqueous solutions into thin solid layers in a SSHE. The heat transfer and the energy consumption were investigated under various operating conditions. The clearance between the edge of the scraper blade and the heat transfer surface could be varied. The shaft speeds were rather low (0.5-1.2 rev. s^{-1}). The heat transfer coefficients were higher than those calculated from Skelland's equation (7). The power consumption was correlated in the same way as by Skelland and Leung[20], Eq. (6), but now the power number appeared to be proportional to $Re_R^{-1.2}$.

In an article by Braginskii, Begachev and Pablushenko[22], a derivation, similar to that given earlier by Latinen[12], is given for the heat transfer coefficient, based on penetration theory. The authors introduce a coefficient that is smaller than unity to compensate for the fact that the liquid scraped off the wall is not completely mixed with the bulk of the liquid in the annular space. This coefficient is taken to be independent of the processing parameters and is dependent only on the dimensions of the scraper blades and of the SSHE used.

Measurements of heat transfer in a stirred vessel with scraper blades are reported by Van Dierendonck[23]. The heat transfer coefficients were lower than those predicted from Eq. (3). The author attributes this phenomenon to an unscraped layer of liquid on the wall of the vessel. The thickness of this layer is 0.5×10^{-3} m.

A slightly different type of heat exchanger used for milk products is described by Koelatsjinski[24]. Apart from scraper blades, there is also a helical ribbon attached to the shaft, similar to the screw flights in an extruder. The correlation found for the heat transfer coefficient is:

$$\frac{\alpha_s d_t}{\lambda} = 13.1 \left(\frac{\pi \rho N d_t^2}{\eta}\right)^{0.44} \left(\frac{\eta c_p}{\lambda}\right)^{0.33} \left(\frac{d_t - d_s}{d_t}\right)^{0.35} \qquad (8)$$

Vinogradov[25] suggests reducing the shaft speed and increasing the number of scraper blades in a SSHE in order to reduce the power consumption without changing the heat transfer coefficient. He assumes that the heat transfer coefficient is proportional to the number of rows of scraper blades and to the shaft speed. He also states that the power consumption is proportional to the number of rows of scraper blades and to the third power of the shaft speed.

Very extensive surveys on power requirements[26] and heat transfer[27] in close-clearance agitators are given by Penney and Bell. They prefer the term 'close-clearance' to 'scraped-surface' because they assume that almost invariably a film of liquid will exist between the agitator (anchor, scraper, extruder etc.) and the heat transfer wall. They distinguish between the fixed-clearance equipment that employs rigid agitators and that with variable clearance agitators which are forced toward the vessel wall by springs, centrifugal force and by hydrodynamic action of the fluid on the agitator. The 'slipper bearing effect' tends to force the agitator off the wall and, as the authors state, the clearance between agitator and wall varies with the operating conditions.

Commenting on the measurements on power consumption by Skelland and Leung[20] Penney and Bell state that, assuming the viscosity to be constant, the only possibility for the slope of ln Po vs. ln Re_R to be less than -1, is that the clearance increases as speed increases, in spite of the fact that the centrifugal force is proportional to N^2. A new power number is proposed which includes d_t^4 L rather than d_t^5, because it is reasonable to assume that the power consumption is proportional to the length of the heat exchanger. Further, this means that the correlation of data with this new power number will result in a scaling-up rule that the power consumption is proportional to d_t^2 L rather than d_t^3.

In their heat transfer survey[27] Penney and Bell discuss the effect of axial dispersion on the mean temperature difference for a heat exchanger. If there is no axial dispersion, the mean temperature difference is equal to the logarithmic mean temperature difference. This gives the maximum value of the driving force. Complete mixing gives the absolute minimum mean temperature difference. Every heat exchanger operates between these two extremes. The authors state that, in general, the effect of axial dispersion increases with increasing shaft speed and decreasing axial flow rate. Blaisdell and Zahradnik[16] have carried out experiments to determine the axial temperature distribution in a Votator. The data are not sufficiently accurate to allow quantitative conclusions to be drawn about the influence of axial dispersion on the temperature distribution. Penney and Bell also stress the importance of the variable clearance, since this causes a stagnant layer of liquid, the thickness of which is dependent on the operating conditions.

Bott, Azoory and Porter[28] present a theoretical axial diffusion model which predicts the effect of backmixing on heat transfer in a scraped-surface heat exchanger. A plug flow with axial dispersion model is assumed. Further assumptions are:

- The wall temperature is constant throughout the exchanger
- The local heat transfer coefficient is uniform
- The physical properties of the liquid are constant
- The axial dispersion coefficient, D_E, is constant
- The heat conduction in the direction of flow is negligible.

The effect of the dispersion on the heat transfer can be described in terms of two dimensionless quantities $N_T = \alpha_s A/\varnothing_m c_p$ and $Pe_D = vL/D_E$. The results of the calculations are given in Fig. 2. No measurements of D_E in votator-type heat exchangers are reported.

Ghosal, Srimani and Ghosh[29] report an experimental study of heat transfer in a steam-heated votator. Experiments were carried out with water, undiluted molasses, molasses/water solutions and glycerol/water solutions.

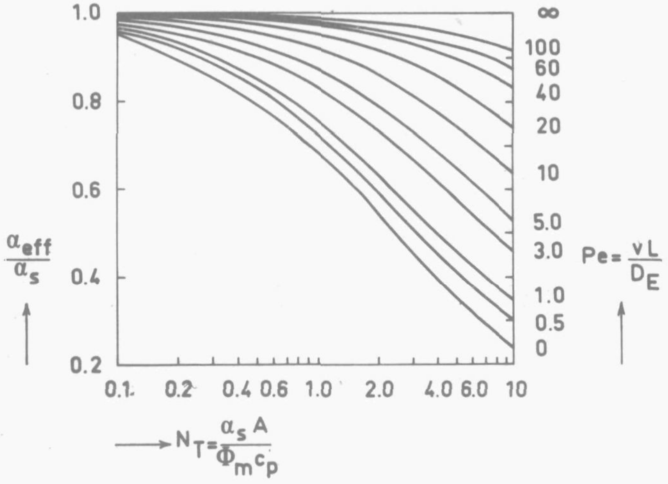

Fig. 2 Effect of Peclet number and N_T on the effective heat transfer coefficient.

A correlation was derived but the authors say that it correlates the measurements rather poorly. This is due partly to the way in which the exponents in the correlation have been evaluated and partly to the inaccuracy of the measurements (high resistance to heat transfer in the stainless steel heat transfer tube).

The most important experimental results are summarized in Table 4.

Table 4

Experimental results of various authors for heat transfer

Author(s)	Variables studied	Process liquid	Correlation for the heat transfer coefficient
Houlton[7]	N, v	Water	$\mathrm{Nu} = \mathrm{const.}\ \mathrm{Re_R}^{0.5}\ \mathrm{Pr}^{0.5} \left(\frac{d_t}{L}\right)^{0.4}$ (calculated by Latinen[12])
Harriot[15]	N, v liquid properties	Water oil	$\mathrm{Nu} = \mathrm{const.}\ \mathrm{Re_R}^{0.5}\ \mathrm{Pr}^{0.5}\ n^{0.5}$
Skelland[18] et al.	N, v, n, d_s liquid properties	Glycerol-water solutions	$\mathrm{Nu} = 0.014\ \mathrm{Re_R}^{0.62}\ \mathrm{Pr}^{0.96}\ n^{0.53}\ \mathrm{x}$ $\mathrm{x} \left\{\frac{(d_t - d_s) v \rho}{\eta}\right\}^{0.38} \frac{d_s^{0.55}\ (d_t - d_s)^{0.62}}{d_t^{1.17}}$ $(\eta > 5 \times 10^{-3}\ \mathrm{N.s.m^{-2}})$

2.2 Derivation of a correlation for the heat transfer coefficient

In Chapter 1 it is stated that our study of a SSHE has been divided into three parts, viz. flow phenomena, power consumption and heat transfer. From Chapter 2.1 it appears that the only paper dealing with experiments on flow phenomena is that by Blaisdell and Zahradnik[16]. Their measurements of the axial temperature distribution are not accurate enough to provide information about the axial dispersion.

The information about the power consumption is also very poor[20,21]. Penney and Bell[26] mention the influence of variable clearance between scraper blade and heat transfer surface on the power consumption, but do not set up a model.

Much work has been published on the heat transfer aspects, and important points here are:

- The mean temperature difference in the SSHE. A mathematical model has been derived by Bott, Azoory, and Porter[28] for the influence of axial dispersion on the mean temperature difference and therefore on the effectiveness of heat transfer. However, no measurements of the dispersion coefficient are available.
- Penetration theory as a mechanism for heat transfer has been discussed by various authors[14,15,18,22,23]. The measured values of the heat transfer coefficient when viscous liquids are used as working fluid are always lower than calculated from a theory of penetration of heat followed by mixing.
- Heat transfer measurements are reported by various authors but the only extensive investigation using Votators is that by Skelland, Oliver and Tooke[18].

The latter work will now be considered more closely. For liquids with viscosities higher than 5 x 10^{-3} N.s.m^{-2} it was found:

$$\frac{\alpha_s d_t}{\lambda} = 0.014\left(\frac{c_p \eta}{\lambda}\right)^{0.96} \left\{\frac{(d_t-d_s)v\rho}{\eta}\right\}^{1.00} \left(\frac{d_t N}{v}\right)^{0.62} \left(\frac{d_s}{d_t}\right)^{0.55} n^{0.53} \qquad (7)$$

Although the investigation was systematic and exhaustive, the following objections can be made to the formulation of Eq. (7):

1. As the authors themselves state, the choice of the dimensionless groups is very arbitrary; other combinations can be selected as well.
2. The determination of the exponents in Eq. (7) is open to question.

The exponent of $\frac{d_t N}{v}$ has been determined as follows (see Fig. 3):
At constant $\frac{c_p \eta}{\lambda}$, $\frac{d_s}{d_t}$ and n, $\frac{\alpha_s d_t}{\lambda}$ is plotted against $\frac{d_t N}{v}$, with $\frac{(d_t-d_s)v\rho}{\eta}$ as parameter. The slope is dependent on $(d_t-d_s)v\rho/\eta$, and varies systematically between 0.45 and 0.72. In spite of this the slope is assumed to be constant (0.62).

A similar objection can be made for the determination of the exponent of $\frac{(d_t-d_s)v\rho}{\eta}$, where $\frac{\alpha_s d_t}{\lambda}\left(\frac{d_t N}{v}\right)^{-0.62}$ is plotted against $\frac{(d_t-d_s)v\rho}{\eta}$ with the shaft speed as parameter. The slope is dependent on the shaft speed and varies systematically, and it is therefore incorrect to take the mean value

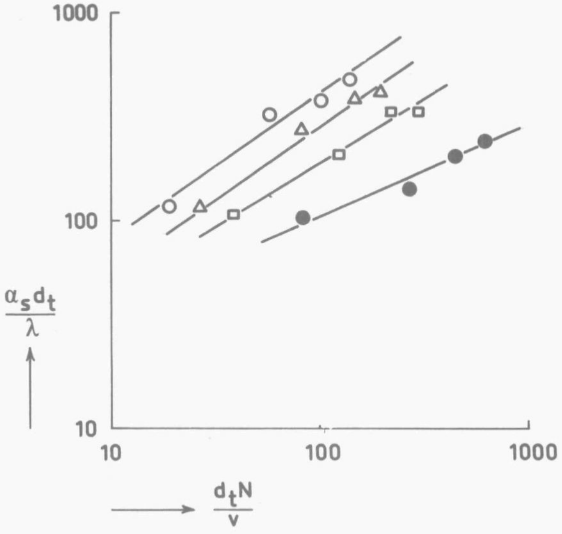

Fig. 3 Variation of Nusselt number $\frac{\alpha_s d_t}{\lambda}$ with $\frac{d_t N}{v}$.

$\frac{(d_t - d_s)v\rho}{\eta}$	Slope
○ 0.60	0.72
Δ 0.50	0.71
□ 0.30	0.61
● 0.15	0.45

Data from Skelland, Oliver and Tooke[18].

of 1.00 (see Fig. 4, full line).

3. The thermal conductivity, λ, occurs only with exponent 0.04 and therefore has hardly any effect on heat transfer. This is remarkable since the heat is largely transferred by conduction.

Because of the objections to Eq. (7) the results of the measurements will now be used to derive a new correlation for the heat transfer coefficient. The correlation is based on the penetration theory and an empirical correction factor. This correction term φ may be a function of λ, η, ρ, c_p, v, N, n, d_t, d_s. The correlation for the heat transfer coefficient now becomes:

$$\frac{\alpha_s d_t}{\lambda} = 1.13 \left(\frac{N d_t^2 \rho}{\eta} \cdot \frac{\eta c_p}{\lambda} \cdot n \right)^{0.5} \varphi \qquad (9)$$

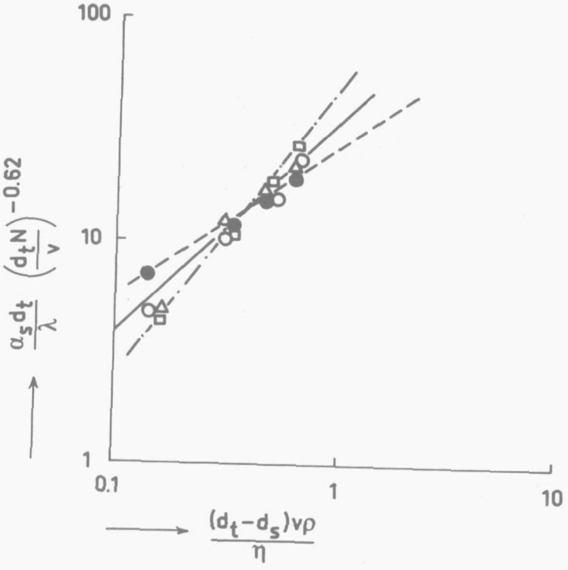

Fig. 4 Variation of the group $\frac{\alpha_s d_t}{\lambda}\left(\frac{d_t N}{v}\right)^{-0.62}$ with Reynolds number $\frac{(d_t-d_s)v\rho}{\eta}$.
Shaft speed (rev. min^{-1}): ○750, △560, □315, ●100.
Data from Skelland, Oliver and Tooke[18]

2.2.1 Influence of axial velocity and shaft speed

To determine the influence of the shaft speed and the axial velocity, the series of measurements was used in which these parameters were varied and Pr, d_s and n remained constant. From Eq. (9) it follows:

$$\varphi = \frac{Nu}{1.13\ (Re_R.Pr.n)^{0.5}} \tag{10}$$

In Fig. 5, 1-φ is plotted as a function of the Péclet number $\frac{(d_t-d_s)v}{a}$, with the shaft speed as parameter. The measurements made at 1.7 rev. s^{-1} give different results from those made at higher shaft speeds. This effect will be discussed in Chapter 5. The other measurements show that a variation in the speed from 5.2 to 12.3 rev. s^{-1} has hardly any influence on the correction factor . By adding 200 to Pe in Fig. 5a a straight line is obtained on double logarithmic scales (Fig. 5b). This figure shows that:

$$\varphi = 1 - \frac{g(\lambda, \eta, \rho, c_p, n, d_t, d_s)}{(Pe+200)^{0.18}} \tag{11}$$

The influence of axial velocity is given in Eq. (11). φ appears to be independent of shaft speed.

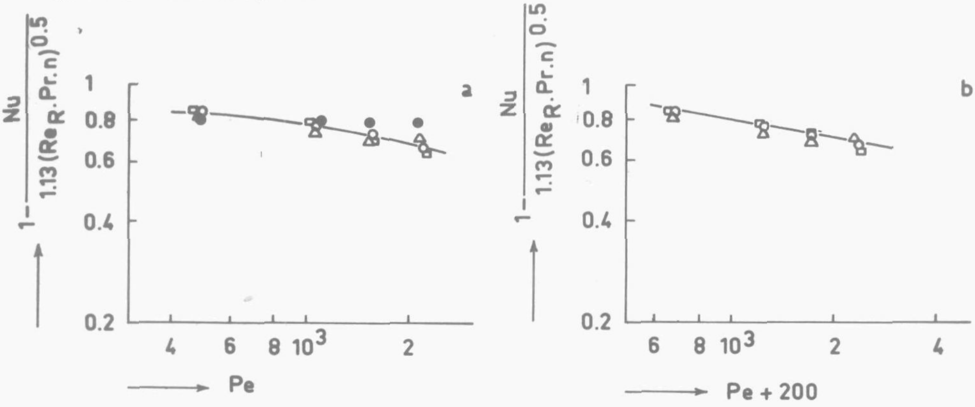

Fig. 5 Influence of the shaft speed on the variation of $1-\varphi$ with Péclet number. Shaft speed (rev./min^{-1}) O750, Δ560, □315, ●100.

a) As a function of Pe

b) As a function of Pe + 200

Data from Skelland, Oliver and Tooke[18].

2.2.2 Influence of number of rows of scraper blades

From the experiments, the following relation between heat transfer coefficient and number of blades was obtained:

$$Nu \sim n^{0.53}$$

This is in good agreement with the theoretical relationship, where

$$Nu \sim n^{0.50}$$

Therefore, the number of rows of blades is not included in the correction factor.

2.2.3 Influence of the annular space

Dimensional analysis shows that Eq. (11) can be written in the form:

$$\varphi = 1 - \frac{g\left(\frac{\eta\, c_p}{\lambda}, \frac{d_s}{d_t}\right)}{(Pe+200)^{0.18}}, \tag{12}$$

if one assumes that this correction factor is determined by kinematic effects only. From the measurements in which the shaft diameter was varied, the influence of d_s/d_t can be determined by plotting the correction term $1 - \varphi$ as a function of Pe, with d_s as parameter (Fig. 6). It appears that the influence of the annular space is completely included in the Péclet number: Fig. 6 shows the same pattern as Fig. 5b. Equation (12) can now be written as:

$$\varphi = 1 - \frac{g\left(\frac{\eta c_p}{\lambda}\right)}{(Pe+200)^{0.18}} \qquad (13)$$

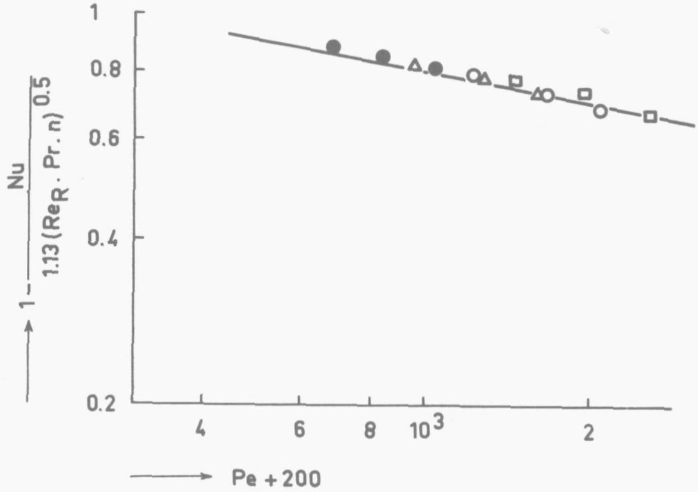

Fig. 6 Influence of the shaft diameter on the variation of 1-φ with Péclet number. Shaft diameter (mm): □25.4, O35.6, Δ45.7, ●57.1. Date from Skelland, Oliver and Tooke[18].

2.2.4 Physical properties of working fluid

The influence of physical constants of the fluid can be derived from the series of measurements with glycerol and glycerol/water mixtures. The experiments using liquids with viscosities lower than 2×10^{-3} $N.s.m^{-2}$ have been neglected, because in practice liquids that are heated or cooled in a SSHE will always have a viscosity which is considerably higher than that value.

In Fig. 7, 1-φ is again plotted against Pe, but now with Pr as parameter. The scattering is greater than in the previous figures but there are no

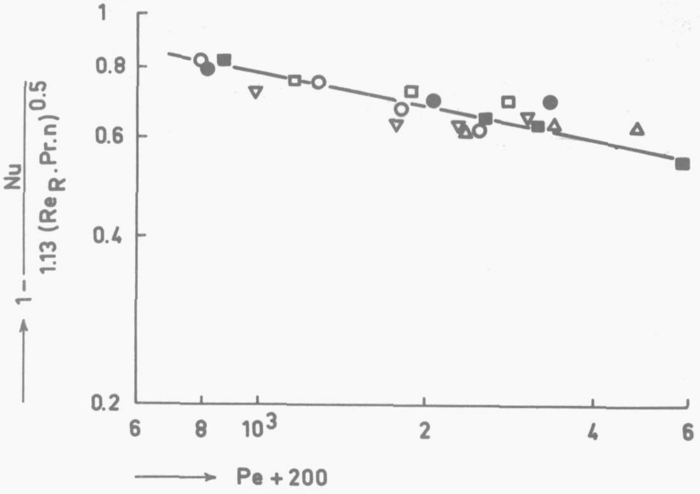

Fig. 7 Influence of the Prandtl number on the variation of $1-\varphi$ with the Péclet number. Prandtl number: ○ ca. 3300, □ ca. 2700, ● ca. 2000, △ ca. 1300, ■ ca. 1100, ▽ ca. 50. Data from Skelland, Oliver and Tooke[18].

significant differences in the various Prandtl numbers. It would appear that the influence of the physical properties of the material is sufficiently expressed in the Péclet number.

2.2.5 The complete correlation

From the foregoing reasonings we obtain the following correlation for the heat transfer coefficient in the Votator used by Skelland, Oliver and Tooke[18] (for $400 < Pe < 6000$):

$$Nu = 1.13\ (Re_R.Pr.n)^{0.5}\left\{1-2.78(Pe+200)^{-0.18}\right\} \tag{14}$$

The standard deviation from Eq. (14) is 12 percent. For the correlation of Skelland, Oliver and Tooke[18], Eq. (7), this is 17 percent.

If the product $Re_R.Pr.n$ in Eq. (14) is considered as one dimensionless group, the heat transfer can be described by three dimensionless groups. In the original equation six dimensionless groups occur.

CHAPTER 3

FLOW PHENOMENA

In this chapter various aspects of the flow in a SSHE will be discussed. A study of the flow pattern is important for various reasons:

- In order to ensure a high heat transfer coefficient and hence a high temperature gradient at the heat transfer wall, the temperature of the liquid that contacts the wall after the blade has passed should be as close to that of the bulk liquid as possible. This process is influenced by the distribution of the liquid scraped off the wall over the bulk of the liquid in the annular space. This distribution is determined by the flow pattern.
- The flow pattern determines the shear stresses in the liquid and therefore the power dissipation.
- Axial dispersion, which is a flow phenomenon, decreases the driving force for heat transfer[28].
- The mixing performance of a SSHE is clearly dependent on the flow.
- The residence time distribution and the temperature histories of liquid particles passing through the SSHE are determined by the flow pattern. If the SSHE is used as a crystallizer or as a sterilizer these aspects are very important.

The tangential velocity in a SSHE is usally much higher than the axial velocity. Therefore the flow pattern in a plane perpendicular to the axis was studied first, the axial velocity being zero. For these studies a short length perspex model was used. The streamlines and velocity profiles were observed and photographed. In addition, residence time distributions were determined experimentally, under various operating conditions, in a SSHE of pilot plant size. Finally, dispersion measurements were carried out in a SSHE of the same dimensions. The outer wall consisted of a glass tube, through which a dye could be injected.

3.1 Flow studies in a plane perpendicular to the axis

A survey of the flow in an annulus with rotating inner cylinder is given by Van Lookeren Campagne[30]. Different flow regimes were distinguished for increasing rotational Reynolds numbers:

- Couette flow. This is simple shear flow in which the axial and radial velocity components are zero.
- Taylor vortices. Large secondary toroidal vortices are formed which occur in pairs with opposite rotation. The diameter of a vortex is approximately equal to the width of the annular space.
- At higher rotational Reynolds number the vortices change in shape until a regular pattern of large secondary vortices is formed in a turbulent tangential flow field. At even higher Reynolds numbers, the regular pattern is disturbed and even at very high Reynolds numbers large secondary vortices are still present in the annulus.

The transition from Couette flow to Taylor vortices takes place at a Reynolds numbers for rotation defined by[30]:

$$\frac{N\,d_s(d_t-d_s)\rho}{4\eta} = \left[\frac{\pi^4\left(0.5+\dfrac{d_s}{d_t-d_s}\right)}{0.0571\left(1-\dfrac{0.652\,(d_t-d_s)}{d_s}\right)+0.00056\left(1-\dfrac{0.652\,(d_t-d_s)}{d_s}\right)^{-1}}\right]^{\frac{1}{2}}$$

This critical Reynolds number is in the range of operating conditions that are usually applied to a SSHE. In our SSHE with glass outer wall (see Chapter 3.3), Taylor vortices were visualized by dispersing small polyethylene beads in the working fluid. The transition from Couette flow to Taylor vortices could not be observed very accurately, but a deviation from the above equation could not be observed. The values of Re_R at which the transition takes place are given in Table 5.

Table 5

Critical Reynolds numbers for various shaft diameters (d_t = 76 x 10^{-3} m) in a SSHE with rotating inner cylinder

Shaft diameter (10^{-3} m)	Re_R (theoretical)
46	200
56	280
62	415
68	870

Critical Reynolds numbers for SSHEs with rotating outer cylinders are much higher. The study of the flow pattern in a plane perpendicular to the axis, described in the following sections is restricted to the Couette flow regime.

3.1.1 Equipment details

Most of our experiments on heat transfer and power consumption were performed in a SSHE described in Chapter 3.2.2. The inside diameter of the heat transfer tube was 76 x 10^{-3} m and various shaft diameters were available for study. The number of rows of scraper blades can be varied between one and six. For the study of the flow pattern a shaft diameter of 56 x 10^{-3} m was selected, thus giving an annular space of 10^{-2} m. Two rows of scraper blades were used.

The linear dimensions of the model that are mentioned above were doubled in order to facilitate the determination of the velocity profile. This does not change the flow pattern in the case of laminar flow. The length of this model was much smaller than that of the SSHE used for the power consumption and heat transfer experiments, viz., twice the annular space and hence 40 x 10^{-3} m. The tangential velocities equidistant from the front and back plane in this case do not deviate by more than approximately 10 percent from those in a long SSHE, as is shown in the Appendix (Chapter 7.1).

The front and back walls, as well as the shaft, of the SSHE were made of perspex. Chromed brass was used for the outer tube and scraper blades. Two types of scraper blades were used, viz., a cutaway type and a closed type that prevents leakage between shaft and blade. Instead of rotating the shaft and the blades, which is the way a SSHE usually operates, these parts were kept stationary in the model and the outer wall was rotated. The flow pattern is the same in both cases as can be seen from the following: Suppose that an observer moves in a circular path at the same velocity as the model's outer wall. He will, in fact, see a stationary wall and a rotating shaft. This is only true in the absence of Taylor instability. The outer wall was rotated using a V-belt and a variable speed motor. This enabled the outer wall to be rotated between 0.17 and 1.7 rev. s^{-1}. By using liquids of low viscosity high values of Re_R could be obtained, in spite of the low shaft speeds. Coloured liquid was introduced in the annular space by means of a syringe fitted with a capillary injection device. The open end of the capillary could be positioned anywhere in the plane equidistant from the front and the back plane of the model.

Streamlines were photographed with an Exacta Varex camera. A tele-objective (focal length 0.200 m) was used to reduce distortion and back-lighting was utilized to eliminate reflection. A photograph of the model is shown in Fig. 8 and a sketch of the experimental set-up in Fig. 9.

3.1.2 Experimental procedure

Experiments were conducted with two glycerol/water mixtures, having viscosities of 0.1 and 0.8 N.s.m^{-2}, and with silicon oil, having a viscosity of 12 N.s.m^{-2}. Streamlines were visualized by a coloured liquid injected whilst the outer wall was rotating. These tracing liquids were made from the working mixtures by dissolving methylene blue in the glycerol/water mixtures and sudan red in the silicon oil. The liquid was injected at various positions in the plane equidistant from the front and the back wall of the model.

To determine the velocity at any point in the model a small drop (ca. 1×10^{-3} m diameter) of coloured liquid was injected at that point. The outer wall was stationary during the injection. The outer wall was then rotated manually through about 20 degrees. Before and after the rotation a photograph was taken. The displacement of the drop of coloured liquid, relative to the displacement of the wall, is equal to the ratio of the velocity at the position of the drop and the wall velocity during steady rotation of the outer wall of the model (see the Appendix, Chapter 7.2).

3.1.3 Streamlines

The experiments with liquids having viscosities between 0.1 and 12

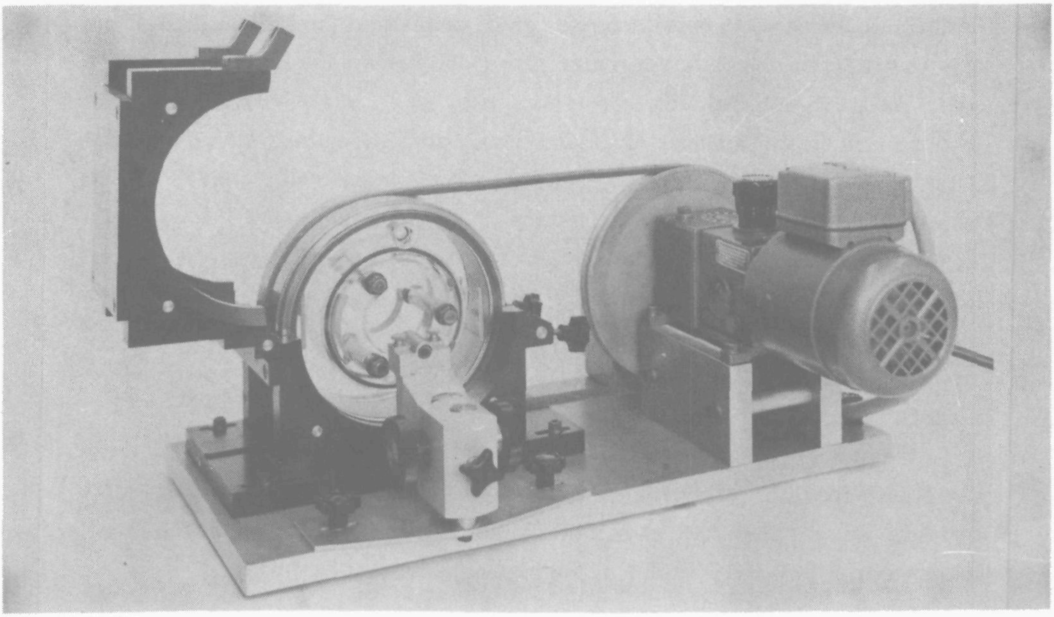

Fig. 8 SSHE-model used for studying the flow pattern in a plane perpendicular to the axis.

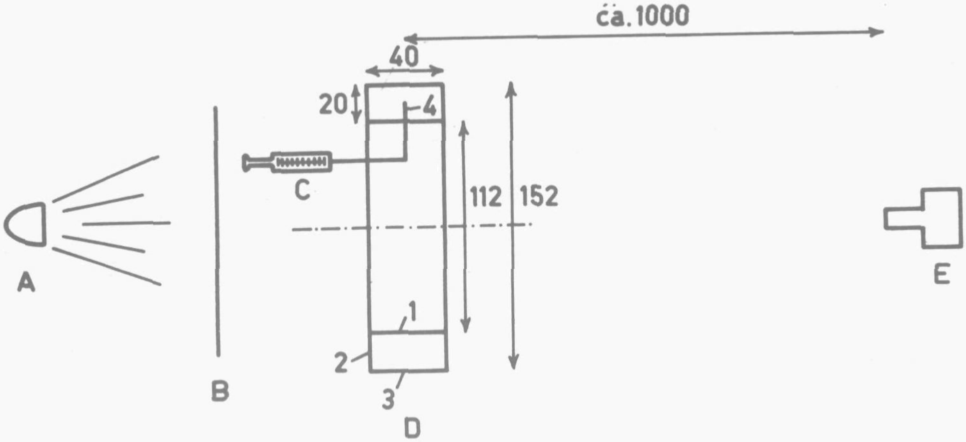

Fig. 9 Schematic view of experimental set-up for studying the flow in a plane perpendicular to the axis. Dimensions in mm. A lamp; B diffusive screen; C syringe; D SSHE-model: 1 shaft (stationary); 2 side wall (stationary); 3 outer wall (rotating); 4 capillary for colour injection; E camera.

$N.s.m^{-2}$ did not show any influence of the viscosity on the tangential velocity profile. The only difference that could be observed was in the secondary flow, which is caused by centrifugal forces. The tangential velocity, and hence the centrifugal force, is greater in the plane equidistant from the front and the back wall than close to these walls. Therefore, a secondary flow pattern develops that has an outward direction in the plane under study and an inward direction in the area close to the end walls. This results in streamlines which are not concentric circles (apart from the blade area) but are spirals. The pitch of the spiral is dependent on the fluid viscosity and varies between ca. 3×10^{-3} m for 0.1 $N.s.m^{-2}$ and an negligeable value for 12 $N.s.m^{-2}$. The influence of this secondary flow on the velocity profiles measured is small.

The rotational speed of the tube wall was varied between 0.17 and 1.7 rev. s^{-1}. No change in tangential velocity profile was observed, apart from the presence of a small vortex between the back of the blade and the wall at the higher rotational speeds.

In further experiments on streamlines and velocity profiles glycerol/water mixtures ($\eta = 0.8$ $N.s.m^{-2}$) were mainly studied at a rotational speed of 0.18 rev. s^{-1}.

Photographs of the streamlines are given in Figs. 10-12, Fig. 10 showing

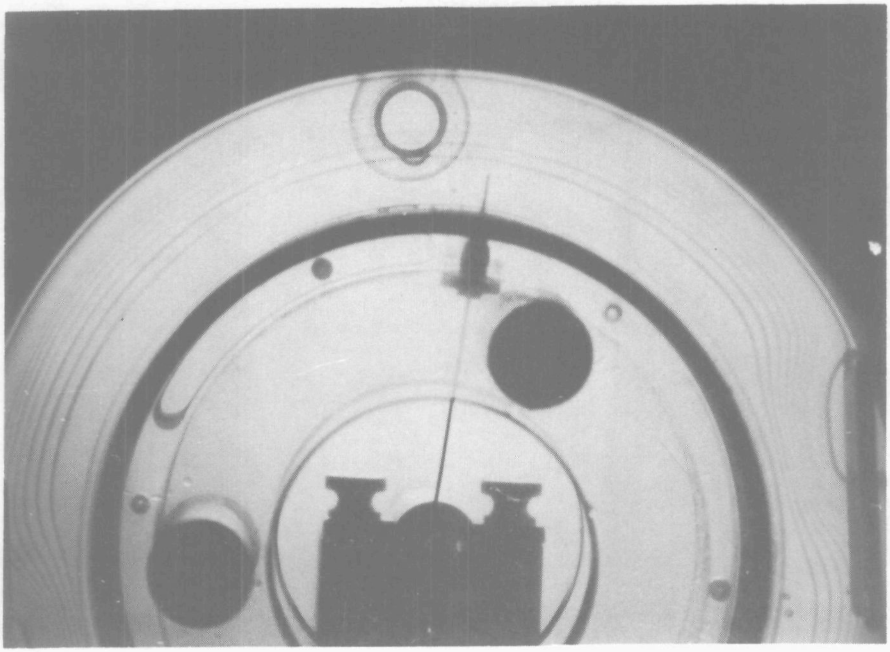

Fig. 10 Streamline pattern for a SSHE with cutaway blades.

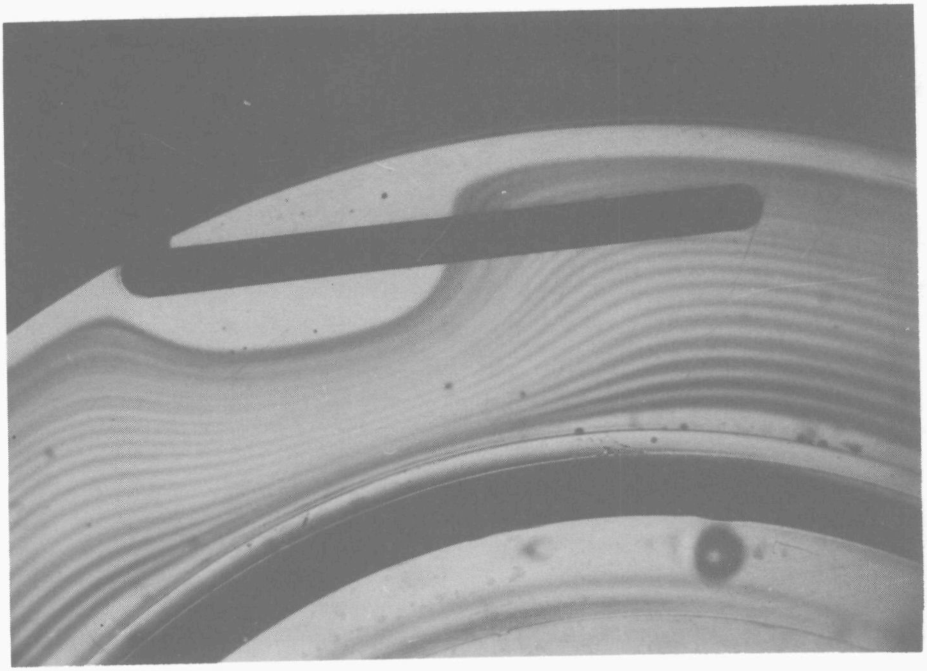

Fig. 11 Streamlines in the area close to the blades.

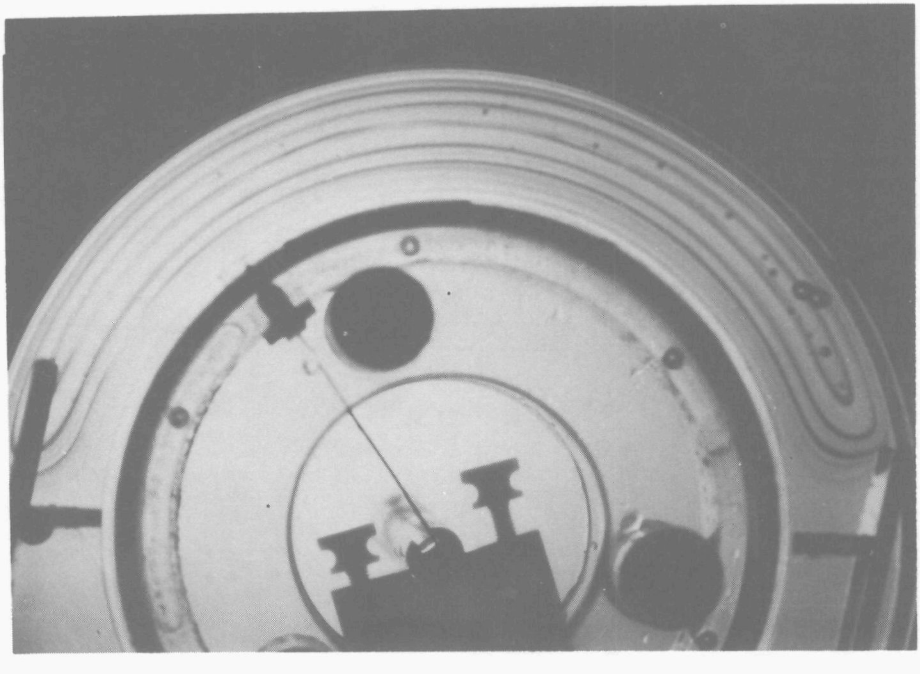

Fig. 12 Streamlines for a SSHE with closed blades (no leakage between blade and shaft).

the streamlines produced by the cutaway blades. The photographs clearly show that the flow is laminar. The streamlines are concentric circles in the major part of the annulus (if the secondary flow is neglected). In the proximity of the blades the flow contracts and expands again without mixing. Fig. 11 shows a close-up of the blade area. For closed blades (no leakage between blade and shaft), the flow pattern is illustrated in Fig. 12. The streamlines are closed loops in the areas between two blades.

3.1.4 Velocity profile

Velocity profiles were determined by the method described in Chapter 3.1.2. Fig. 13 shows the drops of coloured liquid injected with the syringe. In Fig. 14 the position of the drops after a rotational movement of the outer wall of the model is shown. The tangential velocity profile is immediately apparent in the photograph. Velocity profiles for cutaway and closed blades were determined in this way, both in the undisturbed annulus and in the area close to the blades.

The functional form of the velocity profile will now be derived. Assuming that the radial and axial velocities are zero and allowing for a constant tangential pressure gradient, the tangential component of the equation of motion in cylindrical coordinates becomes:

$$\frac{d}{dr}\left\{\frac{1}{r}\frac{d}{dr}(rv_\theta)\right\} = \frac{1}{r}\cdot\frac{1}{\eta}\frac{dp}{d\theta} \tag{15}$$

$\frac{1}{\eta}\frac{dp}{d\theta}$ is constant, but not known. Eq. (15) can be integrated to give:

$$\begin{aligned} v_\theta &= \frac{1}{\eta}\frac{dp}{d\theta}\left(\frac{r}{2}\ln r - \frac{r}{4}\right) + C_1 r + \frac{C_2}{r} \\ &= C_3 r + \frac{C_2}{r} + C_4 r \ln r \end{aligned} \tag{16}$$

with: $\frac{dp}{d\theta} = 2\,\eta\,C_4$

In the case of cutaway blades there are two boundary conditions, viz., $v_\theta = 0$ at $r = \frac{1}{2}d_s$ and $v_\theta = v_o$ at $r = \frac{1}{2}d_t$. A theoretical solution requires three boundary conditions. The third one is that the integral of the pressure along a closed streamline is zero. This condition cannot be evaluated, as the flow pattern in the blade area is not given by Eq. (16).

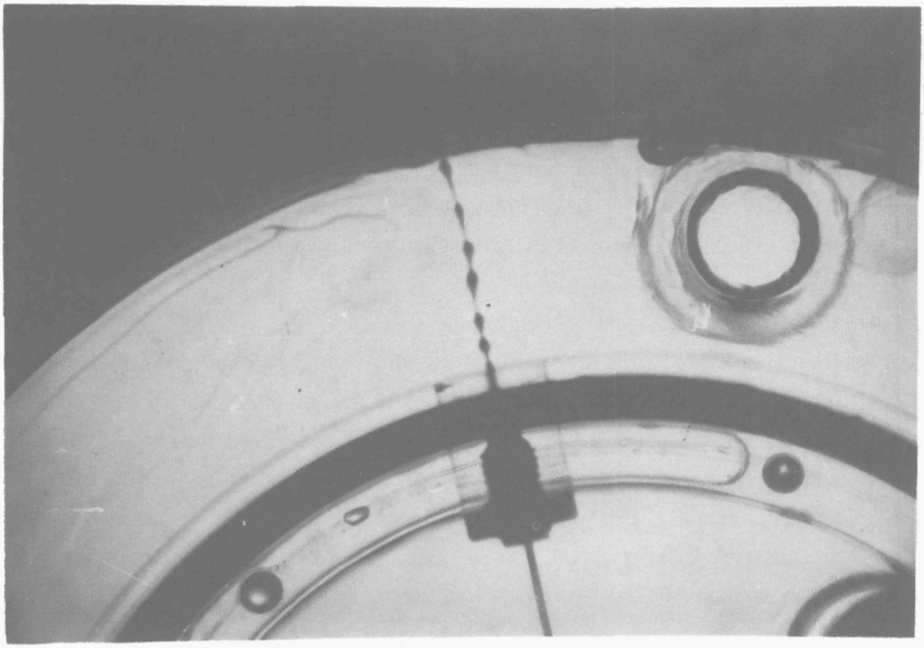

Fig. 13 Position of tracer liquid before rotational movement.

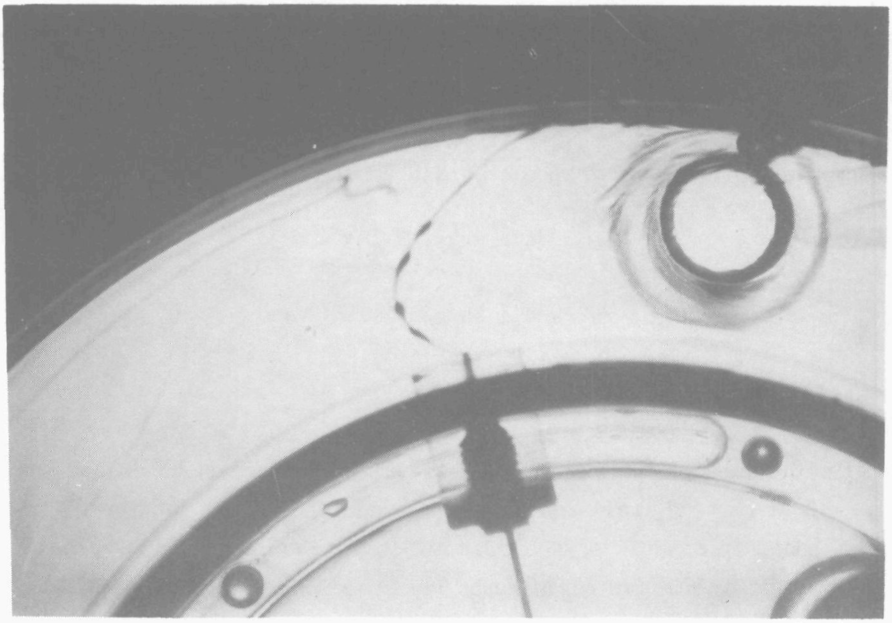

Fig. 14 Position of tracer liquid after rotational movement.

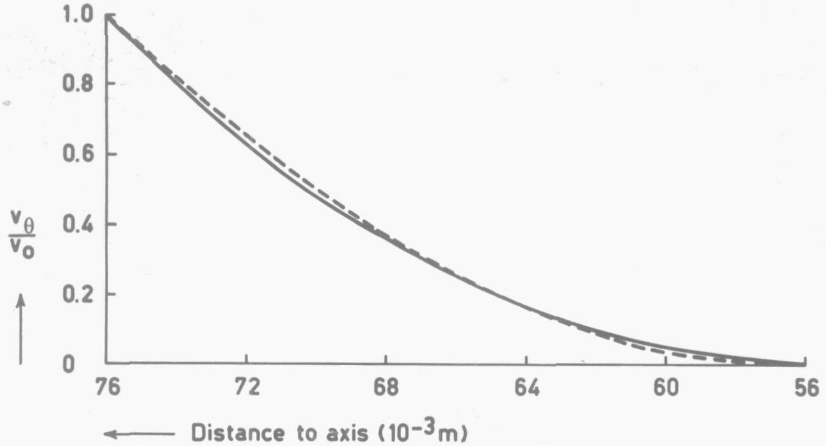

Fig. 15 Tangential velocity versus distance to the axis for cutaway blades. Full line: measured; dotted line: according to Eq. (17).

Fig. 15 shows the experimental velocity profile for cutaway blades. The theoretical equation (16) can be matched to the experiments by imposing the condition that at $r = \frac{1}{4}(d_t + d_s)$ the value of v_θ, as calculated from Eq. (16) should be equal to the experimentally determined value. With this additional condition the constants in Eq. (16) can be calculated:

$$\frac{v_\theta}{v_o} = \frac{289.404}{r} - 0.82186\ r + 0.181246\ r \ln r \quad \text{(r in mm)} \tag{17}$$

This equation is also shown in Fig. 15.

The velocity profile for closed blades can be derived theoretically. Eq. (16) is still valid, as also are the boundary conditions at $r = \frac{1}{2} d_s$ and $r = \frac{1}{2} d_t$. There is a third additional condition, because the net flow through a plane θ = constant is now zero as there is no leakage between blade and shaft. The three constants can be evaluated from these three conditions:

$$\frac{v_\theta}{v_o} = \frac{982.00}{r} - 2.37374\ r + 0.51191\ r \ln r \quad \text{(r in mm)} \tag{18}$$

The experimental and theoretical velocity profiles are shown in Fig. 16. The maximum difference between the two lines is 15%. Fig. 17 gives the velocities of the liquid in the area near the blades. The arrows reflect vector quantities and indicate the value of the velocity. From the velocity profiles

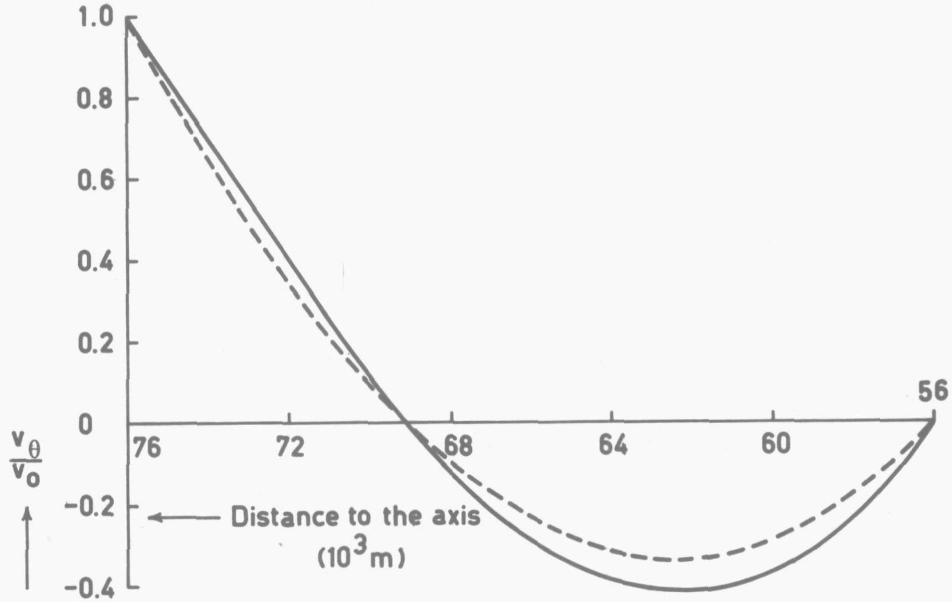

Fig. 16 Tangential velocity versus distance to the axis for closed blades. Full line: measured, dotted line: according to Eq. (18).

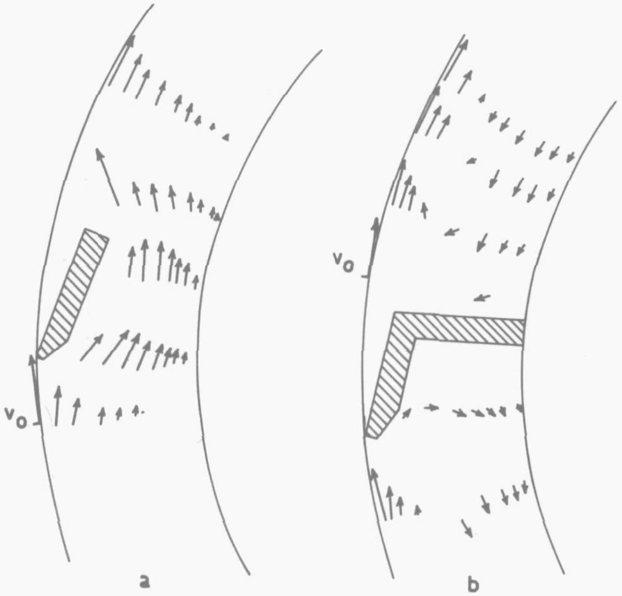

Fig. 17 Velocities of the liquid in the area near the blades. a) cutaway blades; b) blades with no leakage. v_o = wall velocity.

the tangential pressure gradient can be calculated by using the equation of motion (15). In the special case of the model SSHE with the cutaway blades, it follows that:

$$\frac{dp}{d\theta} = 173 \ \eta N \tag{19}$$

In the same way for the closed blades it follows that:

$$\frac{dp}{d\theta} = 490 \ \eta N \tag{20}$$

An experiment was conducted to check the calculations of the pressure gradient. Two small holes, 0.435 of the circumference apart, were drilled in the shaft of the model. With closed blades, a shaft speed of 1 rev. s^{-1} and $\eta = 0.24$ N.s.m^{-2}, the previous calculation predicts a pressure difference (Δp) between these points of 322 N.m^{-2}. A measurement made with a manometer revealed 330 N.m^{-2} indicating good agreement between experiment and theory.

3.2 Residence time distribution

3.2.1 Introduction

The residence time of the liquid elements flowing through a SSHE is not uniform. This is caused partly by the differences in velocity along and in the length of different streamlines and partly by dispersion due to vortices and a pumping effect caused by the scraper blades.

First the residence time distribution caused by the velocity profile will be considered. The flow in an annulus is similar to flow between two flat plates if the annular space is small with respect to the outer diameter. If the fraction of the total flow with a residence time less than θ is given by $F(\theta)$ and the fraction of the total flow having residence times between θ and $\theta + d\theta$ is given by $E(\theta)d\theta$ (θ is the normalized time based on the average residence time $\tau = \int_0^\infty tE(t)dt$), then for a narrow annulus the following is valid[31,32]:

$$\left.\begin{aligned} E(\theta) &= 0 \ \text{ for } \ 0 < \theta < 2/3 \\ E(\theta) &= \frac{1}{3\theta^3} \ \frac{1}{(1 - \frac{2}{3\theta})^{\frac{1}{2}}} \quad \text{for } \theta > 2/3 \end{aligned}\right\} \tag{21}$$

and:

$$\left.\begin{aligned} F(\theta) &= 0 \qquad \text{for } 0 < \theta < 2/3 \\ F(\theta) &= \left(1 - \frac{2}{3\theta}\right)^{\frac{1}{2}} \left(1 + \frac{1}{3\theta}\right) \text{for } \theta > 2/3 \end{aligned}\right\} \qquad (22)$$

For an annulus that is not infinitely narrow, the breakthrough point will be lower than $\theta = 2/3$.

If there is a dispersion in the SSHE due to vortices or a pumping effect the residence time distribution is not given by these equations. Many models are available in the literature to describe non-ideal flow patterns. The two most widely used are the plug flow with dispersion model and the tanks-in-series model[33]. Important parameters of the E-functions belonging to these models are the relative standard deviation σ, where $\sigma^2 = \{\Sigma\ (\theta-1)^2 E\}/\Sigma E$, and the relative skewness ν, where $\nu^3 = \{\Sigma\ (\theta-1)^3 E\}/\Sigma E$. One can distinguish between the models[34] by calculating the control parameter σ^4/ν^3 (see Table 6).

Table 6

Properties of flow models

Flow model	σ	ν	$\frac{\sigma^4}{\nu^3}$
Tanks in series	$\frac{1}{\sqrt{n_T}}$	$2^{1/3}\ \sigma^{4/3}$	0.5
Plug flow with dispersion (large $\frac{Lv}{D_E}$)	$\sqrt{\frac{2D_E}{Lv}}$	$3^{1/3}\ \sigma^{4/3}$	0.33
Streamline flow Eq. (21)	∞	∞	0

3.2.2 Equipment

For the measurements of the residence time distributions the same SSHE as for the power consumption and heat transfer measurements has been used. This apparatus (see Fig. 1) has a length of 0.46 m and an inside diameter of 0.076 m. The scraped heat transfer surface is 0.108 m^2. Shaft diameters of 0.046, 0.056, 0.062 and 0.068 m could be used. The shaft speed, which was measured with an electric meter could be varied between 3.3 and 33 rev. s^{-1}. The shaft could be fitted with 1, 2, 3, 4 or 6 rows of stainless steel scraper blades, each row consisting of two blades with a total length of 0.448 m. The scraper blades were pressed against the chromium plated mild steel wall by centrifugal force and the resistance of the fluid. The heat transfer medium was circulated around the heat transfer tube in a rectangular ($18 \times 7 \times 10^{-6}$ m^2), spiral-shaped coil in countercurrent to the working fluid.

The working fluid was stored in a jacketed stirred vessel (see Fig. 18, No. 1). By controlling the temperature of the jacket, the temperature of the working fluid could be kept at a desired value. The liquid was pumped to the SSHE by means of one or two gear pumps with variable speed drive; the flow could be varied between 0.8×10^{-5} and 0.45×10^{-3} $m^3.s^{-1}$. By means of a three-way valve the fluid could either be led back to the storage vessel or drawn off for weighing or sampling.

The pressure of the working fluid could be measured between the pump and the SSHE; the temperature, before and after the SSHE, by a mercury-thermometer in a pocket. The torque applied to the drive shaft of the SSHE was measured with a momentmeter (Staiger-Mohilo, see Fig. 18, No. 3). Just before the SSHE, a syringe (Fig. 18, No.4) was fitted to the working fluid line to inject a tracer liquid. A rotating sampling device with 30 trays (Fig. 18, No. 6) was used for semi-continuous sampling of the working fluid.

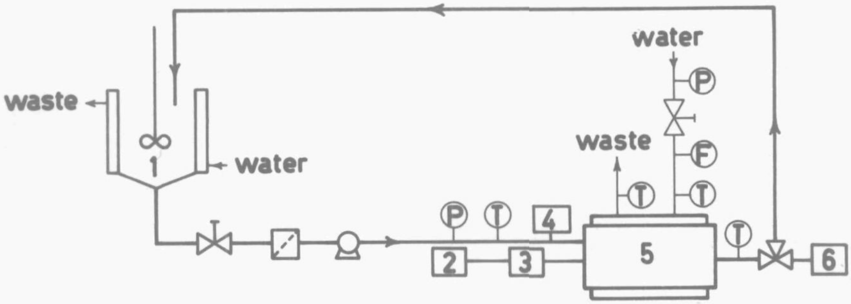

Fig. 18 Flowsheet of the apparatus used.

1. Storage vessel with jacket and stirrer
2. Variable speed drive
3. Torque meter
4. Syringe
5. SSHE
6. Sampler.

3.2.3 Method for measuring residence time distributions

All residence time distribution measurements were conducted adiabatically using the 56 x 10^{-3} m shaft with two rows of scraper blades. Glycerol/water mixtures were used as working fluids. The tracer liquid was a solution of methylene blue in the same fluid. From the colour intensity of a mixture of working fluid and tracer the concentration of the latter was determined by means of a Klett colorimeter.

Three methods for measuring the residence time distribution were used:

- The response to a step input. The SSHE was filled with tracer liquid. From time t = 0 this liquid was replaced by uncoloured liquid that was pumped into the SSHE. The flow from the SSHE was caught in the sampling device. In this way the F-curve (see Chapter 3.2.1) was determined.
- The response to a pulse input. During normal operation of the SSHE an amount of tracer was injected manually with a syringe in a very short time (a few tenths of a second). The flow from the SSHE was again sampled. If the E-curve resulting from these measurements showed a sharp peak, the experiment was repeated, this time samples being taken more frequently. The shape of the peak was determined more accurately in this way.
- The former method was modified to reduce the error caused by the imperfection of the pulse: The SSHE was filled with working fluid. A small plug of tracer liquid was introduced into the pipe line just before the SSHE, after which the pump was started.

The three methods gave the same results. Therefore, for most of the measurements the pulse injection system was used, since this was the fastest method and the contamination of the working fluid by the tracer was small. The measured curves were normalized to give the required E-curves.

3.2.4 Results

Residence time distributions were measured under the five different operating conditions given in Table 7. During all experiments the mass flow rate was 0.0355 $kg.s^{-1}$.

Table 7

Operating conditions for the residence time distribution measurements.

Expt. number	Shaft speed $\mathrm{rev.s^{-1}}$	Viscosity $\mathrm{N.s.m^{-2}}$
1	8.0	0.200
2	32.	0.090
3	4.0	0.084
4	30.4	0.~~0~~623
5	4.0	1.00

In experiments 1, 3 and 4 the shaft speed to viscosity ratios do not vary considerably. The E-curves for these conditions are given in Fig. 19. The above-mentioned ratio changes by two orders of magnitude in experiments 2

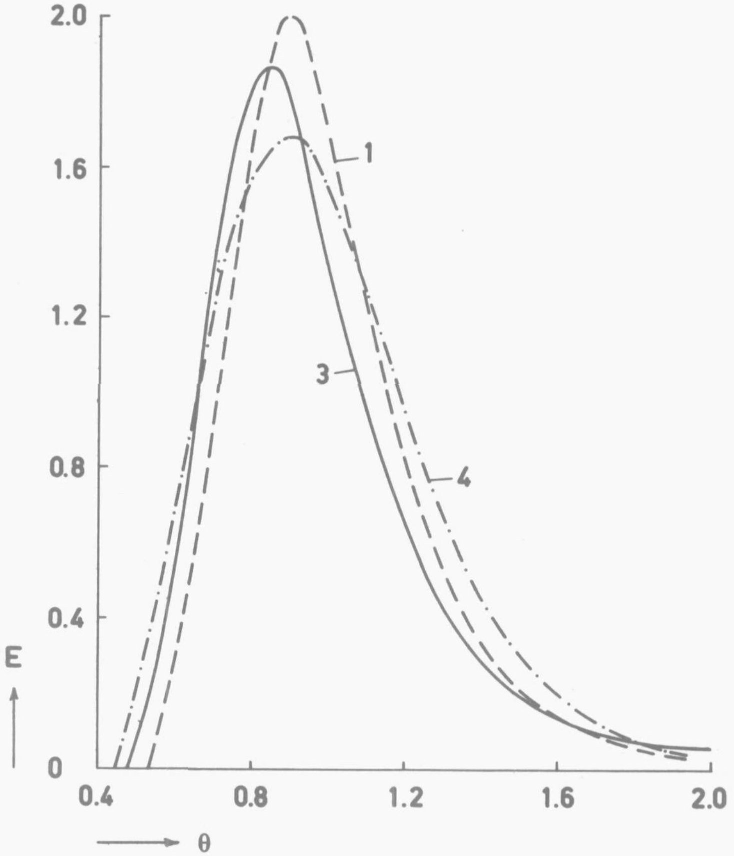

Fig. 19 Residence time distribution curves for experiments 1, 3 and 4.

and 5. The corresponding E-curves are compared with that of Expt. 3 in Fig. 20. In this figure the E-curve for the flow between two flat plates (Eq. (21)) has also been drawn.

For measurement 1 the tail of the curve was extrapolated and the standard deviation was determined, giving $\sigma^2 = 0.074$. ν^3 was determined in the same way: $\nu^3 = 0.035$. The value of the control parameter σ^4/ν^3 was

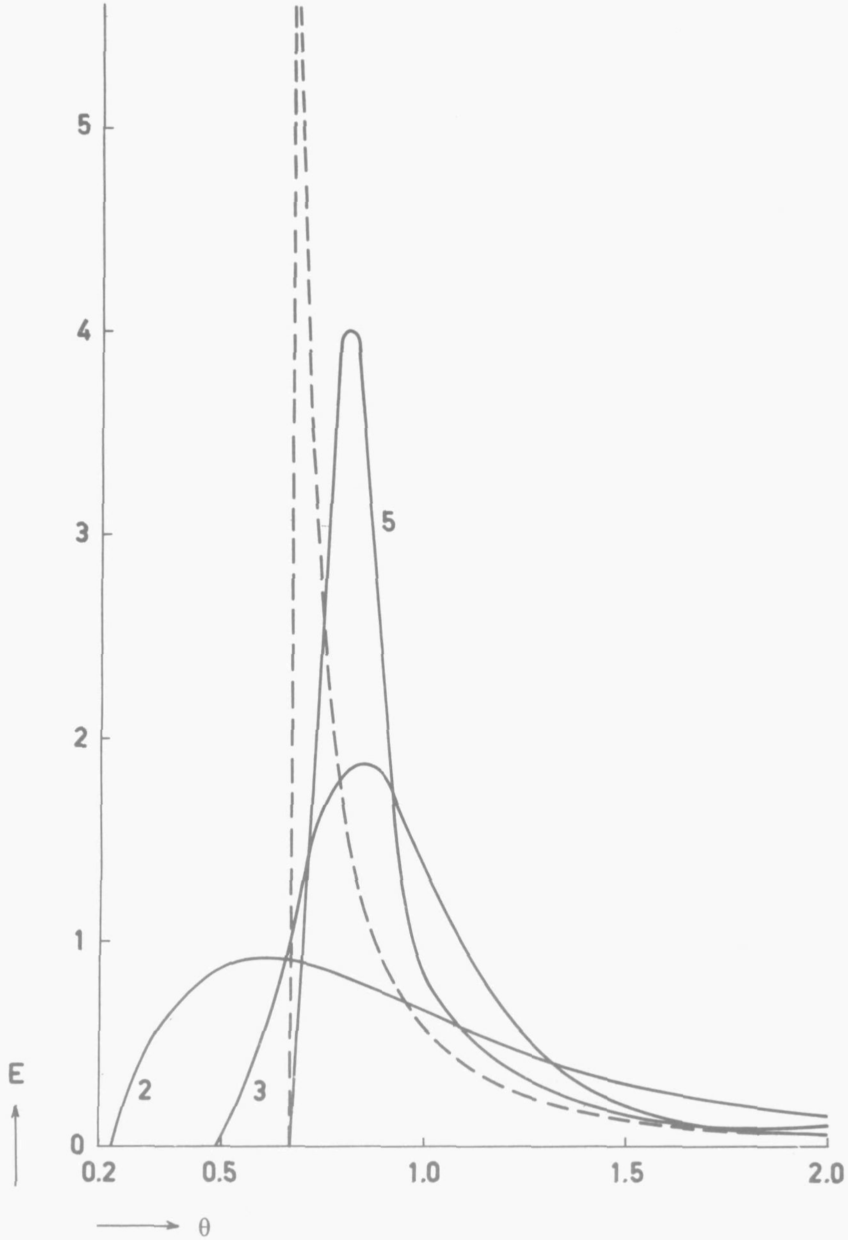

Fig. 20 Residence time distribution curves for experiments 2, 3 and 5. Dotted line: curve for flow between flat plates.

therefore 0.16, indicating that both differences along and in the length of streamlines, as well as dispersion mechanisms due to vortices and pumping action, are important (compare Table 7).

If one seeks to interpret both causes for residence time differences with a dispersion coefficient, one calculates, on the basis of the reported value of $\sigma^2 = 0.074$ a value of $D_E = 2.3 \times 10^{-4}$ $m^2 . s^{-1}$.

3.3 Axial dispersion measurements

We attempted to measure the axial dispersion in a situation with zero mass flow. In that case the influence of the contribution of differences in velocity along and in the length of streamlines on the mixing performance is absent and a true dispersion mechanism (due to vortices and a pumping action) can be measured.

For these experiments the SSHE was equipped with a glass outer wall. A hole was drilled in the wall at about a quarter of the way along the SSHE. A small pressure vessel that could be filled with tracer liquid was connected to the opening via a valve. The 56×10^{-3} m shaft, with two rows of scraper blades, was used for these measurements. The shaft speed was 10 rev. s^{-1}. Glycerol/water mixtures of two different concentrations were used, their viscosities under the operating conditions being 0.06 and 0.45 $N.s.m^{-2}$. A solution of methylene blue was injected into the working fluid through the hole in the SSHE wall while the shaft was being rotated manually at a low speed. In this way a complete ring of the tracer fluid was formed. The shaft was then rotated by means of the electric motor. The coloured ring spread out and the displacement of the boundary between coloured and uncoloured liquid was measured as a function of time.

If the axial dispersion can be described by Fick's law, the concentration profile can be determined from:

$$\frac{\partial C}{\partial t} = D_E \frac{\partial^2 C}{\partial z^2} \qquad (23)$$

with: $C = 0$ at $t = 0$ for $z > 0$

$C = C_o$ at $z = 0$ for $t \geqslant 0$

The solution of this equation is

$$C = C_o \operatorname{erfc} \frac{z}{2\sqrt{D_E t}}$$

or, if the error function is approximated by a linear function:

$$C = C_o \left(1 - \frac{z}{2\sqrt{D_E t}}\right) \quad \text{for } z < 2\sqrt{D_E t}$$

and $$C = 0 \quad \text{for } z > 2\sqrt{D_E t}$$

The position of the boundary between coloured and uncoloured liquid is therefore given by $z = 2\sqrt{D_E t}$.

If z is plotted vs. $\sqrt{t}$, the value of the axial dispersion coefficient can be determined from the graph. The measurement is not very accurate, because the boundary between coloured and uncoloured liquid is not sharp. There is wide scattering of the measuring points and therefore no difference between the two glycerol/water mixtures can be determined.

In Fig. 21 the position of the boundary between coloured and uncoloured liquid is plotted against the square root of the time. From this graph the dispersion coefficient was estimated to be $8 \times 10^{-4}\ m^2.s^{-1}$.

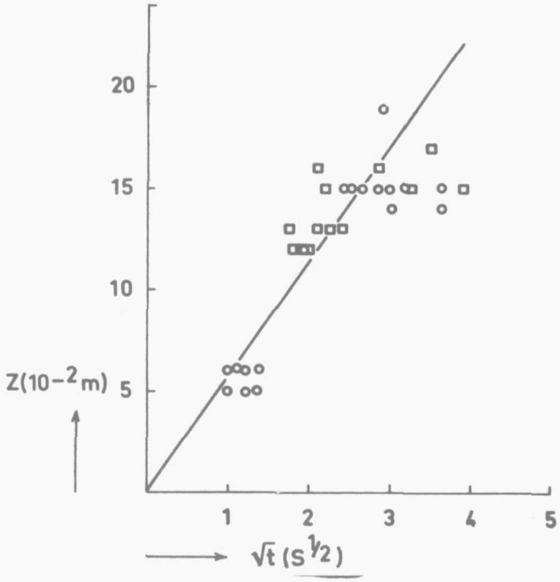

Fig. 21 Position of the boundary between coloured and uncoloured liquid as a function of time.
O 0.060 $N.s.m^{-2}$, □0.45 $N.s.m^{-2}$.

3.4 Conclusions on residence time distribution and axial dispersion

The residence time distribution of the flow between concentric cylinders with the inner cylinder rotating can be described with the plug flow with dispersion model, as was shown by Van Lookeren Campagne[30]

For the SSHE this model is not valid as the value of the control parameter σ^4/ν^3 is much lower than 0.33. Figs. 19 and 20 show that the ratio of shaft speed to viscosity has considerable influence on the E-curve. The residence time distribution is much wider for a low shaft speed and high viscosity than for a high shaft speed and low viscosity.

Although the plug flow with dispersion model does not fully describe the flow, it may be expected that axial dispersion decreases the heat transfer rate as has been described in Chapter 2.1. In chapter 3.2.4 a case has been reported for which $\sigma^2 = 0.074$ or $Pe_D = 27$. This results, with $\alpha_s = 2000$ $W.m^{-2}.\,{}^oC^{-1}$, $A = 0.108\ m^2$, $\varphi_m = 0.035\ kg.s^{-1}$ and $c_p = 2500\ J.kg^{-1}.{}^oC^{-1}$. in $N_T = 2.5$; Fig. 2 shows that in such a case the heat transfer coefficient calculated from experiments with the use of the plug flow model is 10% too low. In most heat transfer experiments the mass flow rate was so high (small values of N_T) that the plug flow model could be used in evaluating the experiments.

CHAPTER 4

POWER CONSUMPTION

This chapter deals with our measurements of power consumption in a SSHE. From the experimental results a theoretical model and an empirical equation for the power consumption have been derived.

4.1 Experimental procedure

The equipment used for measuring the power consumption is described in Chapter 3.2.2. Measurements were performed with all four available shafts, equipped with two, four, or six rows of scraper blades. The shaft speed was varied between 4.0 and 33.3 $rev.s^{-1}$. Three different glycerol/water mixtures, having viscosities at the operating temperatures of 0.1, 0.5 and 1.5 $N.s.m^{-2}$, were used as working fluids. The fluid was circulated through the uncooled SSHE and the temperatures at inlet and outlet were measured. To calculate the power input to the shaft, the torque and the shaft speed were recorded. Part of the power input was dissipated in the bearings of the rotating shaft. This loss was determined by measuring the torque required to keep a bladeless shaft rotating in fluids of different viscosities. This allowed a correction to be made to the experimental results.

4.2 Influence of the temperature on the viscosity

Because of the viscous dissipation the temperature of the fluid in the SSHE increases and consequently the viscosity decreases. This effect is particularly important at high shaft speeds and with highly viscous fluids whose viscosities may change by a factor of two between entering and leaving the SSHE.

For most stirrers the power consumption in a laminar flow regime is proportional to the viscosity. We assumed that this law also applies to SSHEs. This means that the power consumed is proportional to a mean viscosity defined in the following way:

$$\eta = \frac{1}{L} \int_{o}^{L} \eta_L \, dz \quad , \tag{24}$$

in which η_L is the local viscosity. Provided the temperature range is not too great, the relationship between viscosity and temperature is approximately:

$$\eta_L = \eta_o \exp (-a'T) \tag{25}$$

If the above assumption is correct and if it is assumed that the specific heat and the density of the fluid are only slightly temperature dependent, then the temperature gradient, dT/dz, in the adiabatic votator will be proportional to the viscosity, i.e.:

$$\frac{dT}{dz} \sim \exp (-a'T) \tag{26}$$

With the boundary conditions $T = T_1$ for $z = 0$ and $T = T_2$ for $z = L$, it then follows from Eq. (26) that:

$$\exp (a'T) = \frac{z}{L} \exp \left[(a'T_2) - \exp (a'T_1) \right] + \exp (a'T_1) \tag{27}$$

From Eqs. (24), (25) and (27) it is found that:

$$\eta = \frac{a' \eta_o (T_2 - T_1)}{\exp (a'T_2) - \exp (a'T_1)} \tag{28}$$

This equation can be approximated by assuming that η is equal to the viscosity at the arithmetic mean of T_1 and T_2. For a 97% glycerol/water mixture at $T_1 = 15^{o}C$ and $T_2 = 25^{o}C$ the viscosity is given by $\eta = 4.6 \exp (-0.087\ T)$ N.s.m^{-2}. Application of Eq. (28) yields $\eta = 0.79$ N.s.m^{-2}. The approximate method gives $\eta = 0.77$ N.s.m^{-2}. In this case the error introduced by the simplified method is thus less than 3%. In nearly all our measurements the increase in temperature was less than in the above example, thus further reducing the error. This method can also be applied if the SSHE is used as a cooler.

As will be demonstrated later, the power, and consequently dT/dz, is proportional to $\eta^{0.7}$. It can be shown that the result of the above calculation is not invalidated by this fact.

The accuracy of the torque meter, with measuring ranges of 0-0.3 kg.m^{2}.s^{-2}

0-1 $kg.m^2.s^{-2}$ and 0-3 $kg.m^2.s^{-2}$, was 2% of the full scale, i.e. 0.06 $kg.m^2.s^{-2}$. The error in the net torque (without bearings) is therefore 0.12 $kg.m^2.s^{-2}$. Measurements with a net torque of less than 0.3 $kg.m^2.s^{-2}$ were therefore disregarded.

4.3 Experimental results

To determine the influence of the mass flow rate on the power consumption, experiments in which this parameter was varied were carried out. There appeared to be no relationship between power consumption and mass flow rate if viscosity effects were properly accounted for. In the other experiments the mass flow was kept constant at 0.33 $kg.s^{-1}$.

In a similar way, the influence of the pressure was investigated at pressures of 0, 10 and 30 bar gauge. The friction in the bearings increased considerably with the pressure, but the net power dissipated in the fluid was found to be independent of the pressure. All other experiments were carried out at atmospheric pressure.

The results of the experiments in which the shaft speed, the number of rows of scraper blades and the fluid viscosity were varied are tabulated in the Appendix (Chapter 7.3). The results of the experiments with the 56 x 10^{-3}m shaft with six rows of scraper blades are plotted in Fig. 22, from which it appears that there is no unique relationship between the power number and the Reynolds number.

4.4 Theoretical model for power consumption

The power consumption in a SSHE can be considered in two parts, viz. the dissipation in the annular space and the loss due to the scraping of the blades against the wall. In this chapter a model will be derived for both parts of the power consumption.

4.4.1 Power consumed by the scraping of the blades

If the edge of the blade is assumed to be rectangular, as in Fig. 23, isothermal flow is assumed and $s >> \delta$, the velocity profile between scraper blade and tube wall is linear. The rate of shear will be $\pi d_t N/\delta$, and the power consumed to overcome this friction can be derived as:

$$Po = \frac{\pi^2 s}{\delta} Re_R^{-1} n \tag{29}$$

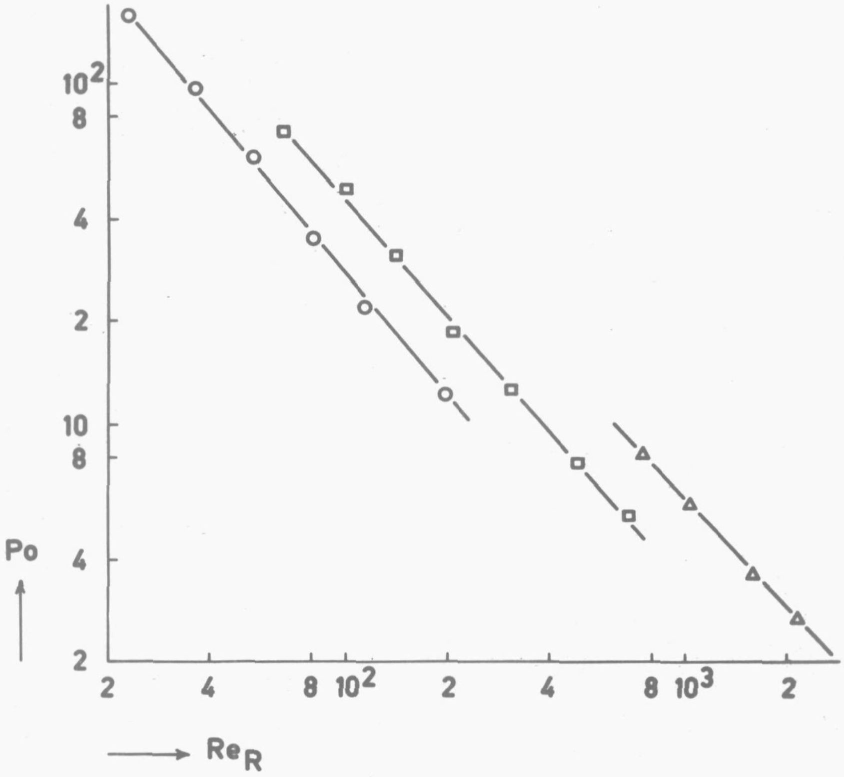

Fig. 22 Relationship between power number Po and Reynolds number Re_R for various viscosities (d_s = 56 x 10^{-3} m;n = 6).
Viscosity η (N.s.m^{-2}): O1.1, □0,4, Δ0.1.

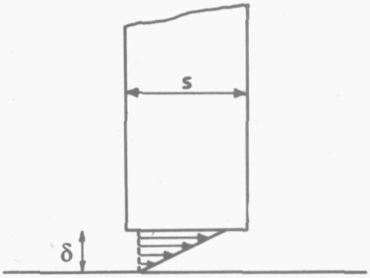

Fig. 23 Flow between scraper blade and tube wall.

Equation (29) suggests a unique relationship between power number and Reynolds number. However, Fig. 22 reveals that this specific relationship, valid for many types of stirrers, cannot be applied straightforwardly to predict the power consumption in the SSHE. As the essential difference between a SSHE and a stirred vessel lies in the presence or absence of scraping, the deviating behaviour of the SSHE is probably caused by the scraping. Two factors may cause this phenomenon, viz.:

- The viscous heating of the liquid between the edge of the scraper blade and the wall is considerable. This results in a temporary decrease of the viscosity of this liquid layer.
- The clearance between the edge of the scraper blade and the wall of the heat transfer tube may not be constant, but be dependent on the operating conditions.

The influence of both effects will be considered in the following sections.

4.4.1.1 *Viscous heating of the liquid between the edge of the scraper blade and the tube wall*

The heat dissipated in the liquid is partly transported into the scraper blade and partly into the wall of the heat transfer tube. The heat flow into the scraper blade is stationary, because the edge of the blade is constantly in contact with the layer of hot liquid near the cylinder wall. The heat flow towards the cylinder wall is different because the contact time of the wall with the hot liquid layer is very short. Therefore the problem of viscous heating at the edges of the scraper blades will be treated in two steps:

1. Analysis of the heat transfer mechanism between the liquid and the cylinder.
2. Analysis of the temperature distribution in the liquid.

For the analysis of the heat transfer mechanism between liquid and cylinder we have to calculate the temperature distribution in the liquid layer between blade edge and tube wall. This is possible if the conditions at the liquid/tube wall boundary are known. This problem can be analysed by assuming a heat transfer resistance of $1/\alpha^*$ in the tube wall.

α^* can be evaluated by calculating the temperature profile in the tube wall when a plane heat source is moving with constant velocity along the surface of a semi-infinite body. The calculation of α^* is given in the Appendix (Chapter 7.4). The result is:

$$\alpha^* = 2.36\sqrt{\frac{d_t N \rho_w c_w \lambda_w}{s}} \tag{30}$$

For the temperature profile in the liquid layer and in the blade the differential equations are derived as follows: in the liquid layer the viscous dissipation per unit time per unit volume is $\eta^* v_o^2/\delta^2$. Within the range $-\delta \leqslant z \leqslant 0$, the equation of energy is:

$$\lambda \frac{d^2T}{dz^2} + \eta^* \frac{v_o^2}{\delta^2} = 0 \tag{31}$$

Assume that the temperature of the blade is dependent only on the distance to the scraping edge (see Fig. 24). The thickness of the blade, m, is much greater than the width of the scraping edge, s. The blade is taken to be perpendicular to the tube wall. The temperature of the liquid near the sides of the blade is zero and there is a uniform heat transfer coefficient α_m from the blade to the liquid.

Consider part of the blade of unit length between z and z + Δz. The heat balance for this part of the blade reads:

$$-\lambda_s m \left.\frac{dT}{dz}\right|_z + \lambda_s \left.\frac{dT}{dz}\right|_{(z+\Delta z)} - 2\alpha_m \Delta z T = 0 \tag{32}$$

For $\Delta z \rightarrow 0$, this changes to:

$$\frac{d^2T}{dz^2} = 2\frac{\alpha_m}{\lambda_s m} T \tag{33}$$

Eqs. (31) and (33) must be solved with the boundary conditions:

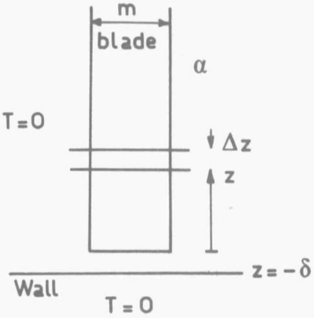

Fig. 24 Sketch of the scraper blade.

(1) $T = 0 \quad \text{at } z = \infty$

(2) $\lambda \frac{dT}{dz} = \alpha^* T \quad \text{at } z = -\delta$

(3) $T \Big|_{z < o} = T \Big|_{z > o} \quad \text{at } z = o$

(4) $-s\lambda \frac{dT}{dz} \Big|_{z < o} = -m\lambda_s \frac{dT}{dz} \Big|_{z > o} \quad \text{at } z = o$

The solutions are:

$$T = K_1 \exp\left(-\sqrt{\frac{2\alpha_m}{m\lambda_s}}\, z\right) + K_2 \exp\left(\sqrt{\frac{2\alpha_m}{m\lambda_s}}\, z\right) \text{ for } z \geqslant o$$

$$T = -\frac{\eta^* v_o^2}{2\lambda\delta^2} z^2 + K_3 z + K_4 \text{ for } -\delta \leqslant z \leqslant 0$$

Introduction of the boundary conditions yields for the temperature in the liquid layer ($-\delta \leqslant z \leqslant 0$):

$$T = -\frac{\eta^* v_o^2}{2\lambda\delta^2} z^2 + K_3 z + K_1 , \tag{34}$$

with:

$$K_3 = -\frac{\eta^* v_o^2}{\delta}\left(\frac{1}{\alpha^*} + \frac{\delta}{2\lambda}\right)\left(\frac{\lambda}{\alpha^*} + \delta + \frac{s\lambda}{\sqrt{2\alpha_m m\lambda_s}}\right)^{-1}$$

and:

$$K_1 = \frac{-s\lambda}{\sqrt{2\alpha_m m\lambda_s}} K_3$$

The average increase in temperature in the liquid is:

$$\Delta T = \frac{1}{\delta}\int_{-\delta}^{o} T dz = -\frac{\eta^* v_o^2}{6\lambda} - \tfrac{1}{2}\delta K_3 + K_1$$

or:

$$\Delta T = \frac{\eta^* v_o^2}{\lambda}\left\{\frac{1}{3\alpha^*} + \frac{\delta}{12\lambda} + \frac{s}{\sqrt{2\alpha_m m\lambda_s}}\left(\frac{1}{3} + \frac{\lambda}{\alpha^* d}\right)\right\}\left(\frac{1}{\alpha^*} + \frac{\delta}{\lambda} + \frac{s}{\sqrt{2\alpha_m m\lambda_s}}\right)^{-1} \quad (35$$

Analysis of Eq. (35) reveals the importance of the various terms:

For:

$$\lambda_w = 15\ \text{W.m}^{-1}.{}^{o}\text{C}^{-1}$$
$$v_o = 3\ \text{m.s}^{-1}$$
$$d_t = 0.05\ \text{m}$$
$$\rho_w = 8000\ \text{kg.m}^{-3}$$
$$c_w = 420\ \text{J.kg}^{-1}.{}^{o}\text{C-1}$$
$$s = 10^{-4}\ \text{m}$$

it follows:

$$\alpha^* = 1.6 \times 10^{6}\ \text{W.m}^{-2}.{}^{o}\text{C}^{-1}$$

Further estimates are:

$$\delta = 2 \times 10^{-6}\ \text{m}$$
$$\lambda = 0.23\ \text{W.m}^{-1}.{}^{o}\text{C}^{-1}$$
$$\alpha_m = 116\ \text{W.m}^{-2}.{}^{o}\text{C}^{-1}$$
$$m = 1.5 \times 10^{-3}\ \text{m}$$
$$\lambda_s = 17\ \text{W.m}^{-1}.{}^{o}\text{C}^{-1}$$

and hence:

$$\frac{1}{3\,\alpha^*} = 2.10^{-7}$$
$$\frac{\delta}{12\lambda} = 7.2 \times 10^{-7}$$
$$\frac{\lambda}{\alpha^*\delta} = 0.075$$
$$\frac{s}{\sqrt{2\,\alpha_m m \lambda_s}} = 0.4 \times 10^{-4}$$

Therefore (35) simplifies to:

$$\Delta T = \frac{\eta^* v_o^{\,2}}{\lambda}\left(\frac{1}{3} + \frac{\lambda}{\alpha^*\delta}\right) \qquad (36)$$

From (30) and (36) it follows:

$$\Delta T = \frac{\pi^2 \eta^* N^2\, d_t^{\,2}}{\lambda}\left[\frac{1}{3} + \frac{\lambda}{2.36\,\delta}\sqrt{\frac{s}{d_t N \rho_w c_w \lambda_w}}\right] \qquad (37)$$

and with:

$$\eta = \eta_o\, e^{-a' T}$$

$$\frac{\eta^*}{\eta} = \exp\left[\frac{-\,\pi^2 a'\,\eta^* N^2\, d_t}{\lambda}\left\{\frac{1}{3} + \frac{\lambda}{2.36\,\delta}\sqrt{\frac{s}{d_t N \rho_w c_w \lambda_w}}\right\}\right] \qquad (38)$$

Thus far it has been assumed that the conditions in the liquid between the edge of the blade and the tube wall are stationary. However, this liquid is continuously refreshed. It may be asked whether the steady state temperature and viscosity are reached within a relatively short time, which would justify the foregoing analysis. For a simplified case, in which the blade and the wall are heat absorbers with temperature $T = 0$, this is demonstrated to be true in the Appendix (Chapter 7.5).

4.4.1.2 Variable clearance between the edge of the scraper blade and the tube wall

Penney and Bell[26] suggest that the clearance between the edge of the scraper blade and the tube wall is not constant, but is dependent on the operating conditions of the SSHE. The centrifugal force and the viscous force, which tend to press the blade against the wall, are in equilibrium with the hydrodynamic lift force caused by the slipper bearing effect.

The centrifugal force is proportional to $m' N^2 d_t$ and the viscous force to ηNdt. The hydrodynamic lift force[35] is proportional to

$$\frac{\eta^* N s^2 d_t}{\delta 2}$$

In equilibrium conditions,

$$\frac{\eta^* N s^2 d_t}{\delta 2} = \beta \eta N d_t + \gamma N^2 m' d_t \qquad (39)$$

is valid, in which β and γ are constants.

Eq. (39) can be rewritten in the form:

$$\delta = \frac{s \sqrt{\eta^*}}{\sqrt{\gamma N m' + \beta \eta}} \qquad (40)$$

4.4.1.3 Combination of effects of viscous heating and variable clearance

In Chapter 4.4.1.1 the decrease in viscosity of the liquid between the edge of the blade and the tube wall has been expressed as a function of various parameters (Eq. (38)),. in which δ is still unknown. In Chapter 4.4.1.2, the value of δ has been calculated as a function of the operating conditions and the reduced viscosity. These equations will now be used to introduce $\frac{\eta^*}{\eta}$ into Eq. (29).

Eq. (38) and (40) can be combined to give:

$$\frac{\eta^*}{\eta} = \exp\left[\frac{-\pi^2\ a'\ \eta^* N^2\ d_t{}^2}{\lambda}\left\{\frac{1}{3} + \frac{\lambda}{2.36}\ \frac{\sqrt{\gamma\ Nm' + \beta\eta}}{\sqrt{s\ \eta^* d_t\ N\rho_w c_w \lambda_w}}\right\}\right] \tag{41}$$

This is a transcendental equation that cannot be solved analytically. For $0.1 < \zeta < 2$, the function $\frac{1}{3} + \zeta$ can be approximated by $1.25\sqrt{a}$, as is shown in Fig. 25. If this approximation is substituted in Eq. (41) and the logarithm is taken, the result is:

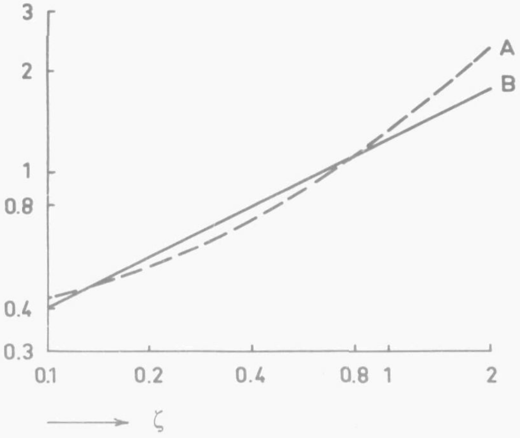

Fig. 25 $1.25\sqrt{\zeta}$ (curve B) as an approximation of $\zeta + 1/3$ (curve A) for $0.1 < \zeta < 2$.

$$\ln\left(\frac{\eta^*}{\eta}\right) = -\left(\frac{\eta^*}{\eta}\right)^{\frac{3}{4}} \left\{\frac{0.81\ \pi^2 a'(Nd_t)^{1.75}\left(\gamma\ \frac{Nm'}{\eta} + \beta\right)^{0.25}}{\lambda^{0.5}\left(s\rho_w\ c_w\ \lambda_w\right)^{0.25}}\right\} \tag{42}$$

or: $$\ln\left(\frac{\eta^*}{\eta}\right) = -\left(\frac{\eta^*}{\eta}\right)^{\frac{3}{4}} \xi \tag{43}$$

We assume that the solution of Eq. (43) can be approximated by the equation:

$$\frac{\eta^*}{\eta} = \frac{1}{K\xi + 1} \qquad \left(0.4 < \frac{\eta^*}{\eta} < 1\right) \tag{44}$$

This can be written in the form:

$$\xi = \frac{1}{K}\left(\frac{1}{\eta^*/\eta} - 1\right) \qquad (45)$$

In Fig. 26, ξ is plotted vs. $\frac{1}{\eta^*/\eta} - 1$ in the range $0.4 < \frac{\eta^*}{\eta} < 1$ both with Eq. (43) and (45).

From this plot it follows: K = 0.90. Eq. (42) then gives:

$$\frac{\eta^*}{\eta} = \frac{1}{1 + \eta N^{1.75}\left(\gamma \frac{Nm'}{\eta} + \beta\right)^{0.25} \frac{7.2\ a'\ d_t^{1.75}}{\lambda^{0.5}\left(s\rho_w c_w \lambda_w\right)^{0.25}}} \qquad (46)$$

Eq. (29) for the power consumption can now be used if Eq. (40) is substituted for δ and Eq. (46) for the viscosity in the Reynolds number:

$$Po = \frac{\pi^2 s}{\delta} \frac{\eta^*}{\eta} Re_R^{-1}\ n$$

$$Po = \pi^2 \sqrt{\gamma \frac{Nm'}{\eta} + \beta}\ \sqrt{\frac{\eta^*}{\eta}}\ Re_R^{-1}\ n$$

or:

$$Po = n\pi^2\ Re_R^{-1} \sqrt{\frac{\gamma \frac{Nm'}{\eta} + \beta}{1 + \eta N^{1.75}\left(\gamma \frac{Nm'}{\eta} + \beta\right)^{0.25} y}} \qquad (47)$$

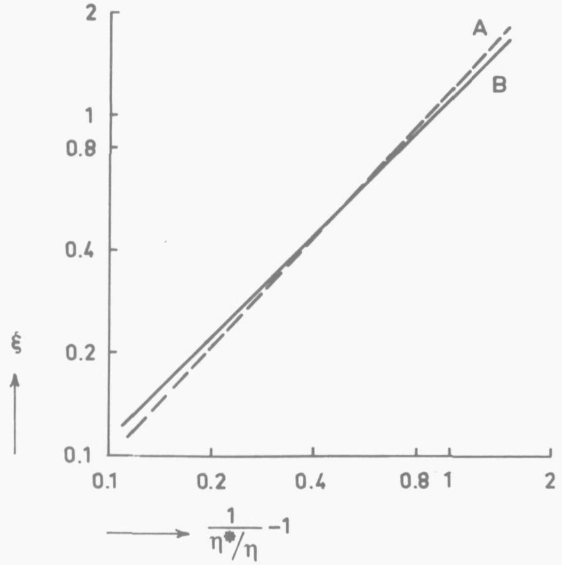

Fig. 26 Approximation of Eq. (43) (curve A) by Eq. (45) (curve B).

with: $$y = \frac{7.2\ a'\ d_t^{1.75}}{\lambda^{0.5}\left(s\rho_w c_w \lambda_w\right)^{0.25}} \tag{48}$$

4.4.2 Power consumed in the annular space

For the calculation of the power consumed in the annular space two flow regimes will be considered, viz., laminar Couette flow and the Taylor instability regime. For the Couette flow regime we first consider the case where there is no clearance between scraper blade and shaft.

If the annular space, $\frac{1}{2}(d_t-d_s)$, is small relative to the diameter, the flow is similar to that between two flat plates (see Chapter 3), one of which is moving at a speed $\pi d_t N$ with respect to the other. The velocity profile is in this case given by ~~Eq. 36~~ 36):

$$v_z = \frac{2\pi x\ d_t N}{d_t-d_s} - \frac{(d_t-d_s)\ \ x}{4\eta}\ \frac{dp}{dz}\left(1-\frac{2x}{d_t-d_s}\right) \tag{49}$$

Since the scraper blade completely fills the space between shaft and tube wall:

$$\int_0^{\frac{1}{2}(d_t-d_s)} v_x dx = 0 \tag{50}$$

The combination of these equations then gives:

$$v_z = \frac{12\pi d_t\ Nx^2}{(d_t-d_s)^2} - \frac{4\pi d_t\ Nx}{d_t-d_s} \tag{51}$$

From the velocity distribution given in Eq. (51), the shear rate at the wall can be calculated. After multiplication by the tube surface area, half the diameter and the angular velocity, the power and therefore the power number is found:

$$\frac{P}{\rho N^3 d_t^4 L} = \frac{8\pi^3 d_t}{d_t-d_s}\left(\frac{\eta}{N d_t^2 \rho}\right)$$

or:

$$Po = \frac{8\pi^3 d_t}{d_t - d_s} Re_R^{-1} \qquad (52)$$

When there are no blades, $\frac{dp}{dz}$ is zero in equation (49). After some calculations it is then found:

$$Po = \frac{2\pi^3 d_t}{d_t - d_s} Re_R^{-1} \qquad (53)$$

From Eqs. (52) and (53) it appears that the power number is inversely proportional to the Reynolds number:

$$Po = R \, Re_R^{-1} \qquad (54)$$

Around the blades the flow pattern is different from that described in (49), but this region is small compared with that of the undisturbed part of the annulus, and therefore (54) will still hold. The value of R can be calculated from the velocity profile, given in Chapter 3 for the shaft with a diameter of 56 x 10^{-3} m. This will be discussed in Chapter 4.4.4.

For the Taylor instability regime it has been shown[30] that for Reynolds numbers that are not appreciably higher than the upper limit of the Couette flow regime the power consumption may be represented by:

$$Po = \text{constant } Re_R^{-0.5} \qquad (55)$$

At the critical Reynolds number, discussed in Chapter 3, Eqs. (54) and (55) should yield the same value. This results in:

$$\left.\begin{aligned} Po &= R \, Re_R^{-1} && \text{for } Re_R < Re_{cr} \\ Po &= R \, Re_{cr}^{-0.5} Re_R^{-0.5} && \text{for } Re_R > Re_{cr} \end{aligned}\right\} \qquad (56)$$

4.4.3 Evaluation of the parameters in the model from the experimental data

From Eqs. (47) and (56) it follows that the power consumption in a SSHE can be described by

$$Po = n\pi^2 Re_R^{-1} \sqrt{\frac{\gamma \frac{Nm'}{\eta} + \beta}{1 + \eta N^{1.75} \left(\gamma \frac{Nm'}{\eta} + \beta \right)^{0.25} \quad y}} + f\,(Re_R) \qquad (57)$$

with: $$y = \frac{7.2\,a'd_t^{1.75}}{\lambda^{0.5} \quad (s\rho_w c_w \lambda_w)^{0.25}} \tag{48}$$

and: $$\left.\begin{aligned} f(Re_R) &= R\,Re_R^{-1} \quad \text{for } Re_R < Re_{cr} \\ f(Re_R) &= R\,Re_{cr}^{-0.5}\,Re_R^{-0.5} \quad \text{for } Re_R > Re_{cr} \end{aligned}\right\} \tag{58}$$

There are four unknown parameters in the equations, viz., ν, β, y and R, that can be determined from the experimental data. As (57) cannot be linearized it is not possible to apply regression analysis to find the parameters. The calculation of the parameters from the experimental data (see Chapter 7.3) was performed as follows:

It was first estimated what values could be expected for the parameters. The ranges of the parameters were then divided in a number of equal-sized steps. At all possible combinations of ν, β, y and R that were thus obtained, the sum of the squares of the difference between measured and calculated power number, divided by the experimental power number was determined. If one or more of the values of the parameters that corresponded to the lowest sum was on the boundary of a range, the procedure was repeated with new estimates of the parameters. If the values of the parameters with the lowest sum were within the ranges, the step size was reduced until sufficient accuracy for the values of ν, β, y and R was obtained. The calculations were performed$^+$ with a digital computer.

The results of the calculations are given in Table 8.

From the derivation of the model for power consumption, it follows that ν and y are not dependent on the shaft diameter and the number of scraper blades. y is a constant that is determined by physical properties of tube wall and working fluid, the geometry of the blade edge and the tube diameter. ν is determined by the ratio between the hydrodynamic lift force and the centrifugal force.

The values of ν and y in Table 8 vary considerably. This is due to the fact that different combinations of the four parameters may result in almost the same values for S^2. This is also the reason why values of R = 0 were obtained in a number of series of experiments.

+By Mr P.R.Croes

Table 8

Evaluation of γ, β, y and R in Eq. (57).

Shaft diameter (10^{-3}m)	Number of rows of scraper blades	γ	β	$y \times 10^3$	R	S^2	S (%)
46	2	588	2920	0.40	0	130	11
46	4	540	3100	1.00	0	167	13
46	6	512	3640	2.00	0	168	13
56	2	788	3740	0.70	0	127	11
56	4	580	4775	1.12	30	61	8
56	6	248	4184	3.28	814	42	6
62	2	600	6200	0.50	0	47	7
62	4	376	5700	1.20	0	98	10
62	6	332	5300	1.40	0	48	7
68	2	2602	8524	3.78	1195	3	2
68	4	294	5079	1.98	1546	1	1
68	6	248	4932	1.38	1146	2	1

The average value of y has been determined from the values in Table 8 (the lowest and highest values not being considered). This resulted in $y = 1.4 \times 10^{-3}$. The calculation was then repeated with this value of y (Table 9).

From the values of γ, reported in Table 9, the average was 380 (the highest value being omitted). Again calculations were carried out to evaluate the two yet undetermined parameters, β and R. y was kept constant at 1.4×10^{-3}, and γ at 380. The results are given in Table 10.

Table 9

Evaluation of γ, β and R in Eq. (57) with y fixed at 1.4 x 10^{-3}

Shaft diameter (10^{-3} m)	Number of rows of scraper blades	γ	β	R	S^2	S (%)
46	2	270	1888	371	193	14
46	4	438	2594	233	180	13
46	6	400	3240	0	181	13
56	2	564	2622	269	164	13
56	4	494	4317	233	62	8
56	6	400	5200	0	51	7
62	2	468	4474	385	68	8
62	4	386	5924	36	102	10
62	6	300	5300	0	50	7
68	2	1624	11477	762	10	3
68	4	269	6133	1229	1	1
68	6	244	4930	1158	2	1

Table 10

Evaluation of β and R in Eq. (57) with y fixed at 1.4 x 10^{-3} and γ at 380

Shaft diameter (10^{-3} m)	Number of rows of scraper blades	β	R	S^2	S (%)
46	2	1937	343	196	14
46	4	2681	251	182	13
46	6	3240	0	183	14
56	2	1987	371	184	14
56	4	3835	365	67	8
56	6	5200	0	53	7
62	2	3684	463	72	8
62	4	5684	58	103	10
62	6	5300	0	52	7
68	2	9429	1035	35	6
68	4	6414	1135	2	1
68	6	5243	990	3	2

From the series of measurements that gave the best fit to the equation (shaft diameter 68 x 10^{-3} m) it appears that R does not depend on the number of rows of scraper blades. Therefore for each shaft diameter the average value of R was taken, omitting the extremely low values. The results of the calculations with only one parameter, , undetermined are given in Table 11.

Table 11

Evaluation of β in Eq. (57) with y fixed at 1.4 x 10^{-3}, γ at 380 and average values for R

Shaft diameter (10^{-3} m)	Number of rows of scraper blades	β	R	S^2	S (%)
46	2	2358	300	196	14
46	4	2439	300	183	14
46	6	2276	300	228	15
56	2	1982	370	184	14
56	4	3800	370	67	8
56	6	3700	370	73	9
62	2	3735	460	71	8
62	4	3374	460	173	13
62	6	3425	460	107	10
68	6	9198	1050	35	6
68	4	6939	1050	2	1
68	6	5070	1050	3	2

Although there is only one degree of freedom for the calculation, reported in Table 11, against four for those in Table 8, the average value of S, which is a measure of the fit of the experimental data to the model, increases only from 7.5% to 9.5%.

4.4.4 Discussion of the parameter values

Eq. (48) gives the relation between y and various physical properties and geometrical quantities. The only unknown factor is s, the thickness of the edges of the scraper blades. If one calculates s from (57) with y = 1.4 x 10^{-3} the result is: s = 0.028 x 10^{-3} m. This is a reasonable value, although it can only be taken as a rough estimate, because s is very sensitive to small changes in y. For $y = 1.0 \times 10^{-3}$ Eq. (48) yields $s = 100 \times 10^{-6}$ m and for $y = 2.0 \times 10^{-4}$, $s = 6.8 \times 10^{-6}$ m. Hence a twofold increase in y results in a value of s that is 16 times smaller.

In Chapter 4.4.2, R was derived and found to be dependent on the ratio of tube diameter and annular space, $d_t/(d_t-d_s)$. For the two extreme conditions, viz., no blades at all and completely closed blades, R is $2\pi^3 d_t/(d_t-d_s)$ and $8\pi^3 d_t/(d_t-d_s)$. In Table 12 the values of $R(d_t-d_s)/d_t$ are given for the four shaft diameters.

Table 12

The parameter R as a function of the four shaft diameters.

Shaft	R	$R.\frac{d_t-d_s}{d_t}$
No blades (theoretical)	$\frac{2\pi^3 d_t}{d_t-d_s}$	62
(Closed blades (theoretical)	$\frac{8\pi^3 d_t}{d_t-d_s}$	248
$d_s = 46 \times 10^{-3}$ m	300	118
$d_s = 56 \times 10^{-3}$ m	370	97
$d_s = 62 \times 10^{-3}$ m	460	85
$d_s = 68 \times 10^{-3}$ m	1050	110

There is no systematic dependency of $R(d_t-d_s)/d_t$ on the shaft diameter; the average is 102.

We can compare these results with the velocity profile for the shaft with a diameter of 56×10^{-3} m, determined in 3.1.4. From the velocity profile the shear rate at the tube wall can be calculated and from this the power consumption in the annular space, by the method described in 4.4.2. The result for this case is: $R(d_t-d_s)/d_t = 101$. The agreement between the measurements of the power consumption and the velocity profile is almost too perfect.

The values of ν and β are related to the equilibrium between centrifugal force, viscous force and hydrodynamic lift force. For a shaft speed of 10 rev. s^{-1} the centrifugal force per meter blade length is 35 N ($m' = 0.117$ $kg.m^{-1}$).

For the 56 x 10^{-3} m shaft and a liquid viscosity of 0.1 N.s.m^{-2} this means that the viscous force per meter blade length is $35\beta\eta\, Nd_t/\gamma\, N^2\, m' d_t$ = 15.5 N. The hydrodynamic lift force is therefore 50 N.

From Eq. (46) the decrease in viscosity due to viscous heating can be calculated for this case. The result is $\eta^* = 0.094$ N.s.m.$^{-2}$ and with $\eta = \eta_o e^{-a'T}$ it follows that the increase of the temperature of the liquid at the edge of the blade is: $\Delta T = 0.8^oC$. From Eq. (40) the clearance between the edge of the scraper blade and the tube wall can be calculated roughly as 0.5 x 10^{-6} m. This is only an approximation as the value of s could not be determined accurately. However, we may conclude that the clearance between the edge of the scraper blade and the tube wall is of the order of 1 x 10^{-6} m.

It is important to realize that the foregoing analysis was derived for an adiabatic votator. But the apparatus is, of course, never used that way, If heat transfer takes place, the temperature in the bulk of the liquid is different from that near the heat transfer tube. This phenomenon can be accounted for by substituting the viscosity of the liquid at the wall temperature in the part of the power consumption due to scraping.

4.5 Empirical correlation for power consumption

From Eqs. (57), (58) and (48) and the values of the parameters given in Table 11, the power consumption can be predicted if the operating conditions are known. To derive an equation of a simpler form, it was assumed that the power consumption could be written in the form:

$$P = \frac{u_o\, (Nd_t)^{u_1}\, \eta^{u_2}\, n^{u_3}\, L}{(d_t - d_s)^{u_4}} \qquad (59)$$

The logarithm of (59) was taken and multiple linear regression analysis was applied to the data of the Appendix (Chapter 7.3) in order to find u_o...... ....u_4. The result was:

$$P = 251\, \frac{(Nd_t)^{1.79}\, \eta^{0.66}\, n^{0.68}\, L}{(d_t - d_s)^{0.31}} \text{ (in m.k.s. units)} \qquad (60)$$

The multiple correlation coefficient was 0.992. An attempt was also made to see whether power consumption measurements for another SSHE (L = 0.26m, d_t = 0.05 m) reported previously[37] could be correlated in the same way. The values of u_3 and u_4 were taken from (60) and u_o, u_1 and u_2 were determined, resulting in:

$$P = 276 \frac{(Nd_t)^{1.52} \eta^{0.68} n^{0.68} L}{(d_t - d_s)^{0.31}} \text{ (in m.k.s. units)} \qquad (61)$$

Eq. (61) is only slightly different from Eq. (60).

When the data of Skelland and Leung on power consumption, discussed in Chapter 2.1, are compared with Eq. (61), good agreement between these experiments and the equation is found.

Measurements of power consumption were carried out during heat transfer experiments (see Chapter 5). The measured power consumption was about 20% lower than the values calculated when the viscosity at the wall temperature was used in Eq. (60).

CHAPTER 5

HEAT TRANSFER

From the results of our experiments on heat transfer in a SSHE, which are described in this chapter, a proposed mechanism for this heat transfer has been developed.

5.1 Experimental procedure

The equipment used for the heat transfer measurements is described in Chapter 3.2.2. The amount of heat transported was calculated from the loss of sensible heat of the process liquid and the power dissipated in the liquid as a result of the rotation of the shaft. The latter part was measured in the same way as described in Chapter 4.

The overall heat transfer coefficient was calculated from the amount of heat transported, the area of scraped surface and the logarithmic mean temperature difference between the cooling water and the liquid in the annular space. The heat transfer coefficient between cooling water and heat transfer tube was calculated as previously done by other authors[7,15,18]:

$$\mathrm{Nu} = 0.0225\ \mathrm{Re}^{0.8}\ \mathrm{Pr}^{0.4},$$

in which the characteristic length in Nu and Re is the hydraulic diameter. The heat transfer coefficient between process liquid and scraped wall could then be calculated.

During these experiments tap water at a flow rate of $0.4 \times 10^{-3}\ \mathrm{m}^3.\mathrm{s}^{-1}$ was used. The temperature of the water at the inlet and outlet of the SSHE was measured by mercury thermometers in pockets. The water flow was measured roughly with a rotameter and more precisely with a volumetric flow meter.

Five variables were investigated: shaft speed, shaft diameter, number of rows of scraper blades, mass flow rate and viscosity. The experiments were carried out with glycerol/water mixtures of three different concentrations. For all measurements the correction factor φ, that is defined in Chapter 2.2 was calculated.

5.2 Influence of axial dispersion

In Chapters 2 and 3 it is argued that the assumption of plug flow in the SSHE may lead to too high values for the driving force for heat transfer. Axial dispersion decreases the effective temperature difference between working fluid and heat transfer medium. For the plug flow with axial dispersion model the decrease in heat transfer rate is dependent on two dimensionless parameters, $N_T = \alpha_s A/\phi_m c_p$, and $Pe_D = vL/D_E$ (see Fig. 2). The mass flow rate has a great influence on the decrease in heat transfer rate due to axial dispersion. A decrease in ϕ_m results in increasing N_T and decreasing Pe_D (v is proportional to ϕ_m); Fig. 2 shows that this gives a decrease in heat transfer rate.

Measurements of the heat transfer coefficient were carried out at shaft speeds of 4, 10 and 25 rev.s^{-1} using the 56 x 10^{-3} m shaft with two rows of scraper blades. The viscosity of the liquid varied between 0.1 and 0.2 N.s.m^{-2} (these figures refer to the viscosity of the liquid at the arithmetic mean of inlet and outlet temperature). The mass flow rate varied between 0.013 and 0.58 kg. s^{-1}. The results of the measurements are listed in Table A5 (Chapter 7.7) and plotted in Fig. 27.

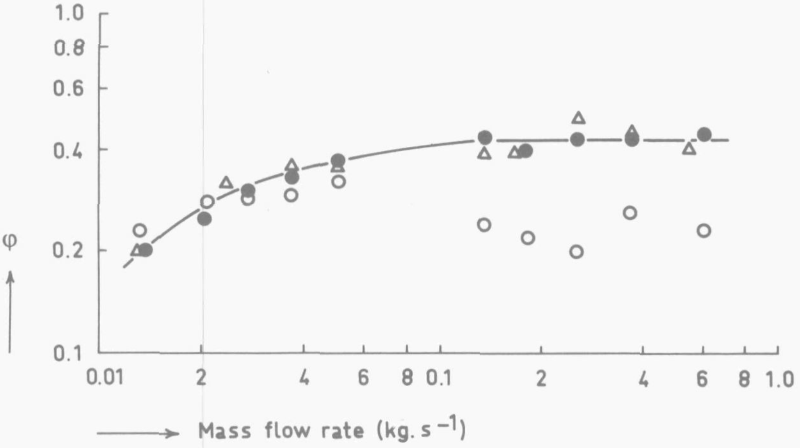

Fig. 27 Influence of the mass flow rate on the heat transfer coefficient at various shaft speeds.
N (rev.s^{-1}): ● 25, Δ 10, O 4.
η = 0.1-0.2 N.s.m^{-2}, d_s = 56 x 10^{-3} m, n = 2.

The influence of the mass flow rate at various viscosities was derived from measurements of the heat transfer coefficient, using the 56 x 10^{-3} m shaft with two rows of scraper blades. The shaft speed was constant at 10 rev.s^{-1}. Three glycerol/water concentrations were used. The viscosities were approximately 0.045, 0.15 and 0.45 N.s.m^{-2}. The results are listed in Table A6 (Chapter 7.7) and plotted in Fig. 28.

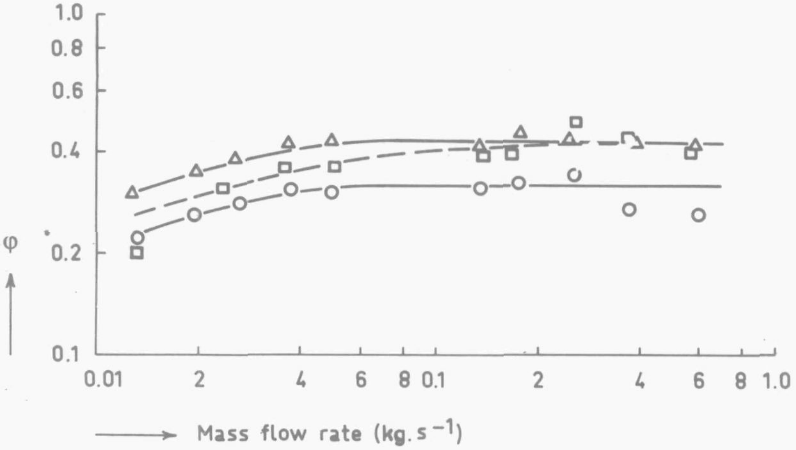

Fig. 28 Influence of the mass flow rate on the heat transfer coefficient at various viscosities.
η (N.s.m^{-2}): ○ca. 0.45, □ca. 0.15, △ca. 0.045.
N = 10 rev.s^{-1}, d_s = 56 x 10^{-3} m, n = 2.

In Figs. 27 and 28 the factor φ is plotted against the mass flow rate. For each series of measurements with constant N and η, φ is proportional to the effective heat transfer coefficient. At high mass flow rates ($\emptyset_m$>ca.0.1 kg.s^{-1}), the value of the effective heat transfer coefficient is independent of $\emptyset_m$ and this value is assumed to be the actual heat transfer coefficient α_s. The lower heat transfer coefficients for $\emptyset_m$ < ca. 0.1 kg. s^{-1} are caused by assuming plug flow in cases where axial dispersion is important.

Our results will now be compared to the model by Bott, Azoory and Porter[28], using Fig. 2. In Chapter 3 it has been calculated that the axial dispersion coefficient in the SSHE with the 56 x 10^{-3} m shaft rotating at 8 rev.s^{-1} with n = 2 is approximately 2.3 x 10^{-4} $m^2.s^{-1}$ for a liquid viscosity of 0.2 N.s.m^{-2}. This value for the dispersion coefficient was used in the calculation of the decrease in effective heat transfer coefficient according to Fig. 2. In Fig. 29 the measured and calculated ratio of the effective and actual heat transfer coefficient are plotted against the mass flow rate. The measurements shown in Fig. 28 for the viscosities of approximately 0.045 and 0.45 $N.s.m^{-2}$ were used for this purpose.

From Fig. 29 it can be seen that the theoretical model predicts the decrease in heat transfer due to backmixing fairly well.

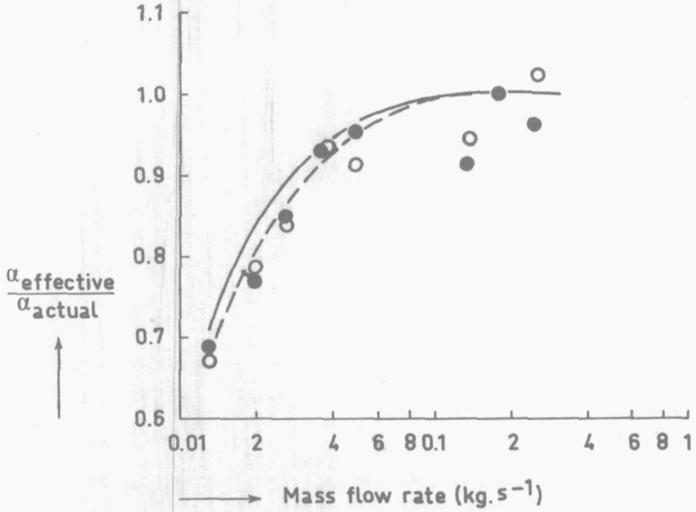

Fig. 29 Measured and theoretical ratio of the effective and actual heat transfer coefficients as a function of the mass flow rate.
$\eta = 0.45$ $N.s.m^{-2}$: ○ measured, full line theoretical,
$\eta = 0.045$ $N.s.m^{-2}$: ● measured, dashed line theoretical.

Industrial votators are usually operated at such high mass flow rates, and hence low values of N_T and high values of Pe_D, that the influence of the axial dispersion on heat transfer may be neglected. The measurements reported in the following sections were made at $\phi_m = 0.17$ $kg.s^{-1}$ and the influence of axial dispersion was therefore negligeable.

5.3 Results of experiments without influence of axial dispersion

Measurements of the heat transfer coefficient were carried out using the 56 x 10^{-3} m shaft with two rows of scraper blades. The shaft speed varied between 4 and 33.3 rev. s^{-1}. Three glycerol/water concentrations, having viscosities of approximately 0.04, 0.13 and 0.44 $N.s.m^{-2}$ were used.

The mass flow rate was about 0.17 kg.s^{-1}. The results of the measurements are listed in Table A7 (Chapter 7.7) and plotted in Fig. 30.

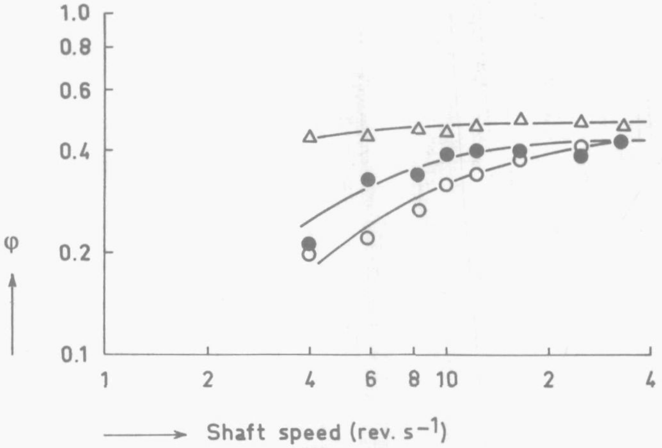

Fig. 30 Influence of the shaft speed on the heat transfer coefficient at various viscosities.
η (N.s.m^{-2}): ○ca. 0.45, ●ca. 0.15, △ ca. 0.040.
d_s = 56 x 10^{-3} m, n = 2, $\emptyset_m$ = 0.17 kg.s^{-1}.

The influence of the number of rows of blades on the heat transfer coefficient was investigated by carrying out experiments in which 2, 3, 4 or 6 rows of blades could be fitted to the 56 x 10^{-3} m shaft. The mass flow rate was about 0.17 kg. s^{-1} and the shaft speed 10 rev.s^{-1}. The viscosities of the glycerol/water mixtures were 0.04, 0.14 and 0.44 N.s.m.$^{-2}$. The results are listed in Table A8 (Chapter 7.7) and plotted in Fig. 31.

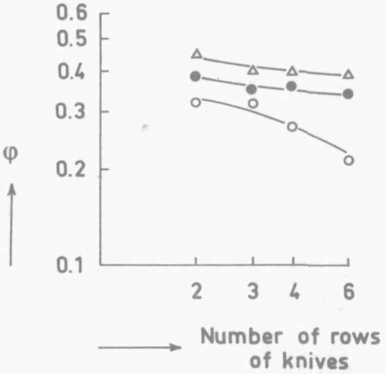

Fig. 31 Influence of the number of rows of knives on the heat transfer coefficient for various viscosities.
η (N.s.m^{-2}): ○ca. 0.44, ●ca. 0.14, △ca. 0.040.
d_s = 56 x 10^{-3} m, N = 10 rev.s^{-1}; $\emptyset_m$ = 0,17 kg.s^{-1}.

The last parameter studied was the width of the annular space. The shaft speed was 10 rev.s^{-1} during these experiments. Two rows of scraper blades were applied. The viscosities of the glycerol/water mixtures were again 0.040, 0.14 and 0.44 N.s.m^{-2}. The results are given in Table A9 (Chapter 7.7) and Fig. 32.

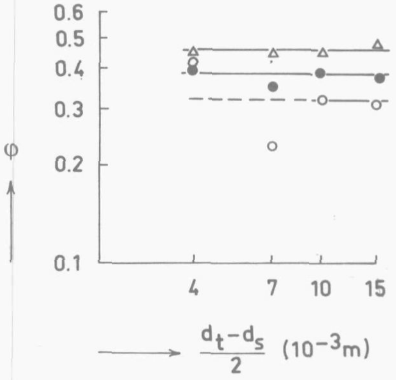

Fig. 32 Influence of the annular space on the heat transfer coefficient for various viscosities.
η (N.s.m^{-2}): ○ca. 0.44, ●ca. 0.14, △ca. 0.040.
N = 10 rev.s^{-1}, n = 2, $\emptyset_m$ = 0.17 kg.s^{-1}.

5.4 The mechanism of heat transfer

The literature survey in Chapter 2 shows that up to now it has been assumed that the mechanism of heat transfer in a SSHE consists of two steps:

1) In the time between two scrapings a thin layer of liquid close to the heat transfer surface is cooled by conduction. The temperature of the liquid as a function of time and position is given by penetration theory.
2) The thin and cooled layer is scraped off the wall and mixed with the bulk of the liquid in the annular space. The mixing is assumed to be imperfect and this qualitatively explains that the measured heat transfer coefficients are lower than is calculated from penetration theory[12].

From the study of the flow pattern, described in Chapter 3, it has appeared that the second step does not take place in the Couette flow regime. Neither is this mechanism valid for the Taylor vortices, as can be seen as follows: The depth of the penetration of heat in the time between two scrapings is ca. 1 x 10^{-4} m. The vortices in the Taylor instability regime will not cause a mixing of such a thin layer close to the wall with the liquid in the annular space.

It would seem, therefore that the mechanism for heat transfer described above is not valid. In the search for alternatives, two possible mechanisms were considered:

1) The contraction and subsequent expansion of the streamlines caused by the passage of the blade increase the heat flux to the heat transfer wall: The photographs of the flow pattern in Chapter 3 show that contraction and subsequent expansion of the streamlines takes place in the blade area. It is possible that this effect influences the penetration of heat in the liquid close to the heat transfer surface.
2) The penetration of heat in the time between two scrapings is followed by a temperature equalization: In the hydrodynamic boundary layer that builds up on the scraper blade the velocity of the liquid, relative to the blade velocity, is low. Therefore, after the liquid has been scraped off the wall, the time it remains in the boundary layer before contacting the wall again, is relatively long. In this boundary layer a temperature equalization may therefore take place, resulting in a high temperature gradient at the wall,and consequently in a high heat transfer coefficient.

In the following sections we will consider the merits of these possible mechanisms.

5.4.1 Influence of an oscillating wall on heat penetration

The contraction and subsequent expansion of the streamlines caused by the passage of the blade can be compared with the flow between two plane walls, one of which is oscillating. Let liquid fill the space $x > 0$ and be bounded by a stationary wall at $x = 0$ and an oscillating wall parallel to this stationary wall somewhere in the liquid. At $t = 0$ the temperature is zero for $x > 0$. For $t > 0$ the wall temperature is T_o.

If the oscillating wall is absent and heat transfer takes place by conduction only, the temperature in the liquid can be described with the penetration theory:

$$T = T_o \operatorname{erfc} \frac{x}{2\sqrt{at}} \tag{62}$$

The heat flux is in this case:

$$q = -\lambda \left.\frac{\partial T}{\partial x}\right|_{x = o} = \lambda \frac{T_o}{\sqrt{\pi at}} \tag{63}$$

In Chapter 7.6 it will be shown that the heat flux, as given by Eq. (63), is not influenced by a flow induced in the liquid by a plane oscillating in the x-direction.

One of the two possible mechanisms for heat transfer is now rejected. We may conclude, therefore, that high heat transfer coefficients in a SSHE, and hence high temperature gradients near the wall, are caused by a temperature equalization in the hydrodynamic boundary layer on the scraper blade.

5.4.2 Temperature equalization in a boundary layer

A second possible mechanism for heat transfer that will be considered is the penetration of heat followed by a temperature equalization in the boundary layer that builds up on the blade. A schematic view of the geometry is given in Fig. 33. The heat transfer surface is at $x = 0$. In the model the scraper blade is taken to be parallel to the heat transfer surface. The heat transfer tube moves and the blades are stationary.

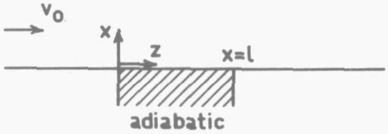

Fig. 33 Geometry of model for temperature equalization in a boundary layer.

In the boundary layer on the scraper blade the velocity of the liquid is relatively low compared to v_o. A temperature equalization may therefore occur in the boundary layer, resulting in a high temperature gradient at the wall after the blade passage. It may not be expected that the temperature equalization is complete, and therefore the equation resulting from penetration theory, which is discussed in Chapter 2, will yield too high values for the heat transfer coefficients. A correction factor φ will allow for this, as well as for other deficiencies of the model.

For $z < 0$ both wall ($x = 0$) and liquid ($x > 0$) have a velocity v_o in positive z-direction. The blade (between $z = 0$ and $z = l$) is supposed to be adiabatic. Hence for $z < 0$ is valid:

$$v_z = v_o \quad \text{for } x \geqslant 0$$
$$v_x = 0 \quad \text{for } x \geqslant 0$$

For $z > 0$:

$v_z = 0$ at $x = 0$

The wall temperature for $z < 0$ is T_o and the temperature of the liquid for $z < 0$ and $x = \infty$ is equal to zero. Let the temperature profile in the liquid at $z = 0$ be given by:

$$T = T_o \left(1 - \frac{x}{\delta_T}\right) \quad \text{for } x \leqslant \delta_T$$

and

$$T = 0 \quad \text{for } x > \delta_T$$

(The error function, which describes the temperature profile during heat penetration, is approximated by a linear function.)

Equations describing the velocity profile that builds up on the scraper blade are known from the literature[38]. As the thickness of the thermal boundary layer that builds up on the blade is usually smaller than that of the hydrodynamic boundary layer, the velocity profile is approximated by a linear function in x in the following way:

$$v_z = A(z)x \tag{64}$$

in which:

$$A(z) = \left.\frac{\partial v_z}{\partial x}\right|_{x = 0} \tag{65}$$

From the boundary layer equations[38] it follows:

$$A(z) = v_o \cdot \frac{3}{2} \cdot \frac{1}{4.64\sqrt{\frac{\nu z}{v_o}}}$$

and hence:

$$\frac{v_z}{v_o} = 0.324\ x\sqrt{\frac{v_o}{\nu z}} \tag{66}$$

A further assumption is:

$$v_x = 0 \tag{67}$$

Using the velocity profile given in Eqs. (66) and (67) the equation of energy must now be solved to find the temperature profile in the boundary layer.

The equation of energy reads for this case[38]:

$$v_z \frac{\partial T}{\partial z} = a\left(\frac{\partial^2 T}{\partial x^2} + \frac{\partial^2 T}{\partial z^2}\right) \tag{68}$$

(frictional heat is not taken into consideration).

The temperature gradients in the x-direction are much greater than in the z-direction and therefore $\partial^2T/\partial z^2$ is neglected with respect to $\partial^2T/\partial x^2$. After elimination of v_z with Eq. (66) the equation of energy now reads:

$$\epsilon \frac{x}{\sqrt{z}} \frac{\partial T}{\partial z} = \frac{\partial^2 T}{\partial x^2} \qquad (69)$$

with

$$\epsilon = \frac{0.324 \, v_o{}^{3/2}}{a\sqrt{\nu}}$$

The boundary conditions are:

$$\text{at } z = 0 \begin{cases} T = T_o \left(1 - \dfrac{x}{\delta_T}\right) & \text{for } x < \delta_T \\ T = 0 & \text{for } x > \delta_T \end{cases}$$

$$\text{at } x = 0: \frac{\partial T}{\partial x} = 0$$

(69) is solved by substituting:

$$\xi = z^{3/2}; \quad d\xi = \frac{3}{2} z^{1/2} \, dz$$

$$\zeta = x^{3/2}; \quad d\zeta = \frac{3}{2} x^{1/2} \, dx$$

(69) now reads:

$$\frac{\partial T}{\partial \xi} = \frac{3}{2\epsilon} \frac{\partial^2 T}{\partial \zeta^2} \qquad (70)$$

with boundary conditions:

$$\text{at } \xi = 0 \begin{cases} T = T_o \left(1 - \dfrac{\zeta^{2/3}}{\delta_T}\right) & \text{for } \zeta < \delta_T{}^{3/2} \\ T = 0 & \text{for } \zeta > \delta_T 3/2 \end{cases}$$

$$\text{at } \zeta = 0: \frac{\partial T}{\partial \zeta} = 0.$$

The solution to (70) is known[13]:

$$T = \frac{1}{2\sqrt{\pi \frac{3\xi}{2\epsilon}}} \int_0^{\delta_T{}^{3/2}} T_o \left(1 - \frac{z^2/3}{\delta_T}\right). \left\{ \exp - \frac{(\zeta - z)^2}{4.\frac{3\xi}{2\epsilon}} + \exp - \frac{(\zeta + z)^2}{4.\frac{3\xi}{2\epsilon}} \right\} dz \qquad (71)$$

This is a rather awkward expression. The problem can be simplified by linearizing $\left(1 - \frac{z^{2/3}}{\delta_T}\right)$. If this expression is plotted against $z.\delta_T{}^{-1.5}$ it is found that it may be approximated by $0.8 - 0.8\, z.\delta_T{}^{-1.5}$.

After substituting z and x for ξ and ζ, the solution is[13]:

$$
\begin{aligned}
\frac{T}{T_o} = {} & 0.4\,\delta_T^{-1.5}\left[\left(\delta_T^{-1.5} - x^{1.5}\right) \operatorname{erf}\left\{\left(\delta_T^{1.5} - x^{1.5}\right)\left(\frac{6z^{1.5}}{\epsilon}\right)^{-0.5}\right\} + \right. \\
& + \left(\delta_T^{1.5} + x^{1.5}\right) \operatorname{erf}\left\{\left(\delta_T^{1.5} + x^{1.5}\right)\left(\frac{6z^{1.5}}{\epsilon}\right)^{-0.5}\right\} + \qquad (72) \\
& \left. - 2x^{1.5} \operatorname{erf}\left\{x^{1.5}\left(\frac{6x^{1.5}}{\epsilon}\right)^{-0.5}\right\}\right] + 0.4\,\delta_T^{-1.5}\left(\frac{6z^{1.5}}{\pi\epsilon}\right)^{0.5} \\
& \cdot\left[\exp\left\{-\left(x^{1.5} + \delta_T^{1.5}\right)^2\left(\frac{6z^{1.5}}{\epsilon}\right)^{-1}\right\} + \exp\left\{-\left(x^{1.5} - \delta_T^{1.5}\right)^2\left(\frac{6x^{1.5}}{\epsilon}\right)^{-1}\right\} + \right. \\
& \left. - 2\exp\left\{-x^3\left(\frac{6z^{1.5}}{\epsilon}\right)^{-1}\right\}\right]
\end{aligned}
$$

The temperature profiles at $z = 1$ will now be calculated with (72) for the following conditions:

$v_o = 2.5\ \mathrm{m.s^{-1}}$

$l = 0.02\ \mathrm{m}$

$\delta_T = 1.37 \times 10^{-4}\ \mathrm{m}$

$a = 0.94 \times 10^{-7}\ \mathrm{m^2.s^{-1}}$

$$
\nu = \begin{cases} 0.8 \times 10^{-5}\ \mathrm{m^2.s^{-1}} & (\eta = 0.01\ \mathrm{N.s.m^{-2}}) \\ 0.8 \times 10^{-4}\ \mathrm{m^2.s^{-1}} & (\eta = 0.1\ \mathrm{N.s.m^{-2}}) \\ 0.8 \times 10^{-3}\ \mathrm{m^2.s^{-1}} & (\eta = 1\ \mathrm{N.s.m^{-2}}) \end{cases}
$$

The results are given in Fig. 34. They show that a good temperature equalization takes place in the boundary layer on the blade. At viscosities of 0.1 and 1 $\mathrm{N.s.m^{-2}}$ the temperature difference between bulk and liquid that reaches the wall after leaving the scraper blade is reduced to 19 and 11 percent.

In this boundary layer approximation the flow in the x-direction has been neglected. If this flow is taken into account the temperature equalization will be even better than calculated. On the other hand it has been assumed that the scraper blade is adiabatic. Often the scraper blade is made of stainless steel. Heat conduction will take place in the z-direction through the blade and this results in less temperature equalization. This effect may be more important for stainless steel blades than for plastic blades with low thermal conductivity.

The preceding calculations have shown that important aspects of the heat transfer mechanism are:

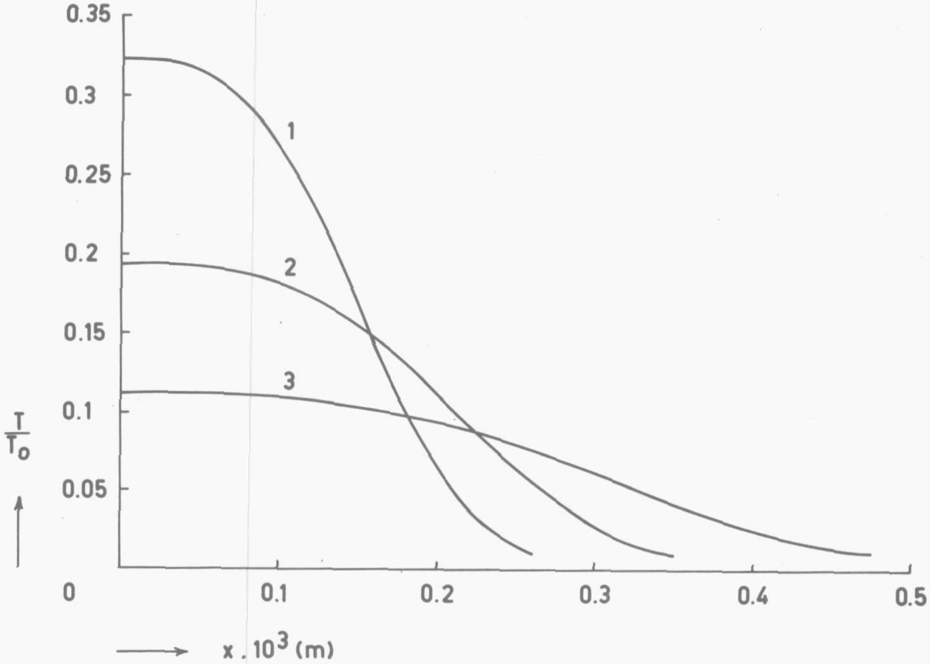

Fig. 34 Temperature equalization in a boundary layer.
η (N.s.m^{-2}): curve 1 0.01, curve 2 0.1, curve 3 1.

- Penetration of heat by conduction in a thin layer close to the heat transfer surface in the time between two scrapings;
- Partial temperature equalization in the boundary layer that builds up on the blade.

5.4.3 Penetration of heat after successive scrapings

The temperature equalization that takes place in the boundary layer on the blade is not complete, as can been seen in Fig. 34. Therefore the driving force during the penetration of heat after the first scraping is smaller than in the period before this scraping. This is shown in Fig. 35: The driving force, T_o-T_b, is smaller than T_o-0, that is assumed in the derivation of the heat transfer coefficient from penetration theory:

$$\alpha_s = \frac{2}{\sqrt{\pi}} \left(\lambda\rho \ c_p N \ n \right)^{0.5} \tag{73}$$

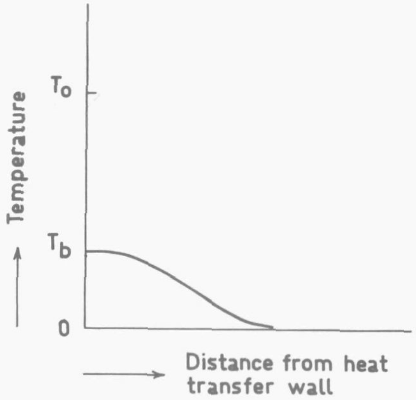

Fig. 35 Incomplete temperature equalization in the boundary layer on the scraper blade. The curve indicates the temperature of the liquid contacting the wall after the first blade passage.

In the period between the first and second scraping the average heat transfer coefficient will therefore be approximately:

$$\alpha_s = \frac{T_o - T_b}{T_o} \cdot \frac{2}{\sqrt{\pi}} \left(\lambda \rho \ c_p N \ n \right)^{0.5} \tag{74}$$

During the second scraping a temperature equalization in the boundary layer will again take place, but this time the temperature of the liquid on contacting the wall after the scraping will be higher than T_b in Fig. 35. This results in an even lower heat transfer coefficient in the period between the second and third scraping than that given by Eq. (74). As the mean residence time in a SSHE is some orders of magnitude higher than the time between two scrapings this process is repeated many times.

During the first periods of the process the depth of the penetration of heat is so small that the radial convective heat transport due to dispersion does not influence the process of heat penetration. However, after a few scrapings, followed by partial temperature equalizations in the boundary layer, the layer of liquid influenced by the penetration of heat becomes thicker and the radial dispersion begins to play a role, especially if Taylor vortices are present.

The radial dispersion can be represented by a stagnant film of thickness δ_D (influenced by the operating conditions), assuming good mixing in the liquid outside this film. This implies that the temperature of the liquid at $x = \delta_D$ is equal to the bulk liquid temperature during the penetration of heat. After a number of scrapings, followed by partial temperature equalizations, the penetration depth of the heat conduction will be equal to δ_D. A pseudo-equilibrium, which is schematically sketched in Fig. 36, will then be established.

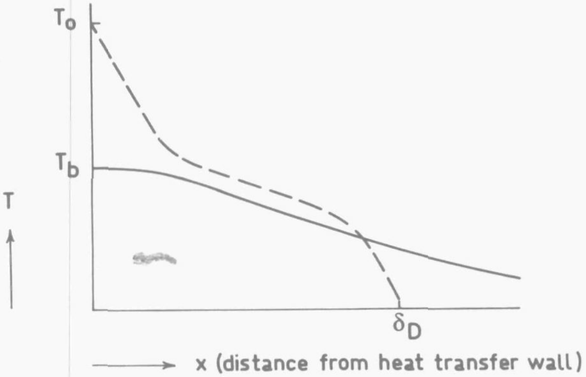

Fig. 36 Penetration and temperature equalization after various scrapings. Dashed line: temperature profile just before scraping. Full line: temperature profile of the liquid contacting the wall after the blade passage.

During the penetration of heat the temperature is T_o at $x = o$ and zero at $x = \delta_D$. During the temperature equalization in the boundary layer, the temperature at $x = 0$ drops from T_o to T_b. The temperature at $x = \delta_D$ increases, because the radial dispersion is smaller in the blade area. The heat transfer coefficient for this situation is again:

$$\alpha_s = \frac{T_o - T_b}{T_o} \quad \frac{2}{\sqrt{\pi}} \left(\lambda\rho \ c_p N \ n \right)^{0.5} \tag{74}$$

It is obvious that the value of $(T_o - T_b)/T_o$ is of paramount importance. If the influence of axial dispersion is absent, this factor is equal to the correction factor φ in Eq. (9).

There are three competing effects influencing the value of $(T_o - T_b)/T_o$ and hence of φ:

- The depth of the penetration of heat, δ_T, in the time between two scrapings. *For constant thermal diffusivity, δ_T is proportional to the square root of time.*
- The temperature equalization in the boundary layer on the scraper blade. In section 5.4.2 it has been shown that the equalization is more complete

when the shaft speed is low, the viscosity is high, and δ_T is low.

- The radial dispersion and hence δ_D. The greater the rotational Reynolds number, the smaller will be δ_D.

Equation (72) shows that increasing the shaft speed does not influence φ when radial dispersion is absent (where $\epsilon \sim v_o^{3/2} \sim \delta_T^3$, equation (72) proves that $(T|_{x=o})/T_o$ and hence φ is independent of shaft speed). If in the case of radial dispersion the value of δ_D is proportional to $N^{-\frac{1}{2}}$, φ is not influenced by the shaft speed either. In that case, the temperature profiles in Fig. 36 are similar when the shaft speed is varied.

5.5 Comparison of experimental results and the proposed mechanism

The influence of shaft speed and viscosity on the heat transfer coefficient, as shown in Fig. 30 will first be compared with the proposed mechanism. For a liquid having a viscosity of ca. 0.040 $N.s.m^{-2}$ the factor φ is not influenced by the shaft speed, but for liquids with higher viscosities φ increases with increasing shaft speed. In Fig. 37, φ is plotted as a function of Re_R.

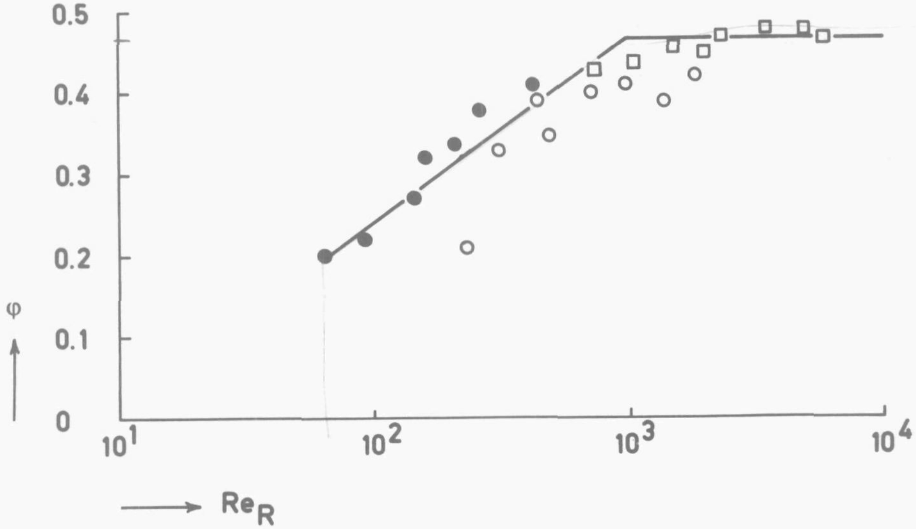

Fig. 37 φ as a function of the rotational Reynolds number.
η ($N.s.m^{-2}$): ○ca. 0.45, ●ca. 0.15, □ca. 0.040.
$d_s = 56 \times 10^{-3}$ m, n = 2.

For high values of Re_R, φ is constant. This area is in the Taylor vortices regime. Apparently in this flow regime δ_D is influenced by the shaft speed in the same way as δ_T. This means that δ_D is inversely proportional to the square root of the shaft speed. φ decreases for lower values of Re_R. For $Re_R \simeq 350$ this decrease is 20%, compared with the value of φ at high values of Re_R.

The Couette flow regime prevails for $Re_R < 280$. This means that in the Couette flow regime δ_D is more dependent on the shaft speed than in the Taylor instability regime. Experiments with other shaft diameters show the same trend. Above the critical Reynolds number φ approaches its final value, below the critical Reynolds number, φ decreases.

From Fig. 32 it appears that the width of the annular space has no influence on heat transfer if liquids with viscosities of 0.040 and 0.14 $N.s.m^{-2}$ are used. For a viscosity of 0.44 $N.s.m^{-2}$ the following explanation might be given for the higher heat transfer coefficient at an annular space of 4×10^{-3} m. Under these conditions the boundary layer that builds up on the scraper blade is thicker than the gap between the blade and the shaft. The velocity in this layer will be lower than in an undisturbed boundary layer, causing a better temperature equalization. The low heat transfer value at an annular space of 7×10^{-3} m is probably caused by a measuring error, or an incorrect mounting of the scraper blade.

From Fig. 31 it can be seen that φ decreases slightly with a decreasing number of rows of blades. This is caused by the fact that more rows of blades decrease the radial dispersion. The transition from Couette flow to Taylor vortices will take place at a higher Reynolds number, if many rows of blades are present[39]. Furthermore the contact time of the liquid and the wall between two scrapings is less than 1/Nn. The scraped liquid does not flow back from the scraper blade to the edge along the back of the blade, but contacts the wall again a short distance from the blade edge. This effect increases with an increasing number of rows of scraper blades.

We will now again consider the experiments by Skelland, Oliver and Tooke reported in Chapter 2. As the mass flow rate during their experiments was rather low, axial dispersion was important. The form of the correction factor for the experiments was:

$$\varphi = 1 - 2.78\ (Pe + 200)^{-0.18} \quad (400 < Pe < 6000)$$

Both the final value of φ, as reported in Chapter 5.4, and the influence of the axial dispersion (the mass flow rate is proportional to Pe) are included in this function. The experimental results of Skelland et al and those reported in this chapter are in agreement with each other.

Summarizing, it can be stated that at low mass flow rates the heat transfer rate is reduced by axial dispersion. In industrial heat exchangers the mass flow rate is high and the influence of axial dispersion is absent. The mechanism of heat transfer is as follows:

- Penetration of heat in the time between two scrapings (penetration depth δ_T).
- Partial temperature equalization in the boundary layer on the scraper blade.
- Radial dispersion outside the stagnant layer of thickness δ_D.

In the Taylor vortices regime the temperature profiles resulting from these effects are similar resulting in a constant value of φ.

CHAPTER 6

CONCLUSIONS AND DESIGN

6.1 Conclusions

Important physical aspects of scraped-surface heat exchangers have been studied, both experimentally and theoretically, viz. flow phenomena, power consumption and heat transfer. The interrelations between these phenomena have also been considered.

6.1.1 Flow phenomena

Dependent upon the operating conditions, the flow in a SSHE is in one of the following two regimes:

- Couette flow. This is simple shear flow in which the radial velocity component is zero outside the area close to the blade.
- Taylor vortices. Above a certain critical rotational Reynolds number large secondary toroidal vortices are formed in pairs with opposite rotation. The diameter of a vortex is approximately equal to the width of the annular space. Within the accuracy of the experiments the critical Reynolds number is equal to that for flow in the annulus between smooth rotating cylinders.

In the Couette flow regime the streamlines are concentric circles outside the blade area (for cutaway blades). The streamlines contract and expand near the blades. The resulting velocity profile is similar to that between two plates, one of which is moving parallel to the other, and with a pressure gradient in the direction of the flow.

The residence time of the liquid flowing through the SSHE is not uniform. This is partly caused by differences in velocity along, and in length of, streamlines and partly by dispersion mechanisms due to vortices and a pumping effect. The axial dispersion is so great that for heat transfer measurements at low mass flow rates the effective driving force for heat transfer is smaller than that calculated for the plug flow model.

6.1.2 Power consumption

For most stirrers the power number is a unique function of the rotational Reynolds number. This is not valid for SSHEs. For the same value of Re_R, Po increases with decreasing bulk viscosity. This is caused by two phenomena:

- Due to viscous dissipation the temperature of the liquid between the edge of the blade and the wall increases and therefore the viscosity decreases.
- The clearance between the edge of the scraper blade and the tube wall is dependent on the operating conditions.

A model incorporating these effects has been derived for the power consumption. The equation reads:

$$Po = n\,\pi^2\,Re_R^{-1}\sqrt{\frac{\nu\frac{Nm'}{\eta}+\beta}{1+\eta N^{1.75}\left(\nu\frac{Nm'}{\eta}+\beta\right)^{0.25}}}_{\,y} + f\,(Re_R)$$

where $f(Re_R) = R\,Re_R^{-1}$ for $Re_R < Re_{cr}$

and $f(Re_R) = R\,Re_{cr}^{-0.5}\,Re_R^{-0.5}$ for $Re_R > Re_{cr}$

The parameters in the equation, ν, β, y and R were determined experimentally, and their values were in agreement with the results of the flow studies.

An empirical equation, more readily evaluated, was derived in the form:

$$P = \frac{251\,(Nd_t)^{1.79}\,\eta^{0.66}\,n^{0.68}L}{(d_t - d_s)^{0.31}} \qquad \text{(for m.k.s.-units)}$$

6.1.3 Heat transfer

The mechanism for heat transfer in a SSHE consists of three steps:

- Penetration of heat by conduction in a thin layer close to the heat transfer surface in the time between two scrapings.
- Partial temperature equalization in the boundary layer that builds up on the blade.
- A convective radial transport from the cooled layer to the bulk of the liquid. Taylor vortices contribute to this radial transport.

The heat transfer coefficient can be described by an equation resulting from penetration theory, modified by an empirically determined correction factor:

$$Nu = 1.13\ (Re_R\ Pr\ n)^{0.5}\varphi$$

The correction factor φ has a value between 0.4 and 0.5 if Taylor vortices are present. Below the critical Reynolds number φ diminishes due to insufficient radial mixing.

At low mass flow rates the influence of the axial dispersion on the driving force for heat transfer is important. The apparent decrease in the heat transfer coefficient due to this effect can be calculated. To do so, the plug flow with dispersion model is applied, in which the axial dispersion coefficient is calculated from the standard deviation of the residence time distribution curve.

6.2 Design and scaling-up

In SSHEs high heat transfer coefficients are obtained when Taylor vortices are present. The geometry of the SSHE influences the flow regime: a wide annular space promotes instability. Furthermore, the power consumption is less when the value of $(d_t-d_s)/d_t$ is high.

For the same value of the blade velocity, the flow is more unstable in a SSHE with small tube diameter than in one with a large tube diameter. If a certain heat transfer area is required, a long, narrow SSHE is preferable to a short, large diameter apparatus. The increase in pressure drop can be reduced by increasing the annular space, as is mentioned above.

If the SSHE is operating in the Taylor-vortices regime, the heat transfer coefficient is proportional to the square root of the number of scrapings per unit time. However, the power consumption is approximately proportional to $N^{1.8}$ and $n^{0.7}$. The heat removal is therefore more efficient with a large number of scraper blades and a low shaft speed than with a smaller number of blades and a higher shaft speed, given the same number of scrapings per unit of time in both cases.

As the power comsumption is proportional to $d_t^{1.8}$ L, the power consumption in a long, small diameter SSHE is less than in a short one with the same heat transfer area.

Theoretically, then, the best way of scaling up is by increasing the length of a SSHE. Increase in pressure drop can be offset by widening the annular space. The heat transfer coefficient does not change and the power consumption increases linearly with the length. When for an increase in mass flow rate the length of the votator is increased proportionally, the power consumption per unit mass of working fluid retains its value.

If the heat transfer area is increased by increasing the diameter of the SSHE, the shaft speed should be reduced. If the blade velocity is the same for the small and the large unit, the power consumption per unit area of cooling surface is almost constant. By increasing the number of rows of scraper blades the heat transfer coefficient can be kept constant. A check should be made to ascertain whether the flow regime is the same for both cases.

CHAPTER 7
APPENDIX

7.1 The influence of the length of the SSHE on the tangential velocity profile

Two-dimensional viscous flow between parallel planes enclosing an object, e.g. a cylinder, is often referred to as Hele-Shaw flow[40]. The streamlines are equal in any plane parallel to the two boundary planes. In the model SSHE the flow cannot be described by the Hele-Shaw theory because of the rotating boundary that is formed by the outer tube.

In the following an attempt is made to estimate how flow, equidistant from front and back planes, is influenced by the finite length of the model. Two cases will be considered: flow that is caused by the pressure gradient due to the presence of the blades, and shear flow caused by the rotation of the outer wall. Instead of the flow between concentric cylinders the flow between two flat walls will be studied (see Fig. A1). The shaft of the SSHE is represented by the plane $x=o$, and the outer wall by $x=h$. The plane $x=h$ is moving in the z-direction with velocity v_o. If the SSHE is infinitely long, there are no boundaries in the y-direction. In our model SSHE, however, there are walls at $y=\pm d$ with $d=h$.

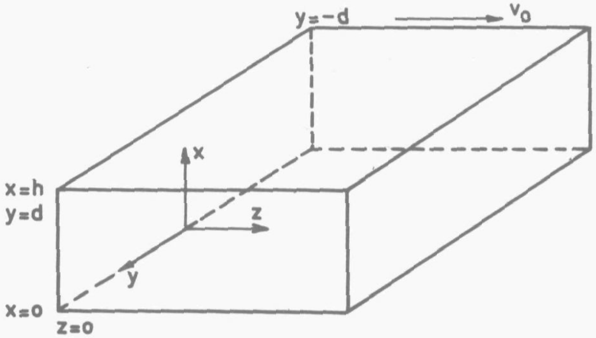

Fig. A1 Influence of the length of the votator on the flow pattern.

7.1.1 Pressure flow

In the derivation for pressure flow the outer wall will be considered to be stationary (v_o=0). For an infinitely long SSHE (d=∞) the velocity in the z-direction, v_z, between two parallel plates is given by:

$$v_z = \frac{dp}{dz} \cdot \frac{1}{8\eta} \left[h^2 - (h-2x)^2 \right] \qquad (A1)$$

in which

dp/dz = pressure gradient in z-direction

η = fluid viscosity

This yields: $v_z = \frac{dp}{dz} \cdot \frac{h^2}{8\eta}$ at $x = \frac{h}{2}$, $y = 0$.

For d≠∞ it is known[41]:

$$v_z = \frac{dp}{dz} \cdot \frac{1}{8\eta} \left[h^2-(h-2x)^2 - \frac{32}{h} \sum_{n=0}^{\infty} (-1)^n \frac{1}{m^3} \frac{\cosh m\left(\frac{h}{2} - x\right) \cosh my}{\cosh md} \right] \qquad (A2)$$

with m = $(2n+1)\pi/h$

With d=h it follows for x=h/2, y=0:

$$v_z = \frac{dp}{dz} \cdot \frac{h^2}{8\eta} \left[1 - \frac{32}{\pi^3} \sum_{n=0}^{\infty} \frac{(-1)^n}{(2n+1)^3} \cdot \frac{1}{\cosh (2n+1)\pi} \right] \qquad (A3)$$

Hence, the relative decrease of v_z at x=h/2, y=o due to the presence of the walls at y=±h is equal to[42]:

$$\frac{32}{\pi^3} \sum_{n=0}^{\infty} \frac{(-1)^n}{(2n+1)^3} \cdot \frac{1}{\cosh(2n+1)\pi} =$$

$$= \frac{32}{\pi^3} \left(\frac{1}{\cosh \pi} - \frac{1}{3^3 \cosh 3\pi} + \frac{1}{5^3 \cosh 5\pi} - \frac{1}{7^3 \cosh 7\pi} + \ldots\ldots \right) =$$

$$< \frac{32}{\pi^3} \left(\frac{1}{\cosh \pi} - \frac{1}{3^3 \cosh 3\pi} + \frac{1}{5^3} - \frac{1}{7^3} + \ldots\ldots \right) =$$

$$= \frac{32}{\pi^3} \left(\frac{1}{\cosh \pi} - \frac{1}{3^3 \cosh 3\pi} + 0.969 - 1 + 0.037 \right) = 0.095$$

The decrease in velocity at x=h/2 and y=0, due to the presence of walls at y=±h, instead of the situation in a SSHE of great length in the y-direction, is therefore smaller than 10%.

7.1.2 Shear flow

In shear flow the pressure gradient in the z-direction is zero and the flow is caused by the constant movement of the plane at x=h. For a long SSHE (d>>h), v_z at y=0 is given by:

$$v_z = \frac{x}{h} v_o \qquad \text{(A4)}$$

If d is equal to h, the velocity profile can be calculated from the equation of motion. Since $v_z \equiv v_y \equiv 0$, the equation of motion for the z-component becomes:

$$v_x \frac{\partial v_z}{\partial x} + v_y \frac{\partial v_z}{\partial y} + v_z \frac{\partial v_z}{\partial z} =$$

$$= - \frac{\partial p}{\partial z} + \eta \left(\frac{\partial^2 v_z}{\partial x^2} + \frac{\partial^2 v_z}{\partial y^2} + \frac{\partial^2 v_z}{\partial z^2} \right) + \rho g_z \qquad \text{(A5)}$$

If there is no pressure gradient, the influence of gravity is neglected, and the viscosity is constant, (A5) reduces (with $\partial v_z / \partial z = 0$) to:

$$\frac{\partial^2 v_z}{\partial x^2} + \frac{\partial^2 v_z}{\partial y^2} = 0 \; . \qquad \text{(A6)}$$

with boundary conditions:

$v_z = 0$ at $x = 0$, $-d \leqslant y \leqslant d$
$v_z = 0$ at $y = \pm d$, $0 \leqslant x \leqslant h$
$v_z = 0$ at $x = h$, $-d < y < d$

To solve the differential equation, the following substitution is made:

$$v_z = \frac{x}{h} v_o - v(x,y)$$

The differential equation and boundary conditions are transformed into:

$$\frac{\partial^2 v}{\partial x^2} + \frac{\partial^2 v}{\partial y^2} = 0 \qquad \text{(A7)}$$

$v=0$ at $x=0$ $-d \leqslant y \leqslant d$

$v=\frac{x}{h} v_o$ at $y=\pm d$, $0 \leqslant x \leqslant h$

$v=0$ at $x=h$, $-d < y < d$

The equation can be solved by separation of variables.

Assume: $v = X(x) \quad Y(y)$

and substitute this in (A7):

$$\frac{1}{X}\frac{d^2X}{dx^2} + \frac{1}{Y}\frac{d^2Y}{dy^2} = 0 \tag{A8}$$

Equation (A8) will be satisfied if

$$\frac{1}{X}\frac{d^2X}{dx^2} = -n^2 \quad \text{and} \quad \frac{1}{Y}\frac{d^2Y}{dy^2} = n^2, \tag{A9}$$

in which n has not yet been determined.

The general solutions of (A9) are:

$$X_n = C_{1n} \cos nx + C_{2n} \sin nx$$

$$Y_n = C_{3n} \cosh ny + C_{4n} \sinh ny$$

From the first boundary condition it follows: $C_{1n}=0$ and from the third: $n = \frac{\pi k}{h}$, with k=1,2,.... Obviously the solution must be symmetrical in y and hence $C_{4n}=0$. The solution of (A7) can therefore be written as:

$$v = \sum_{k=1}^{\infty} C_k \sin\left(\frac{\pi kx}{h}\right) \cosh\left(\frac{\pi ky}{h}\right)$$

The constants C_k can be evaluated by imposing the second boundary condition. Values of C_k must be found, for which is valid:

$$\frac{v_o x}{h} = \sum_{k=1}^{\infty} C_k \sin\left(\frac{\pi kx}{h}\right) \cosh \pi k \tag{A10}$$

(A10) is multiplied by $\sin\left(\frac{\pi mx}{h}\right)$ and integrated over x between x=0 and x=h. The result is:

$$C_1 = 5.52 \times 10^{-2} v_o$$

$$C_2 = -11.92 \times 10^{-4} v_o$$

$$C_3 = 3.24 \times 10^{-5} v_o$$

$$C_4 = -11.10 \times 10^{-7} v_o$$

and hence:

$$\frac{v}{v_o} = 5.52 \times 10^{-2} \sin\frac{\pi x}{h} \cosh\frac{\pi y}{h} +$$
$$-11.92 \times 10^{-4} \sin\frac{2\pi x}{h} \cosh\frac{2\pi y}{h} +$$
$$+ 3.24 \times 10^{-5} \sin\frac{3\pi x}{h} \cosh\frac{3\pi y}{h} +$$
$$-11.10 \times 10^{-7} \sin\frac{4\pi x}{h} \cosh\frac{4\pi y}{h} + \ldots\ldots$$

$\frac{v}{v_o}$ is the relative deviation of v_z from that of a SSHE of infinite length.

For y=0 and $x=\frac{h}{2}$, $\frac{v}{v_o} = 5.52 \times 10^{-2} - 3.24 \times 10^{-5} + \ldots$

For the infinitely long SSHE at y=0 and $x=\frac{h}{2}$, $\frac{v_z}{v_o} = 0.5$ and the change in velocity caused by the finite length is 11%.

The result of these calculations shows that the small length of the model SSHE does not influence the velocity in the plane equidistant to front and back plane by more than ca. 10%.

7.2 The determination of velocity profiles

Consider the flow between two parallel planes at x=0 and x=h. If the plane at x=0 moves steadily in the z-direction, with velocity v_o and void of pressure gradients, the velocity is given by:

$$\frac{v_z}{v_o} = 1 - \frac{x}{h} \qquad \text{(A11)}$$

(This situation is different from that in Chapter 7.1 where the plane at x=0 is static and the plane at x=h is dynamic).

The displacement of the liquid as a result of a temporary motion of the plane at x=0 will now be calculated. The velocity during the displacement satisfies the partial differential equation:

$$\frac{\partial v_z}{\partial t} = \nu \frac{\partial^2 v_z}{\partial x^2}$$

where ν is the kinematic viscosity of the fluid, with side conditions:

$v_z = 0$ at $t = 0$, $0 \leqslant x \leqslant h$
$v_z = v_o$ at $x = 0$, $t > 0$
$v_z = 0$ at $x = h$, $t \geqslant 0$

The solution to this problem is given in the literature[13]:

$$v_z = v_o \left(1 - \frac{x}{h}\right) + \frac{2}{\pi} \sum_{n=1}^{\infty} \left\{ - \frac{v_o}{n} \sin \left(\frac{n\pi x}{h}\right) \exp \left(- \frac{\nu n^2 \pi^2 t}{h^2}\right)\right\} \qquad \text{(A12)}$$

Assume that the movement of the plane ends at $t = t_o$, then the displacement of the liquid at $t = t_o$ can be calculated by integrating (A12)

$$S_I = \int_0^{t_o} v_z \, dt = v_o t_o \left(1 - \frac{x}{h}\right) +$$

$$- \frac{2\, v_o h^2}{\pi^3 \nu} \sum_{n=1}^{\infty} \left\{ \frac{1}{n^3} \sin \left(\frac{n\pi x}{h}\right) \left[1 - \exp \left(- \frac{\nu n^2 \pi^2 t_o}{h^2}\right)\right]\right\}$$

For $t > t_o$ the situation is different with respect to the boundary conditions: $v_z = 0$ at $x = 0$ and $x = h$, and the velocity of the liquid damps out.
Let: $t_1 = t - t_o$. The velocity for $t > t_o$ and hence $t_1 > 0$ satisfies the differential equation:

$$\frac{\partial v_z}{\partial t_1} = \nu \frac{\partial^2 v_z}{\partial x^2} \qquad \text{(A13)}$$

with side conditions:

$v_z = 0$ at $x = 0$ and $x = h$, $t_1 > 0$

$$v_z = v_o \left(1 - \frac{x}{h}\right) + \frac{2}{\pi} \sum_{n=1}^{\infty} \left\{ - \frac{v_o}{n} \sin \left(\frac{n\pi x}{h}\right) \exp \left(- \frac{\nu n^2 \pi^2 t_o}{h^2}\right)\right\}$$

at $t_1 = 0$, $0 < x < h$

The solution of (A13) is again given in the literature[13]:

$$v_z = \frac{2}{h} \sum_{m=1}^{\infty} \left\{ \sin \left(\frac{m\pi x}{h}\right) \exp \left(- \frac{\nu m^2 \pi^2 t_1}{h^2}\right) \int_0^h v_z(x)\Big|_{t_1=0} \sin \left(\frac{m\pi x}{h}\right) dx \cdot \right\} \qquad \text{(A14)}$$

This displacement after $t = t_o$ can be calculated by integrating (A14):

$$S_{II} = \int_0^{\infty} v_z \, dt_1$$

$$= \frac{2}{h} \sum_{m=1}^{\infty} \left\{ \sin \left(\frac{m\pi x}{h}\right) . \frac{h^2}{\nu m^2 \pi^2} \left[\int_0^h v_z(x)\Big|_{t_1=0} \sin \left(\frac{m\pi x}{h}\right) dx \right]\right\} \qquad \text{(A15)}$$

The integral in (A15) can be split into three parts and evaluated:

$$\int_0^h \left[v_o - v_o \frac{x}{h} + \frac{2}{\pi} \sum_{n=1}^{\infty} \left\{ - \frac{v_o}{n} \sin\left(\frac{n\pi x}{h}\right) \exp\left(- \frac{\nu n^2 \pi^2 t_o}{h^2}\right)\right\} \right] \sin\left(\frac{m\pi x}{h}\right) dx =$$

$$\int_0^h v_o \sin\left(\frac{m\pi x}{h}\right) dx - \int_0^h v_o \frac{x}{h} \sin\left(\frac{m\pi x}{h}\right) dx +$$

$$+ \int_0^h \frac{2}{\pi} \sum_{n=1}^{\infty} \left\{ - \frac{v_o}{n} \sin\left(\frac{n\pi x}{h}\right) \exp\left(- \frac{\nu n^2 \pi^2 t_o}{h^2}\right)\right\} \sin\left(\frac{m\pi x}{h}\right) dx = - \frac{hv_o}{m\pi} \left[(-1)^m - 1 \right] +$$

$$+ \frac{hv_o}{m\pi} (-1)^m + \frac{hv_o}{m\pi} \cdot \exp\left(- \frac{\nu m^2 \pi^2 t_o}{h^2}\right) = \frac{hv_o}{m\pi} \left[1 + \exp\left(- \frac{\nu m^2 \pi^2 t_o}{h^2}\right)\right] \qquad \text{(A16)}$$

Substitution of (A16) in (A14) yields:

$$S_{II} = \frac{2 v_o h^2}{\pi^3 \nu} \sum_{m=1}^{\infty} \left\{ \frac{1}{m^3} \sin\left(\frac{m\pi x}{h}\right) \left[1 + \exp\left(- \frac{\nu m^2 \pi^2 t_o}{h^2}\right)\right] \right\}$$

For the total displacement of the liquid elements is found:

$$S = S_I + S_{II} = v_o t_o \left(1 - \frac{x}{h}\right), \text{ or: } \frac{S}{v_o t_o} = 1 - \frac{x}{h} \qquad \text{(A17)}$$

From comparing (A17) and (A11) it follows that the method to determine velocity profiles is valid.

7.3 Results of power consumption experiments

Table A1

Experimental results for 46 x 10^{-3} m shaft

n	N ($rev.s^{-1}$)	η ($N.s.m^{-2}$)	Re_R	Po
2	5.83	1.61	26.2	40.5
2	8.33	1.70	35.4	26.6
2	12.2	1.59	55.5	16.4
2	16.7	1.60	75.5	11.3
2	25.4	1.45	127	6.70
2	33.3	1.27	189	4.59
2	12.2	0.47	187	8.55
2	16.7	0.48	259	6.20
2	25.4	0.46	401	3.71
2	33.3	0.44	555	2.69
2	33.3	0.118	2040	1.10
4	4.00	1.79	16.1	121
4	5.83	1.79	23.6	76.2
4	8.33	1.75	34.4	48.1
4	12.2	1.67	52.5	27.5
4	16.7	1.55	77.5	18.5
4	25.4	1.36	135	10.6
4	5.83	0.46	87.5	32.8
4	8.33	0.46	131	22.7
4	12.2	0.46	193	14.7
4	16.7	0.44	278	10.1
4	25.4	0.45	407	6.01
4	33.3	0.40	595	4.36
4	16.7	0.124	970	3.78
4	25.4	0.122	1200	2.62
4	33.3	0.120	2000	2.00
6	4.00	1.60	18.0	164
6	5.83	1.59	26.5	102
6	8.33	1.72	35.0	62.5
6	12.2	1.72	51.0	36.1
6	16.7	1.53	94.5	24.0
6	25.4	1.27	144	13.6
6	4.00	0.46	62.5	66.5
6	5.83	0.46	87.5	45.3
6	8.33	0.46	132	30.7
6	12.2	0.45	195	19.8
6	16.7	0.44	281	14.0
6	25.4	0.42	439	7.95
6	16.7	0.123	980	5.20
6	25.4	0.120	1530	3.53
6	33.3	0.118	2040	2.65

Table A2

Experimental results for 56 x 10^{-3} m shaft

n	N (rev.s^{-1})	η (N.s.m^{-2})	Re_R	Po
2	4.00	1.86	15.5	77.5
2	5.83	1.79	23.5	46.7
2	8.33	1.53	39.3	27.2
2	12.2	1.79	49.1	18.4
2	16.7	1.78	67.5	11.2
2	25.4	1.40	131	6.95
2	12.2	0.37	237	7.35
2	16.7	0.43	283	6.25
2	25.4	0.39	474	3.63
2	33.3	0.33	725	2.33
2	25.4	0.113	1630	1.55
2	33.3	0.105	2290	1.15
4	4.00	1.34	21.6	122
4	5.83	1.35	31.2	76.5
4	8.33	1.35	44.5	48.5
4	12.2	1.32	66.5	27.7
4	16.7	1.24	97.0	17.9
4	25.4	1.13	162	10.5
4	5.83	0.43	97.5	34.1
4	8.33	0.44	138	22.8
4	12.2	0.44	199	14.4
4	16.7	0.44	274	10.1
4	25.4	0.43	425	6.25
4	33.3	0.42	579	4.57
4	16.7	0.116	1040	4.37
4	25.4	0.115	1590	2.77
4	33.3	0.114	2110	2.10
6	4.00	1.21	23.9	159
6	5.83	1.17	36.0	98.5
6	8.33	1.13	53.0	62.0
6	12.2	1.10	80.0	35.5
6	16.7	1.06	113	22.3
6	25.4	0.93	197	12.3
6	4.00	0.44	65.5	74.5
6	5.83	0.44	97.0	49.0
6	8.33	0.43	140	31.2
6	12.2	0.43	205	18.9
6	16.7	0.40	304	12.6
6	25.4	0.38	483	7.65
6	33.3	0.36	675	5.40
6	12.2	0.117	750	8.15
6	16.7	0.116	1040	5.80
6	25.4	0.115	1590	3.63
6	33.3	0.112	2150	2.71

Table A3

Experimental results for 62 x 10^{-3} m shaft

n	N (rev.s^{-1})	η (N.s.m^{-2})	Re_R	Po
2	4.00	1.65	17.5	90.5
2	5.83	1.65	25.5	58.5
2	8.33	1.65	36.4	37.2
2	12.2	1.60	55.0	21.2
2	16.7	1.56	77.0	14.0
2	25.4	1.43	128	7.60
2	33.3	1.23	196	5.10
2	12.2	0.42	212	8.50
2	16.7	0.41	296	6.10
2	25.4	0.40	453	3.70
2	33.3	0.40	610	2.90
2	33.3	0.111	2160	1.20
4	4.00	2.10	13.8	180
4	5.83	2.06	20.4	113
4	8.33	2.01	29.9	69
4	12.2	1.92	45.8	38.7
4	16.7	1.80	67.0	23.8
4	5.83	0.40	106	31.8
4	8.33	0.41	147	22.0
4	12.2	0.39	223	13.6
4	16.7	0.40	301	9.85
4	25.4	0.37	491	5.75
4	33.3	0.35	685	4.21
4	25.4	0.105	1750	2.20
4	33.3	0.103	2340	1.76
6	4.00	1.67	17.3	220
6	5.83	1.66	25.4	136
6	8.33	1.62	37.1	82.5
6	12.2	1.56	56.5	46.3
6	16.7	1.47	82.0	28.7
6	4.00	0.40	72.5	66.0
6	5.83	0.40	106	44.2
6	8.33	0.40	151	30.0
6	12.2	0.39	224	18.6
6	16.7	0.38	315	12.4
6	25.4	0.37	492	7.65
6	33.3	0.35	685	5.45
6	12.2	0.119	740	7.00
6	16.7	0.120	1000	5.30
6	25.4	0.116	1580	3.41
6	33.3	0.107	2250	2.63

Table A4

Experimental results for 68 x 10^{-3} m shaft

n	N ($rev.s^{-1}$)	η ($N.s.m^{-2}$)	Re_R	Po
2	4.00	1.42	20.4	132
2	5.83	1.42	29.7	83.5
2	8.33	1.41	42.6	54.5
2	12.2	1.32	66.5	32.5
2	16.7	1.22	98.5	20.9
2	25.4	1.11	165	11.0
2	5.83	0.42	100	32.3
2	8.33	0.42	145	21.2
2	12.2	0.41	218	13.2
2	16.7	0.40	313	8.95
2	25.4	0.39	475	5.30
2	33.3	0.37	645	3.74
4	4.00	1.11	26.0	158
4	5.83	1.10	38.3	104
4	8.33	1.06	56.5	67.5
4	12.2	1.02	86.0	40.3
4	16.7	0.96	125	25.6
4	25.4	0.88	209	13.5
4	4.00	0.46	63.0	70.5
4	5.83	0.45	93.0	45.6
4	8.33	0.46	131	31.4
4	12.2	0.46	189	20.3
4	16.7	0.44	272	13.5
4	25.4	0.42	434	7.90
4	33.3	0.40	600	5.45
6	4.00	1.20	24.1	216
6	5.83	1.18	35.7	139
6	8.33	1.16	52.0	88.5
6	12.2	1.11	79.0	52.0
6	16.7	1.07	113	33.1
6	4.00	0.49	59.5	89.0
6	5.83	0.49	86.5	59.0
6	8.33	0.48	125	40.1
6	12.2	0.47	186	26.1
6	16.7	0.46	259	17.6
6	25.4	0.44	417	10.1

7.4 Analysis of heat transfer mechanism in cylinder wall

Consider a semi-infinite body in the space $z \leqslant 0$ (see Fig. A2) and moving with velocity v_o in positive x-direction. A heat source in the plane $z = 0$ is bounded by $x = \pm \frac{s}{2}$ and has infinite length in the y-direction.

The heat flux from the source is Q':

Let:

$$X = \frac{v_o x}{2a_w}\ ; \quad Z = \frac{v_o z}{2a_w}\ ; \quad B = \frac{v_o s}{4a_w}$$

The temperature for $Z \leqslant 0$ is given by[13]:

$$T = \frac{2\ a_w Q'}{\pi \lambda_w v_o} \int_{X-B}^{X+B} e^u K_o\ (Z^2 + u^2)^{\frac{1}{2}}\ du \tag{A18}$$

K_o is the modified Bessel function of the second kind and zero order.

For the wall, $Z = 0$ Eq. (A18) yields:

$$T = \frac{2\ a_w Q'}{\pi \lambda_w v_o} \int_{X-B}^{X+B} e^u K_o |u| du \tag{A19}$$

This can be rewritten as:

$$T . \frac{\pi \lambda_w v_o}{2\ a_w Q'} \int_{X-B}^{X+B} e^u K_o |u| du = \int_0^{X+B} e^u K_o |u| du\ +$$

$$+ \int_{X-B}^{0} e^u K_o |u| du = \int_0^{X+B} e^u K_o |u| du + \int_0^{B-X} e^{-u} K_o |u| du =$$

$$= (B + X)\ e^{B+X} \left\{ K_o\ (B + X) + K_1\ (B + X) \right\} - 1\ +$$

$$+\ (B - X)\ e^{-(B-X)} \left\{ K_o\ (B - X) + K_1\ (B - X) \right\} + 1 \tag{A20}$$

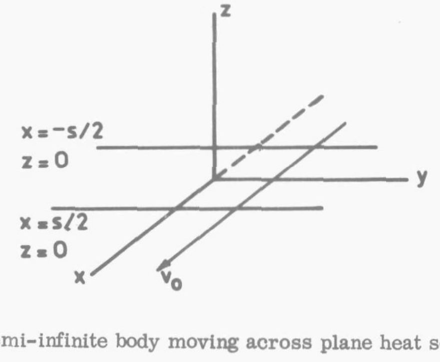

Fig. A2 Semi-infinite body moving across plane heat source.

$$= \int_0^2 y\left\{K_o(y) + K_1(y)\right\}(e^y + e^{-y})dy +$$

$$+ \int_2^{2B} y\left\{K_o(y) + K_1(y)\right\}(e^y + e^{-y})\, dy \qquad \text{(A21)}$$

The order of magnitude of B is 10. The integral in (A21) between 0 and 2 will be calculated numerically.

For $y > 2$ the Bessel functions can be written approximately:

$$K_o(y) \approx K_1(y) \approx \frac{1.25}{e^y \sqrt{y}}$$

and hence:

$$\int_2^{2B} y\left\{K_o(y) + K_1(y)\right\}(e^y + e^{-y})\, dy \approx \int_2^{2B} y \frac{2.50}{e^y \sqrt{y}} (e^y + e^{-y})\, dy =$$

$$= 2.50 \int_2^{2B} \sqrt{y}\, dy + 2.50 \int_2^{2B} e^{-2y} \sqrt{y}\, dy =$$

$$= 4.72\left(B\sqrt{B} - 1\right) + 1.77 \int_2^{2\sqrt{B}} y^2 e^{-y^2}\, dy =$$

$$= 4.72\left(B\sqrt{B} - 1\right) + \frac{1.77}{2}\left[-y\, e^{-y^2}\right]_2^{2\sqrt{B}} + \frac{1.77}{2} \int_2^{2\sqrt{B}} e^{-y^2}\, dy =$$

$$= 4.72\left(B\sqrt{B} - 1\right) - 1.77\sqrt{B}\, e^{-4B} + 0.033 +$$

$$+ \frac{1.77}{4}\sqrt{\pi}\,(\text{erf } 2\sqrt{B} - \text{erf } 2) \approx 4.72\, B\sqrt{B} - 4.69$$

To calculate the integral in (A21) between 0 and 2, we evaluate

$$f(y) = y\left\{K_o(y) + K_1(y)\right\}(e^y + e^{-y})$$

for $y = 0, 0.5, 1, 1.5$ and 2.

$f(0) = 2.00$
$f(0.5) = 2.90$
$f(1) = 3.19$
$f(1.5) = 3.48$
$f(2) = 3.82$

The application of Simpson's rule gives:

The average temperature of the heat source, $\langle T \rangle$, is given by:

$$\langle T \rangle \frac{\pi \lambda_w v_o}{2\, a_w Q'} \quad 2\,B =$$

$$= \int_{-B}^{B} (B + X)\, e^{B + X}\, K_o(B + X)\, dX + \int_{-B}^{B} (B + X)\, e^{B + X} K_1(B + X)\, dX$$

$$+ \int_{-B}^{B} (B - X)\, e^{-(B - X)}\, K_o(B - X)\, dX + \int_{-B}^{B} (B - X)\, e^{-(B-X)} K_1\,(B - X)$$

$$\int_0^2 f\,(y)\,dy = \frac{0.5}{3} \left\{ 2.00 + 4\,(2.90 + 3.48) + 2\,(3.19) + 3.82 \right\} = 6.29$$

From (A21) it now follows:

$$\langle T \rangle \frac{\pi \lambda_w v_o}{2\, a_w Q'} \;.\; 2\,B = 4.72\, B\sqrt{B} - 4.69 + 6.29 = 4.72\, B\sqrt{B} - 1.60, \text{ or,}$$

approximately:

$$\langle T \rangle \frac{\pi \lambda_w v_o}{2\, a_w Q'} = 2.36\sqrt{B} \qquad \text{(A22)}$$

If we define a heat transfer coefficient α^* between the source and the semi-infinite body by:

$$\alpha^* = \frac{Q'}{\langle T \rangle}\,,$$

it follows from (A22):

$$\alpha^* = \frac{0.655\, \rho_w c_w v_o}{\sqrt{B}} = 0.665 \sqrt{\frac{\rho_w c_w \lambda_w \; 4\, v_o}{s}}$$

or:

$$\alpha^* = 2.36 \sqrt{\frac{d_t N \rho_w c_w \lambda_w}{s}} \qquad \text{(A23)}$$

It is possible to approximate this result by applying penetration theory. As the contact time between the blade edge and a point at the wall is $\frac{s}{\pi d_t N}$, the heat transfer coefficient, calculated from one-dimensional penetration of heat in a semi-infinite body is:

$$\alpha^* = 2.00 \sqrt{\frac{d_t N \rho_w c_w \lambda_w}{s}} \qquad \text{(A24)}$$

The difference between the results of (A23) and (A24) is 18%.

7.5 The steady state approximation in the model for power consumption

It has been assumed in Chapter 4.4.1.1 that the conditions in the liquid between the edge of the blade and the tube wall are stationary. However, this liquid is continuously refreshed. It may be asked whether the steady state temperature and viscosity are reached within a relatively short time, so that the analysis in 4.4.1.1 is justified. For a simplified case, in which the blade and the wall are heat absorbers with temperature T=0, this will now be demonstrated.

The origin of the coordinate system is central between the edge of the scraper blade and the tube wall. The viscous dissipation begins at t=0.

The mathematical model can be formulated as follows:

$$\rho c_p \frac{\partial T}{\partial t} = \lambda \frac{\partial^2 T}{\partial z^2} + \frac{\eta^* v_o^2}{\delta^2}$$

with side conditions:

(1) $T = 0$ at $t = 0$, $\frac{-\delta}{2} \leqslant z \leqslant \frac{\delta}{2}$

(2) $T = 0$ at $t \geqslant 0$, $z = \frac{-\delta}{2}$ and $z = \frac{\delta}{2}$

The solution of this problem is given in the literature[13]:

$$T = \frac{\eta^* v_o^2}{8\lambda} \left\{ 1 - \frac{4z^2}{\delta^2} - \frac{32}{\pi^3} \sum_{n=0}^{\infty} \frac{(-1)^n}{(2n+1)^3} \cdot \left\{ \cos \frac{(2n+1)\pi z}{\delta} \exp\left(\frac{-\lambda (2n+1)^2 \pi^2 t}{\rho c_p \delta^2} \right) \right\} \right. \tag{A25}$$

The average value of T in the space can be calculated:

$$\Delta T = \frac{1}{\delta} \int_{-\frac{\delta}{2}}^{\frac{\delta}{2}} T \, d z \tag{A26}$$

From (A25) and (A26) it follows:

$$\Delta T = \frac{\eta^* v_o^2}{12\lambda} \left[1 - \frac{96}{\pi^4} \sum_{n=0}^{\infty} \frac{\exp\left\{ \frac{-\lambda (2n+1)^2 \pi^2 t}{\rho c_p \delta^2} \right\}}{(2n+1)^4} \right] \tag{A27}$$

To evaluate the influence of the transient term in (A27) the value of δ must be estimated. Let us assume for the moment that $\delta = 2 \times 10^{-6}$ m (see Chapter 4) and $\lambda/\rho c_p = 1.0 \times 10^{-7}$ $m^2.s^{-1}$. We can now calculate for which value of t the contribution of the transient term in (A27) is less than 10%. The following equation must be solved:

$$\frac{96}{\pi^4} \sum_{n=0}^{\infty} \frac{\exp\left\{\dfrac{-\lambda\ (2n+1)^2 \pi^2\ t}{\rho c_p \delta^2}\right\}}{(2n+1)^4} = 0.1$$

or:

$$\sum_{n=0}^{\infty} \frac{\exp\left\{\dfrac{-\lambda (2n+1)^2 \pi^2\ t}{\rho c_p \delta^2}\right\}}{(2n+1)^4} = 0.1 \qquad \text{(A28)}$$

The first term in the left hand side of (A28) is $\exp\left(\frac{-\pi^2\ \lambda t}{\rho c_p \delta^2}\right)$

Assume for the moment that the other terms may be neglected. In this case:

$$\exp\left(-\frac{\pi^2\ \lambda t}{\rho c_p \delta^2}\right) = 0.1$$

and: $$\frac{\lambda\ t}{\rho c_p \delta^2} = 0.231, \text{ or } t = 0.92 \times 10^{-5} \text{ s.}$$

The time required for the passing of the edge of the blade at any point of the wall is s/v_o, and with $s = 0.2 \times 10^{-3}$ m, $v_o = 4$ m.s^{-1}, this time is 0.5×10^{-4} s. The steady state is reached within 18% of the total time, and therefore the steady state approximation is justified.

The truncation of the series in (A28) after the first term will now be considered. With $t = 0.92 \times 10^{-5}$ s, the series can be written as follows:

$$0.1 + \frac{(0.1)^{3^2}}{3^4} + \frac{(0.1)^{5^2}}{5^4} + \frac{(0.1)^{7^2}}{7^4} + \ldots\ldots\ldots$$

The sum of this series is smaller than that of the geometric progression:

$$0.1 + (0.1)^3 + (0.1)^5 + (0.1)^7 + \ldots\ldots = \frac{0.1}{1-0.01}$$

In the latter, the first term accounts for 99% of the sum of the series; hence the truncation after the first term was allowed.

7.6 The influence of a flow of fluid on the penetration of heat

The contraction and subsequent expansion of the streamlines which are caused by the passage of the blade can be compared with the flow between two plane walls, one of which is oscillating.

Let liquid fill the space $x > 0$ and be bounded by a stationary wall at $x = 0$ and an oscillating wall parallel to this stationary wall somewhere in the liquid. At $t = 0$ the temperature is zero for all $x > 0$. For $t > 0$ the wall temperature is T_o.

Assume that a flow is induced in the liquid by the plane that oscillates in the x-direction. The flow is two-dimensional (independent of y) and is symmetrical about $z = 0$. We suppose that the flow is similar to the two-dimensional stagnation point flow[36]. For this type of flow the following is valid:

$$v_z \sim xz \quad \text{and} \quad v_x \sim -x^2 \tag{A29}$$

The oscillating movement has the form:

$$\left.\begin{aligned} v_z &= 2A\, xz \sin\omega t \\ v_x &= -A\, x^2 \sin\omega t \end{aligned}\right\} \tag{A30}$$

The equation of energy reads[38]:

$$\frac{\partial T}{\partial t} + v_x \frac{\partial T}{\partial x} + v_z \frac{\partial T}{\partial z} = a \left(\frac{\partial^2 T}{\partial x^2} + \frac{\partial^2 T}{\partial z^2} \right) \tag{A31}$$

The temperature gradient in the x-direction is much greater than that in the z-direction and therefore:

$$\frac{\partial T}{\partial z} << \frac{\partial T}{\partial x} \quad \text{and} \quad \frac{\partial^2 T}{\partial z^2} \ll \frac{\partial^2 T}{\partial x^2}$$

Thus, to find the temperature profile in the area around $x = 0$, $z = 0$ the following partial differential equation must be solved:

$$\frac{\partial T}{\partial t} = A\, x^2 \sin\omega t \frac{\partial T}{\partial x} + a \frac{\partial^2 T}{\partial x^2} \tag{A32}$$

with side conditions:

at $t = 0$; $T = 0$ for $x \geqslant 0$

at $x = 0$; $T = T_o$ for $t > 0$

To find a solution of (A32) the temperature is written in the form:

$$T = f_o(t) + xf_1(t) + x^2 f_2(t) + \ldots\ldots + x^n f_n(t) + \ldots. \qquad \text{(A33)}$$

$f_n(t)$ are functions of t only that have not yet been determined. After differentiating of (A33) it follows:

$$\frac{\partial T}{\partial x} = f_1\ (t) + 2xf_2(t) + 3x^2 f_3(t) + \ldots\ldots + n\ x^{n-1} f_n(t) + \ldots\ldots \qquad \text{(A34)}$$

$$\frac{\partial^2 T}{\partial x^2} = 2\ f_2(t)+3.2\ xf_3(t)+4.3\ x^2 f_4(t) + \ldots\ldots + n(n-1)\ x^{n-2}\ f_n(t) + \ldots. \qquad \text{(A35)}$$

$$\frac{\partial T}{\partial t} = f_o'(t)+xf_1'(t) + x^2 f_2'(t) + \ldots\ldots + x^n f_n'(t) + \ldots \qquad \text{(A36)}$$

(The apostrophe indicates differentiation with respect to t).

Eqs. (A34)-(A36) are substituted in (A32). The result is:

$$\sum_{n=o}^{\infty} x^n \frac{df_n}{dt} = Ax^2\ \sin\omega\, t \sum_{n=1}^{\infty} nx^{n-1} f_n + a \sum_{n=2}^{\infty} n(n-1)\ x^{n-2} f_n \qquad \text{(A37)}$$

From the first boundary condition it follows $f_o(t) \equiv T_o$. Equation (A37) is satisfied if the coefficients of each distinct power of x are identically zero. This means:

$$\frac{df_n}{dt} = A\ (\sin\omega\, t)\ (n-1)\ f_{n-1} + a(n+2)\ (n+1) f_{n+2} \qquad \text{(A38)}$$

For n=0:

$$\frac{df_o}{dt} = 2\ af_2 \text{ and hence } f_2 = 0.$$

For n=1:

$$\frac{df_1}{dt} = 6\ af_3 \text{ and hence } f_3 = \frac{1}{6a}\ \frac{df_1}{dt}$$

For n=2: $f_4 = \dfrac{-f_1 A\ \sin\omega\, t}{12a}$

For n=3: $f_5 = \dfrac{1}{120a^2}\ \dfrac{d^2 f_1}{dt^2}$

For n=4: $$f_6 = \frac{-\frac{df_1}{dt} A\ (\sin \omega\, t) \left(1 - \frac{1}{2a} \right) - f_1\, A \omega\, \cos \omega\, t}{30a}$$

For n=n: $$f_{n+2} = \frac{\frac{df_n}{dt} - A(\sin \omega\, t)\ (n-1) f_{n-1}}{a(n+1)\ (n+2)}$$

The solution of (A32) can be written in the form:

$$T = T_o + x f_1 + x^3 \frac{x^3}{a.3!} \cdot \frac{df_1}{dt} + \frac{x^5}{a^2.5!} \cdot \frac{d^2 f_1}{dt^2} + \frac{x^7}{a^3.7!} \cdot \frac{d^3 f_1}{dt_3} + \dots + $$

$$\frac{x^4}{12a} (f_1\ A\ \sin \omega\, t) + \frac{x^6}{30} \left(- \frac{df_1}{dt} A(\sin \omega\, t)\ (1 - \frac{1}{2a}) - f_1\ A\ \omega\ \cos \omega\, t \right) +$$

$$\frac{x^7}{126a^2} \left(-A^2\, f_1\, \sin^2\, \omega\, t \right) + \dots \qquad \text{(A29)}$$

The heat flux at x = 0 is therefore equal to:

$$q = \lambda \frac{\partial T}{\partial y} \bigg|_{y\,=\,0} = -\lambda f_1 \qquad \text{(A40)}$$

For A = 0 we have the situation of pure conduction.

This means $f_1 = \frac{T_o}{\sqrt{\pi a t}}$

Finite values of A have no influence on f_1. This calculation has demonstrated that the contraction and expansion of streamlines has no influence on the heat flux at the wall.

7.7 Results of heat transfer measurements

Table A5

Influence of mass flow rate on the heat transfer coefficient at various shaft speeds

Shaft speed (rev. s^{-1})	Mass flow rate (kg. s^{-1})	Viscosity (N. s. m^{-2})	Loss of sensible heat (W)	Frictional heat (W)	Overall heat transfer coefficient (W. m^{-2}. $^{o}C^{-1}$)	Scraped side heat transfer coefficient (W. m^{-2}. $^{o}C^{-1}$)	φ
4.00	0.0131	0.125	1360	67	665	735	0.23
4.00	0.0206	0.097	1900	61	760	880	0.28
4.00	0.0272	0.122	1950	58	795	900	0.29
4.00	0.0364	0.094	2280	53	810	920	0.29
4.00	0.050	0.092	2560	49	880	1000	0.32
4.00	0.136	0.113	1870	60	690	770	0.24
4.00	0.181	0.113	1710	61	630	695	0.22
4.00	0.256	0.120	1470	65	570	620	0.20
4.00	0.364	0.122	1910	65	735	820	0.26
4.00	0.600	0.108	2460	62	67	735	0.23
10.0	0.0131	0.202	1720	615	900	955	0.20
10.0	0.0234	0.152	3190	515	1210	1410	0.31
10.0	0.0361	0.133	4490	420	1370	1690	0.36
10.0	0.050	0.140	4710	375	1370	1690	0.36
10.0	0.138	0.184	4780	360	1450	1830	0.39
10.0	0.167	0.161	5310	335	1460	1840	0.39
10.0	0.257	0.146	6160	305	1600	2080	0.49
10.0	0.367	0.180	5650	360	1600	2060	0.44
10.0	0.570	0.127	6100	315	1500	1910	0.40
25.0	0.0131	0.097	1480	1450	1290	1580	0.20
25.0	0.0206	0.111	2060	1410	1570	2020	0.25
25.0	0.0272	0.120	2490	1300	1740	2320	0.29
25.0	0.0364	0.126	2860	1300	1900	2620	0.33
25.0	0.050	0.131	3420	1150	2050	2900	0.37
25.0	0.136	0.120	4810	1070	2320	3470	0.44
25.0	0.180	0.120	4580	1040	2200	3200	0.40
25.0	0.256	0.143	4220	1150	2310	3400	0.43
25.0	0.364	0.127	4680	1090	2300	3430	0.43
25.0	0.600	0.117	5210	1050	2400	3580	0.45

Table A6

Influence of mass flow rate on the heat transfer coefficient at various viscosities

Mass flow rate (kg. s^{-1})	Viscosity (N. s. m^{-2})	Loss of sensible heat (W)	Frictional heat (W)	Overall heat transfer coefficient (W. m^{-2}. $^{o}C^{-1}$)	Scraped side heat transfer coefficient (W. m^{-2}. $^{o}C^{-1}$)	φ
0.0131	0.480	950	615	915	1040	0.22
0.0195	0.430	1360	585	1040	1230	0.26
0.0267	0.510	1400	575	1110	1320	0.28
0.0375	0.370	2250	495	1210	1460	0.31
0.0497	0.450	1980	500	1180	1430	0.30
0.138	0.450	2100	490	1220	1470	0.31
0.174	0.450	2480	540	1230	1480	0.32
0.257	0.435	2360	505	1300	1600	0.34
0.372	0.415	2470	360	1090	1300	0.27
0.600	0.395	1890	535	1040	1220	0.26
0.0131	0.202	1720	615	900	955	0.20
0.0234	0.152	3190	515	1210	1410	0.31
0.0361	0.133	4490	420	1370	1690	0.36
0.050	0.140	4710	375	1370	1690	0.36
0.138	0.184	4780	360	1450	1830	0.39
0.167	0.161	5310	335	1460	1840	0.39
0.257	0.146	6160	305	1600	2080	0.49
0.367	0.180	5650	360	1600	2060	0.44
0.570	0.127	6100	315	1500	1910	0.40
0.0128	0.048	2190	150	1290	1580	0.30
0.0197	0.042	2390	150	1430	1790	0.35
0.0256	0.040	2920	129	1530	1950	0.38
0.0361	0.044	3390	132	1650	2160	0.42
0.0489	0.041	3880	115	1690	2220	0.43
0.132	0.047	3830	130	1620	2120	0.41
0.179	0.037	4950	117	1740	2320	0.45
0.243	0.045	4250	124	1710	2240	0.43
0.386	0.040	4500	126	1660	2160	0.42
0.578	0.040	4400	123	1640	2140	0.41

Table A7

Influence of shaft speed on the heat transfer coefficient at various viscosities

Shaft speed ($rev.s^{-1}$)	Mass flow rate ($kg.s^{-1}$)	Viscosity ($N.s.m^{-2}$)	Loss of sensible heat (W)	Frictional heat (W)	Overall heat tranfer coefficient ($W.m^{-2}.{}^{o}C^{-1}$)	Scraped side heat transfer coefficient ($W.m^{-2}.{}^{o}C^{-1}$)	φ
4.00	0.174	0.445	1290	165	560	605	0.20
5.85	0.174	0.450	1330	300	630	775	0.22
8.35	0.174	0.420	2200	460	1000	1170	0.27
10.0	0.174	0.450	2500	550	1230	1480	0.32
12.2	0.174	0.420	3080	700	1410	1790	0.34
16.7	0.174	0.460	3100	2300	1700	2280	0.38
25.0	0.174	0.420	3360	2090	2120	3060	0.41
4.0	0.171	0.121	1580	62	605	660	0.21
5.85	0.171	0.135	2580	110	1070	1290	0.33
8.35	0.171	0.121	3470	155	1260	1540	0.34
10.0	0.167	0.161	5300	335	1460	1840	0.39
12.2	0.171	0.122	4050	335	1660	2180	0.40
16.7	0.171	0.125	4410	570	1940	2680	0.41
25.0	0.171	0.134	4410	960	2160	3110	0.39
33.3	0.171	0.130	4350	1840	2480	3840	0.42
4.00	0.171	0.039	5400	40	1140	1360	0.43
5.85	0.171	0.040	6250	65	1370	1700	0.44
8.35	0.171	0.040	7450	115	1620	2110	0.46
10.0	0.179	0.037	4950	115	1740	2320	0.45
12.2	0.171	0.038	8600	190	1880	2580	0.47
16.7	0.171	0.035	10100	310	2160	3100	0.48
25.0	0.171	0.037	10800	620	2440	3780	0.48
33.3	0.171	0.039	11100	1040	2670	4300	0.47

Table A8

Influence of the number of rows of scraper blades on the heat transfer coefficient for various viscosities

Number of rows of blades	Mass flow rate (kg. s^{-1})	Viscosity (N. s. m^{-2})	Loss of sensible heat (W)	Frictional heat (W)	Overall heat transfer coefficient (W. m^{-2}. ^{o}C^{-1})	Scraped side heat transfer coefficient (W. m^{-2}. ^{o}C^{-1})	φ
2	0.174	0.45	2500	540	1230	1480	0.32
3	0.174	0.44	3040	685	1410	1820	0.32
4	0.174	0.45	2610	940	1400	1760	0.27
6	0.174	0.40	2530	1260	1360	1680	0.21
2	0.167	0.161	5300	335	1460	1840	0.39
3	0.171	0.126	4000	450	1600	2140	0.35
4	0.171	0.132	4250	420	1870	2540	0.36
6	0.171	0.129	4700	560	2060	2920	0.31
2	0.179	0.036	4950	115	1740	2320	0.45
3	0.171	0.038	8300	160	1830	2480	0.40
4	0.171	0.041	9100	210	2050	2760	0.39
6	0.171	0.039	10200	260	2280	3380	0.39

Table A 9

Influence of the annular space on the heat transfer coefficient for various viscosities

Shaft diameter (m)	Mass flow rate ($kg.s^{-1}$)	Viscosity ($N.s.m^{-2}$)	Loss of sensible heat (W)	Frictional heat (W)	Overall heat transfer coefficient ($W.m^{-2}.^{o}C^{-1}$)	Scraped side heat transfer coefficient ($W.m^{-2}.^{o}C^{-1}$)	φ
0.046	0.174	0.415	2690	520	1230	1480	0.32
0.056	0.174	0.450	2490	535	1230	1480	0.32
0.062	0.174	0.410	1900	615	940	1090	0.32
0.068	0.174	0.430	3130	580	1510	1930	0.42
0.046	0.171	0.123	3710	290	1450	1830	0.37
0.056	0.167	0.161	5300	335	1460	1840	0.39
0.062	0.171	0.145	2930	535	1400	1760	0.35
0.068	0.171	0.127	3840	275	1560	2030	0.40
0.046	0.171	0.039	8500	160	1760	2340	0.47
0.056	0.179	0.037	4950	115	1740	2320	0.45
0.062	0.171	0.037	7300	160	1660	2180	0.44
0.068	0.171	0.039	7600	130	1630	2180	0.44

LIST OF SYMBOLS

A	heat transfer area	(L^2)
a	$\lambda/\rho c_p$ = thermal diffusivity	(L^2t^{-1})
a'	constant in viscosity equation	(T^{-1})
a_w	thermal diffusivity of wall material	(L^2t^{-1})
B	dimensionless thickness of scraper blade edge	(-)
C	concentration of tracer liquid in working fluid	(-)
C_1, C_2, C_3, C_4	constants	various
c_p	specific heat of fluid	$(L^2t^{-2}T^{-1})$
c_w	specific heat of wall material	$(L^2t^{-2}T^{-1})$
D_E	axial dispersion coefficient	(L^2t^{-1})
d_s	shaft diameter	(L)
d_t	diameter of heat transfer tube	(L)
$E(\theta)d\theta$	fraction of total flow with residence times between θ and $\theta + d\theta$	(-)
$F(\theta)$	fraction of total flow with residence times less than θ	(-)
g_z	acceleration of gravity in z-direction	(Lt^{-2})
K_o	modified Bessel function of the second kind and zero order	(-)
K_1	modified Bessel function of the second kind and first order	(-)
K_1, K_2, K_3, K_4	constants in the solution of Eq. (34)	various
L	length of scraped surface	(L)
m	thickness of scraped blade	(L)
m'	mass of scraper blade per unit length	(ML^{-1})
N	shaft speed	(t^{-1})
N_T	$\alpha_s A/\emptyset_m c_p$ = dimensionless group in Fig. 2	(-)
Nu	$\alpha_s d_t/\lambda$ = Nusselt number	(-)
n	number of rows of scraper blades	(-)
n_T	number of perfectly mixed tanks	(-)
P	power consumed by rotating shaft plus blades	(ML^2t^{-3})

Pe	$v(d_t-d_s)/a$ = Péclet number	(-)
Pe_D	vL/D_E = Péclet number for axial dispersion	(-)
Po	$P/\rho N^3 d_t^4 L$ = power number	(-)
Pr	$\eta c_p/\lambda$ = Prandtl number	(-)
p	pressure	$(ML^{-1}\ t^{-2})$
Q'	heat flux from heat source	(Mt^{-3})
q	heat flux from tube wall	(Mt^{-3})
R	parameter in power consumption model	(-)
Re_R	$d_t^2 N\rho/\eta$ = Reynolds number for rotation	(-)
Re_{cr}	critical rotational Reynolds number	(-)
S	total displacement of liquid particle	(L)
s	width of scraper blade edge	(L)
T	temperature	(T)
T_o	temperature of heat transfer tube wall	(T)
T_1, T_2	inlet and outlet temperature of fluid	(T)
$\langle T \rangle$	average temperature of heat source	(T)
ΔT	increase in temperature of liquid between scraper blade edge and wall	(T)
T_b	temperature of the liquid contacting the wall after blade passage	(T)
t	time	(t)
U	overall heat transfer coefficient	$(Mt^{-3}\ T^{-1})$
v	mean axial velocity of fluid	(Lt^{-1})
v_o	tangential velocity of wall of model SSHE	(Lt^{-1})
v_θ	tangential velocity component	(Lt^{-1})
X, Z	dimensionless coordinates	(-)
y	parameter in power consumption model	(-)
α^*	heat transfer coefficient between heat source and semi-infinite body	$(Mt^{-3}T^{-1})$
α_c	heat transfer coefficient from heat transfer medium to tube wall	$(Mt^{-3}T^{-1})$
α_{eff}	effective heat transfer coefficient	$(Mt^{-3}T^{-1})$
α_m	heat transfer coefficient between scraper blade and fluid	$(Mt^{-3}T^{-1})$
α_s	heat transfer coefficient at scraped side	$(Mt^{-3}T^{-1})$

α_o	heat transfer coefficient from scraped wall to heat transfer medium	$(Mt^{-3}T^{-1})$
β,γ	parameters in power consumption model	(-)
γ	relative skewness of E-curve	(-)
δ	clearance between blade edge and tube wall	(L)
δ_D	thickness of stagnant layer in radial dispersion model	(L)
δ_T	depth of penetration of heat	(L)
ϵ	parameter in Eq. (69)	$(L^{-3/2})$
ζ	transformed coordinate	$(L^{3/2})$
η	fluid viscosity	$(ML^{-1}t^{-1})$
η^*	viscosity of liquid between blade edge and wall	$(ML^{-1}t^{-1})$
η_L	local viscosity	$(ML^{-1}t^{-1})$
θ	normalized residence time	(-)
λ	thermal conductivity of fluid	$(MLt^{-3}T^{-1})$
λ_s	thermal conductivity of blade material	$(MLt^{-3}T^{-1})$
λ_w	thermal conductivity of wall material	$(MLt^{-3}T^{-1})$
ν	kinematic viscosity	(L^2t^{-1})
ξ	transformed coordinate	$(L^{3/2})$
ρ	fluid density	(ML^{-3})
ρ_w	density of wall material	(ML^{-3})
σ^2	variance of E-curve	(-)
τ	average residence time	(t)
$\emptyset_m$	mass flow rate of liquid	(Mt^{-1})
φ	correction term in Eq. (9)	(-)

SUMMARY

The heat transfer coefficients in heat exchangers without moving parts are very low for viscous liquids. However, if the surface of the heat exchanger is scraped continuously, high temperature gradients and hence high heat transfer coefficients are obtained.

One type of scraped-surface heat exchangers (hereafter referred to as SSHEs) consists of two concentric cylinders, the outer one being cooled or heated by the heat transfer medium. The inner rotating cylinder is equipped with scraper blades that scrape the outer cylinder. The working fluid flows through the annulus formed by the two cylinders.

The investigation described in this thesis was initiated to study the mechanisms governing power consumption, heat transfer and flow in a SSHE. Furthermore the aim was to determine the influence of design and operating conditions on heat transfer and power consumption.

By suspending polyethene beads in glycerol/water solutions, and operating a glass-walled SSHE with this suspension, it was established that the flow was in one of the following two regimes, depending on the operating conditions:

- Couette flow. This is simple shear flow in which the radial velocity component is zero outside the area close to the blades.
- Taylor vortices. Above a certain critical rotational Reynolds number large secondary vortices are formed in pairs with opposite rotation. The diameter of a vortex is approximately equal to the width of the annular space. Within the accuracy of the experiments, the critical Reynolds number is equal to that for flow in the annulus between smooth rotating cylinders.

The flow in the Couette-regime was further studied in a perspex model of the SSHE. In this model a dye could be injected at different positions in the SSHE. In this way streamline patterns and velocity profiles were determined. The streamlines are concentric circles outside the blade area

(for cutaway blades). The streamlines contract and expand near the blades. The resulting velocity profile is similar to that between two parallel plates, one of which is moving, and with a pressure gradient in the direction of the flow.

Residence time distributions were measured by injecting a pulse of dye near the inlet of a SSHE and sampling continuously at the outlet. The residence time of the liquid flowing through the SSHE is not uniform. This is partly caused by differences in velocity along, and in length of, streamlines and partly by dispersion mechanisms due to vortices and a pumping effect. The axial dispersion is so great that for some of the heat transfer measurements the effective driving force for heat transfer is smaller than calculated for the plug flow model.

Power consumption was measured under various operating conditions of a SSHE, by recording the torque and the rotational speed of the shaft. For most stirrers the power number, Po, is a unique function of the rotational Reynolds number, Re_R. This is not valid for SSHEs. For the same value of Re_R, Po increases with decreasing viscosity. This is caused by two phenomena:

- Due to viscous dissipation the temperature of the liquid between the edge of the blade and the wall increases and therefore the viscosity decreases.
- The clearance between the edge of the scraper blade and the tube wall is dependent on the operating conditions and the physical properties of the fluid.

A model with these effects included has been derived for the power consumption. The parameters in this model have been determined from the experiments. The values of the parameters thus determined were in agreement with the results of the flow studies. An empirical equation for power consumption, which is more readily evaluated, has also been derived.

The mechanism for heat transfer in a SSHE consists of three steps:

- Penetration of heat by conduction in a thin layer close to the heat transfer surface in the time between two scrapings.
- Partial temperature equalization in the boundary layer that builds up on the scraper blade.
- Convective radial transport from the cooled layer to the bulk of the liquid.

Taylor vortices contribute to this radial transport.

Heat transfer measurements were conducted under various conditions.

The heat transfer coefficient can be described by means of an equation resulting from penetration theory, modified by an empirically determined correction factor φ. In φ are included:

- The incompleteness of the temperature equalization in the boundary layer.
- The effect of radial dispersion.
- The decrease in driving force for heat transfer due to axial dispersion.

When the influence of the axial dispersion on heat transfer is absent (high mass flow rates), φ has a value between 0.4 and 0.5, if Taylor vortices are present. Below the critical Reynolds number, φ diminishes due to insufficient radial mixing.

At low mass flow rates the influence of the axial dispersion on the driving force for heat transfer is important. The apparent decrease in heat transfer coefficient due to this effect can be calculated. To do so, the plug flow with dispersion model is applied in which the axial dispersion coefficient is calculated from the standard deviation of the residence time distribution curve.

The results of this investigation can be applied in the design of SSHEs.

SAMENVATTING

Voor viskeuze vloeistoffen zijn de warmteoverdrachtscoëfficiënten in warmtewisselaars zonder bewegende delen zeer laag. Door echter het oppervlak van de warmtewisselaar voortdurend te schrapen kan men grote temperatuurgradiënten en daardoor hoge warmteoverdrachtscoëfficiënten verkrijgen.

Een van de typen van geschraapte warmtewisselaars (in dit proefscrhfit aangeduid met SSHE) bestaat uit twee concentrische cylinders waarvan de buitenste gekoeld of verwarmd wordt door het warmteoverdrachtsmedium. De binnenste cylinder roteert en is uitgerust met schraapmessen die de buitenste cylinder afschrapen. De werkvloeistof stroomt door de ringvormige ruimte tussen de twee cylinders.

Het doel van het in dit proefschrift beschreven onderzoek was het bestuderen van de mechanismen die aan energieverbruik, warmteoverdracht, en stroming in een SSHE ten grondslag liggen en het bepalen van de invloed van de uitvoering van de SSHE en de procesomstandigheden op warmteoverdracht en energieverbruik.

Door polyetheen deeltjes in glycerol/water-mengsels te suspenderen en deze suspensie door een SSHE met een glazen buitenwand te voeren bleek dat de stroming, afhankelijk van de omstandigheden, volgens één van de volgende patronen verliep:

- Couettestroming. Dit is een eenvoudige stroming door afschuiving waarbij de radiale snelheidscomponent buiten het gebied vlakbij de messen nul is.
- Taylor wervels. Boven een bepaald kritisch Reynoldsgetal voor rotatie worden grote secundaire wervels gevormd in paren met tegengestelde draaiing. De diameter van een wervel is ongeveer gelijk aan de spleetbreedte tussen de cylinders. Binnen de nauwkeurigheid van de experimenten is het kritische Reynoldsgetal gelijk aan dat voor stroming in de ruimte tussen gladde roterende cylinders.

De Couettestroming werd verder bestudeerd in een perspex model van de SSHE. Daarin kon op verschillende plaatsen een kleurstof worden ingespoten, waardoor de patronen van de stroomlijnen en de snelheidsprofielen konden worden bepaald. Voor open messen zijn de stroomlijnen concentrische cirkels die bij de messen dichter bij elkaar komen te lopen. Het snelheidsprofiel lijkt op dat tussen twee evenwijdige platen waarvan de ene beweegt en waarbij een drukgradiënt in de richting van de stroming bestaat.

De verblijftijdsspreiding werd gemeten door een hoeveelheid kleurstof in de leiding vlak vóór de SSHE te injecteren en bij de aftapopening continu monsters te trekken. De verblijftijd van de vloeistof die door de SSHE stroomt is niet uniform. Dit wordt gedeeltelijk veroorzaakt door snelheidsverschillen langs de stroomlijnen en gedeeltelijk door dispersie door wervels en een pompeffect. De axiale dispersie is zo groot dat bij sommige warmteoverdrachtsmetingen de effectieve drijvende kracht voor warmteoverdracht kleiner is dan voor propstroming kan worden berekend.

Onder verschillende omstandigheden werd het energieverbruik in een SSHE gemeten door het moment en de omwentelingssnelheid van de as te registreren. Voor de meeste roerders is het vermogenskengetal Po een éénduidige functie van het Reynoldsgetal voor rotatie, Re_R. Dit geldt niet voor SSHE's. Bij gelijkblijvende Re_R neemt Po toe als de viscositeit daalt. Twee verschijnselen zijn hiervan de oorzaak:

- door viskeuze dissipatie neemt de temperatuur tussen de rand van het mes en de wand toe, waardoor de viscositeit daalt;
- de afstand tussen de rand van het mes en de wand hangt af van de waarden van de ingestelde variabelen van het apparaat, en van de fysische eigenschappen van de werkvloeistof.

Voor het energieverbruik is een model afgeleid waarin met deze effecten rekening is gehouden. De parameters uit dit model zijn experimenteel bepaald. De waarden ervan waren in overeenstemming met de resultaten van het stromingsonderzoek. Ook is een empirische vergelijking voor het energieverbruik afgeleid die praktisch gemakkelijker bruikbaar is.

Het mechanisme voor warmteoverdracht in een SSHE bestaat uit drie stappen:

- penetratie van warmte door geleiding in een dunne laag vlakbij de wand in de tijd tussen twee schrapingen;
- gedeeltelijke temperatuurvereffening in de grenslaag die op het mes wordt opgebouwd;

- radiaal transport door convectie van de gekoelde laag naar de vloeistofmassa. Taylor wervels leveren een bijdrage aan dit radiaal transport.

Onder verschillende omstandigheden werden warmteoverdrachtsmetingen uitgevoerd. De warmteoverdrachtscoëfficiënt kan worden beschreven door een vergelijking die afkomstig is uit de penetratietheorie en gecorrigeerd wordt met een empirisch bepaalde correctiefactor φ. Daarin zijn opgenomen:

- het effect, dat de temperatuurvereffening in de grenslaag niet volledig is;
- het effect van de radiale dispersie;
- de verlaging in de drijvende kracht voor warmteoverdracht, veroorzaakt door axiale dispersie.

Als er geen invloed van de axiale dispersie op de warmteoverdracht is (hoge debieten) en in aanwezigheid van Taylor wervels heeft φ een waarde van 0.4-0.5. Beneden het kritische Reynoldsgetal neemt φ af door onvoldoende radiale menging.

Bij lage debieten is de invloed van de axiale dispersie op de drijvende kracht voor warmteoverdracht belangrijk. De door dit effect veroorzaakte daling van de warmteoverdrachtscoëfficiënt kan worden berekend met behulp van het model voor propstroming met axiale dispersie. De coëfficiënt voor axiale dispersie wordt berekend uit de standaarddeviatie van de curve voor de verblijftijdsspreiding.

De bij het onderzoek verkregen resultaten kunnen bij het ontwerpen van geschraapte warmtewisselaars worden toegepast.

REFERENCES

1. J.P.Bolanowski and D.D.Lineberry, Ind.Eng.Chem. 44, 657 (1952).
2. C.W.Vogt (to Vogt Instant Freezers Inc.), USA Pat. 1,783,685, appl. 17 III 1928, publ. 2 XII 1930.
3. A.Johnson & Co (London) Ltd., Br.Pat. 1,136,423, appl. 2 VI 1966, publ. 11 XII 1968.
4. Sen-ichi Sato and Motoo Morinaga (to Mitsubishi Kakoki Co. Ltd.), Jap. Pat. 3,521-1962, appl. 19 XI 1959, publ. 6 VI 1962.
5. F.E.Huggins, Ind.Eng.Chem. 23, 749 (1931).
6. H.G.Laughlin, Trans.Am.Inst.Chem.Engrs. 36, 345 (1940).
7. H.G.Houlton, Ind.Eng.Chem. 36, 522 (1944).
8. F.W.Dittus and L.M.K.Boelter, Univ.Calif.(Berkeley) Publs.Eng. 2, 443 (1930).
9. A.H.P.Skelland, Chem.Eng.Sci. 7, 166 (1958).
10. M.J.McNelly, J.Imp.Coll.Chem.Eng.Soc. 7, 18 (1953).
11. A.H.P.Skelland, Brit.Chem.Eng. 3, 325 (1958).
12. G.A.Latinen, Chem.Eng.Sci. 9, 263 (1958-59).
13. H.S.Carslaw and J.C.Jaeger, Conduction of heat in solids, Clarendon Press, Oxford, 1959^2.
14. J.Kool. Trans.Inst.Chem.Engrs. (London) 36, T253 (1958).
15. P.Harriot, Chem.Engr.Progr.Symp.Ser. 55 (29), 137 (1959).
16. J.L.Blaisdell and J.W.Zahradnik, Food Technol. 13, 659 (1959).
17. A.H.P.Skelland, Brit.Chem.Eng. 5, 708 (1960).
18. A.H.P.Skelland, D.R.Oliver and S.Tooke, Brit.Chem.Eng. 7, 346 (1962).
19. A.P.Hosking, Trans.Inst.Chem.Engrs. (London) 161, A97 (1962).
20. A.H.P.Skelland and L.S.Leung, Brit.Chem.Eng. 7, 264 (1962).
21. G.Dinglinger, Kältetechnik 16, 170 (1964).
22. L.N.Braginskii, V.I.Begachev and I.S. Pablushenko, Zh. Prikl.Khim. 37, 1984 (1964).
23. L.L.van Dierendonck, Paper read at the Symposium"Hanteren van viskeuze vloeistoffen II", Utrecht, 1965.

24. A.Koelatsjinski, Molochn.Prom. 26 (2), 11 (1965).

25. A.Vinogradov, Molochn.Prom. 26 (2), 15 (1965).

26. W.R.Penney and K.J. Bell, Ind.Eng.Chem. 59 (4), 40 (1967).

27. W.R.Penney and K.J.Bell, Ind.Eng.Chem. 59 (4), 47 (1967).

28. T.R.Bott, S.Azoory and K.E.Porter, Trans.Inst.Chem.Engrs. (London) 46, T37 (1968).

29. J.K.Ghosal, B.N.Srimani and D.N.Ghosh, Indian Chem.Eng. 9, T53 (1964).

30. N.van Lookeren Campagne, Longitudinale dispersie in de stroming door een ringspleet met draaiende binnencilinder, Thesis Groningen, 1966.

31. E.T.White, J.Imp.Coll.Chem.Eng.Soc. 14, 72 (1962).

32. E.A.Koldenhof and W.J.Beek, Ingenieur 77, Ch 25 (1965).

33. O.Levenspiel, Chemical reaction engineering, Wiley, New York, 1962.

34. J.J.van Deemter, Chem.Eng.Sci. 13, 190 (1961).

35. A.E.Norton, Lubrication, McGraw Hill Publ. Co., New York, 1942.

36. H.Schlichting, Grenzschichttheorie, Verlag G.Braun, Karlsruhe, 1958^3

37. A.M.Trommelen and S.Boerema, Trans.Inst.Chem.Engrs. (London) 44, T329 (1966).

38. R.B.Bird, W.E.Stewart and E.N.Lightfoot, Transport Phenomena, Wiley & Co., New York, 1960.

39. H.A. Snyder, Phys.Fluids 11, 1606 (1968).

40. H.S.Hele-Shaw, Trans.Inst.Naval Architects 40, 21 (1898).

41. S.Flügge, Handbuch der Physik, Band VIII/2, Strömungsmechanik II, Springer, Berlin, 1963.

42. H.B.Dwight, Tables of integrals and other mathematical data, The Macmillan Co., New York, 1961^4;